Report No. UCB/SEMM-2014/01	Structural Engineering Mechanics and Materials
	Lateral Buckling in Reinforced Concrete Walls By Pablo F. Parra, and Jack P. Moehle
March 2014	Department of Civil and Environmental Engineering University of California, Berkeley

ABSTRACT

Structural (shear) walls are used worldwide to resist gravity and earthquake loads. In many countries, structural walls commonly are constructed with a rectangular cross section, or a cross section made up of interconnected rectangles, without an enlarged boundary element. In some countries, design practice has resulted in walls that are more slender than those used in the past. For example, in Chile and elsewhere it is not unusual to find rectangular wall edges having thickness of 6 to 8 in. (150 to 200 mm), resulting in floor-to-floor slenderness ratios reaching $hu/b = 16$ or greater. Such walls can be susceptible to overall wall buckling in which a portion of the walls buckles out of the plane of the wall. Examples of this behavior were observed following the 2010 Chile and the 2011 Christchurch, New Zealand earthquakes.

Tendency to buckle is believed to depend primarily on the wall clear height to thickness ratio hu/b and loading history. Two failure modes are hypothesized. One hypothesis is that tensile yielding for loading in one direction softens the boundary for subsequent loading in the opposite direction, leading to lateral instability of an otherwise intact wall. A second hypothesis is that the wall crushes first, leaving an even smaller and irregular cross section. This crushed section may become immediately unstable or, alternatively, subsequent tension and compression cycles may lead to instability of the reduced cross section according to the first hypothesis, leading to a secondary buckling failure. Either type of buckling can lead to critical loss of axial force capacity in the flexural compression zone of the wall.

A theory is presented for buckling of reinforced concrete sections subjected to inelastic tension and compression strain cycles. The theory is applied to tests of reinforced concrete prisms and walls tested in the laboratory. The theory is also applied to two Chilean buildings (Alto Huerto and Emerald). Both buildings had some buckled walls after the 2010 Chile earthquake. Based on the study of these buildings, it is concluded that buckling most likely was a secondary failure that occurred after initial crushing of the wall boundaries.

ACKNOWLEDGMENTS

This research has been supported by the National Institute of Standards and Technology through the ATC 94 project. Their support is gratefully acknowledged. Opinions, findings, conclusions and recommendations are those of the writers and do not necessarily represent those of the sponsor.

CONTENTS

LIST OF FIGURES

LIST OF TABLES

1 Introduction

1.1 BACKGROUND

Design practices prior to the 1990s favored rectangular walls with enlarged boundary elements, contributing to stability of the flexural compression zone. More recently, prevailing practices in many countries favor rectangular sections without enlarged boundaries. The more slender flexural compression zones can be susceptible to inelastic lateral buckling as shown in Figure 1.1.

Figure 1.1 Buckled wall in first story of Alto Huerto building (DICTUC report #906575/10-056-EE-01-R0, 2010).

When parts of a wall section are subjected to compression strains, the possibility of lateral instability arises. Although global wall buckling occurs when the wall boundary is in compression, buckling can be strongly influenced by the magnitude of the tensile strain experienced by the wall for prior loading in the opposite direction (Paulay and Priestley, 1993; Chai and Elayer, 1999). This is because residual tensile strains in the previously yielded longitudinal reinforcement leave the wall boundary with open cracks, resulting in reduced lateral stiffness.

Consider a multi-story wall as shown in Figure 1.2. The foundation, floor diaphragms, and roof diaphragm provide lateral support at every story level. Thus, the unsupported height of the wall boundary can be taken equal to the story clear height, h_u.

An effective length kh_u can be defined based on the rotational restraints at the different floor levels. In the present analysis, which is concerned with very slender walls, it may be

reasonable to consider the wall to be fixed at top and bottom of the clear height. Accordingly, k is taken equal to 0.5.

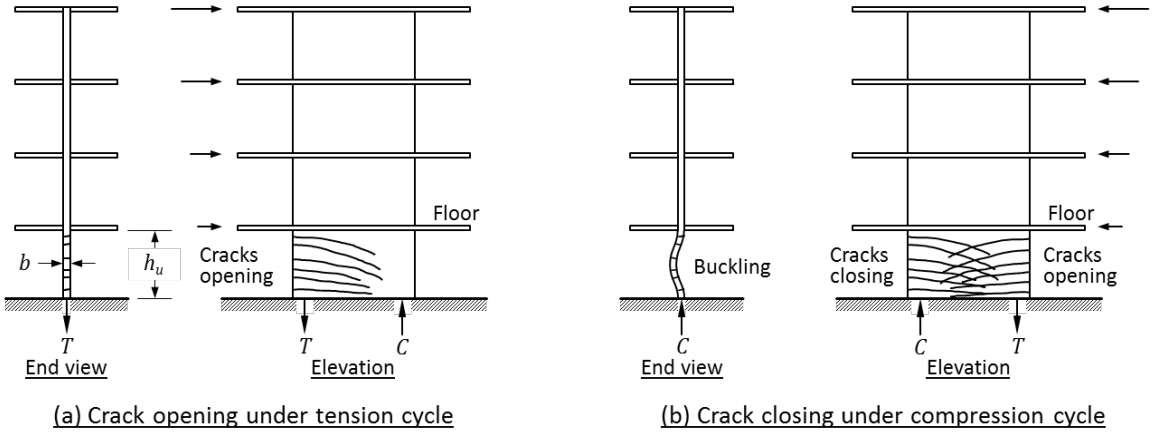

Figure 1.2 Lateral instability of wall boundary previously yielded in tension (After Chai and Elayer, 1999).

A typical wall boundary will be subjected to alternating tension and compression as a building responds to an earthquake (Figure 1.2). If the boundary yields in tension, a cracked section is produced, with crack width dependent on the amplitude of the reinforcement tensile strain ϵ_{sm} during the tension excursion. In a previously yielded wall, crack closure under deformation reversal may require yielding of the longitudinal reinforcement in compression. In a wall with two curtains of reinforcement, any slight asymmetry in the reinforcement is likely to result in one curtain yielding before the other, leading to out-of-plane curvature and a tendency to buckle out of plane. In a wall with one curtain of reinforcement, out-of-plane curvature occurs even more readily. Whether the wall remains stable depends on the amplitude of the prior tensile strain ϵ_{sm} and the slenderness ratio h_u/b of the wall. As a design approximation, the critical slenderness ratio can be related to the maximum prior tensile strain ϵ_{sm}, as will be shown later.

In this report different procedures are used to estimate ϵ_{sm} in laboratory tested walls (Oesterle et al., 1976; Thomsen and Wallace, 2004) and Chilean buildings walls. The selected buildings were Alto Huerto (San Pedro de la Paz) and Emerald (Santiago). Both of them experienced wall buckling after the 2010 Chile Earthquake. The estimated tensile strain values are compared with the limit given by the buckling theory developed in Section 2.2. This enables an assessment of whether the walls are likely to have buckled prior to concrete crushing.

1.2 RESEARCH PROGRAM OBJECTIVES

This report addresses the key aspects involved in overall wall buckling during cyclic loading. The research program had the following specific objectives:

- To develop a buckling theory for walls subjected to cyclic loading. This theory allows to determine the maximum tensile strain experienced by the wall prior compressive loading at which lateral instability is triggered
- For tests on five walls subjected to reversed cyclic loading, to compare analytical and experimental strain profiles and perform buckling analysis in order to propose the mechanics that best explains the observed lateral instability

- For five walls in two Chilean buildings (Alto Huerto and Emerald), to estimate analytically the drift demands and the strain profiles in the plastic hinge zone during the 2010 Chile earthquake. Then, to compare the analytical and observed response and propose the mechanism that best explains the observed lateral instability
- Finally, to provide recommendations to improve design practice for slender structural walls

1.3 ORGANIZATION OF REPORT AND SCOPE

Chapter 2 presents the derivation of the buckling model for walls subjected to alternating tension and compression cycles, and compares the model results with test results. The first set of tests is on prismatic sections reinforced as rectangular boundary elements. The second set of tests is on reinforced concrete walls subjected to lateral displacement cycles. For the wall tests, various methods for estimating the relation between base level strain and top level displacement are investigated.

Chapters 3 and 4 present analysis results for two buildings whose walls showed apparent buckling damage following the 2010 Chile earthquake. These are the Alto Huerto building (San Pedro de la Paz) and the Emerald building (Santiago). For the Alto Huerto building (Chapter 3), analyses include linear analyses using ETABS, nonlinear analyses using PERFORM 3D, and a simplified nonlinear analysis. For the Emerald building (Chapter 4), only the linear analysis and the simplified nonlinear analysis are done. The group of building analyses provides data from which to assess the likelihood of failure being triggered by concrete crushing or by wall lateral instability.

Chapter 5 presents a summary of the findings of the study.

2 Buckling of Prismatic Sections under Tension-Compression Reversals

2.1 INTRODUCTION

This chapter presents the derivation of the wall buckling model and compares results using that model with results from laboratory tests on reinforced concrete prisms subjected to tension-compression cycles and on walls subjected to lateral displacement cycles. The results provide a partial basis for the analyses of buildings in subsequent chapters.

2.2 BUCKLING THEORY

In the following theoretical development, some of the modeling concepts of Paulay and Priestley (1993) are followed. Consider the wall shown in Figure 2.1. Wall lateral buckling is constrained by the story clear height (Figure 2.1a). We assume the wall has been flexed previously such that the boundary yields in tension (Figure 2.1b), with a unit length (measured in the horizontal direction) of the boundary element developing tension force T, maximum tensile stress f_{sm}, and tensile strain ϵ_{sm}. Upon deformation reversal, just before the boundary element yields in compression, the longitudinal reinforcement will have unloaded by strain $\epsilon_s = f_{sm}/E_s$ and reloaded in compression to $-\epsilon_y$ (ignoring the Bauschinger effect), such that the residual tensile strain is approximately $\epsilon_{res} = \epsilon_{sm-} f_{sm}/E_s - \epsilon_y$. To simplify the model, the residual tensile strain is approximated as $\epsilon_{res} \approx \epsilon_{sm} - 0.005$. Invariably, one curtain of reinforcement will yield before the other, producing curvature as shown in Figure 2.1d, and out-of-plane displacement as illustrated in Figure 2.1a and Figure 2.1c. Whether the boundary remains stable depends on magnitude of the lateral displacement δ relative to the wall thickness b, which relates to the maximum previous tensile strain ϵ_{sm} and the resulting curvature as illustrated in Figure 2.1c.

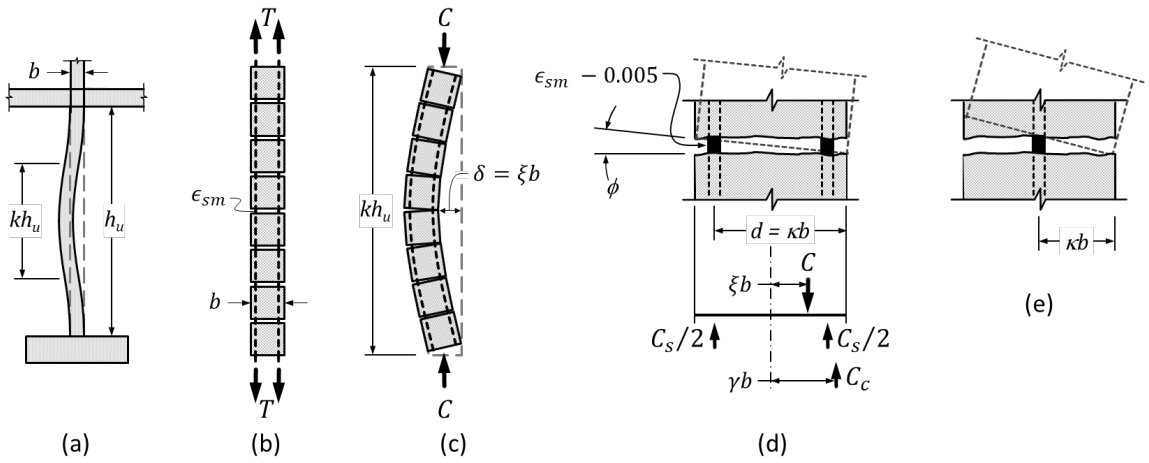

Figure 2.1 Lateral instability of wall boundary previously yielded in tension.

To estimate conditions for stability, we first approximate the effective length (height). For a multi-story wall with length l_w not less than the first-story clear height h_u, it is reasonable to assume that the flexural plastic hinge extends over the height of the first story. Assuming fixity at top and bottom, with a simple harmonic buckled shape, the effective length in Figure 2.1a is $kh_u = 0.5h_u$. Examining the effective length more closely (Figure 2.1c), we can express the maximum deflection as a fraction of wall thickness (that is, $\delta = \xi b$). The relation between maximum deflection and the maximum curvature $\emptyset_{max}$ is:

$$\delta = \xi b = \emptyset_{max} \left(\frac{kh_u}{\pi}\right)^2 \tag{2.1}$$

As a first approximation, the maximum curvature from Figure 2.1d can be written as:

$$\emptyset_{max} = \frac{\in_{sm} - 0.005}{d} \tag{2.2}$$

Equilibrium of forces and moments in the free-body diagram of Figure 2.1d results in the following two expressions:

$$\sum F = 0 \rightarrow C = C_s + C_c \tag{2.3}$$

$$\sum M = 0 \rightarrow C\xi b = C_c \gamma b \tag{2.4}$$

In Equation (2.4), moments are taken about the centerline, such that moments of longitudinal reinforcement compressive force resultants (assumed equal) cancel. Assuming longitudinal reinforcement is stressed to f_y and assuming the concrete compressive force C_c is represented by the usual rectangular stress block with depth $\beta_1 c$ and average stress $0.85f'_c$, we can write

$$C_s = \rho b f_y \tag{2.5}$$

$$C_c = 0.85f'_c(1 - 2\gamma)b \tag{2.6}$$

Substituting Equations (2.3), (2.5), and (2.6) in Equation (2.4) and manipulating the results we obtain:

$$(1-2\gamma)\left(\frac{\gamma}{\xi}-1\right)=\frac{\rho f_y}{0.85f'_c}=\frac{m}{0.85} \tag{2.7}$$

in which $m=\rho f_y/f'_c$ is the mechanical reinforcement ratio. This expression has real roots only if the following is satisfied:

$$\xi \le 0.5\left(1+\frac{2m}{0.85}-\sqrt{\left(\frac{2m}{0.85}\right)^2+\frac{4m}{0.85}}\right) \tag{2.8}$$

Substituting ξ from Equation (2.8) into Equation (2.1), solving for b/h_u, and defining width b as the critical width b_{cr} results in:

$$\frac{b_{cr}}{kh_u}=\frac{1}{\pi}\sqrt{\frac{\epsilon_{sm}-0.005}{\kappa\xi}} \tag{2.9}$$

The main variables appearing in Equation (2.9) are slenderness ratio kh_u/b, maximum tensile strain ϵ_{sm} in longitudinal reinforcement, effective depth parameter κ for longitudinal reinforcement, and ξ. Parameter κ can be found from $d=\kappa b$, where it is noted that $\kappa \approx 0.8$ for thin walls with two curtains of reinforcement and 0.5 for walls with single layer of reinforcement. From this, it is clear that walls with two curtains of longitudinal reinforcement are inherently more stable than walls with a single curtain. Parameter ξ relates to the mechanical reinforcement ratio Equation (2.8), which is an inconvenient parameter for preliminary design. For practical construction, $0.4 \le \sqrt{\xi} \le 0.6$.

Adopting values $\kappa=0.8$ and $\sqrt{\xi}=0.5$, Equation (2.9) for walls with two curtains of reinforcement becomes:

$$\frac{b_{cr}}{kh_u}=0.7\sqrt{\epsilon_{sm}-0.005} \tag{2.10}$$

If the cover is lost before buckling the wall (this occurs usually within a compressive strain range of 0.003-0.005), it is more reasonable to use $\kappa=1$ and b_{cr} equal to the confined core width.

For typical slender wall geometries, the boundary can be approximated as fixed-fixed, in which case $k=0.5$. Thus, Equation (2.10) becomes:

$$\frac{b_{cr}}{h_u}=0.35\sqrt{\epsilon_{sm}-0.005} \tag{2.11}$$

Considering low-cycle fatigue, the maximum tensile strain normally accepted for longitudinal reinforcement is approximately $\epsilon_{sm}=0.05$. For $\epsilon_{sm}=0.05$, Equation (2.11) results in $h_u/b_{cr}=13$. Equation (2.11) is plotted in Figure 2.2.

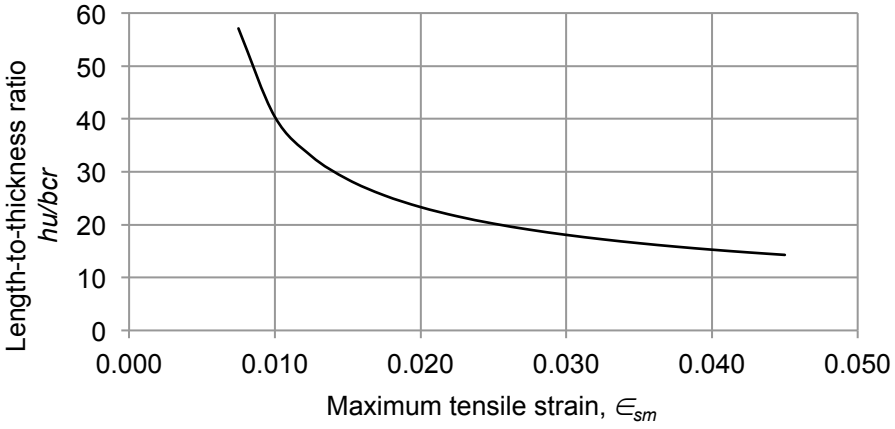

Figure 2.2 Length-to-thickness ratio v/s maximum tensile strain.

The preceding derivation is based on an idealized wall boundary subjected to uniform compressive strain. Actual wall boundaries have strain gradient along the wall length, which would tend to brace the edge of the wall. This suggests that the preceding results should be conservative for actual wall boundaries.

ACI 318 (2011) does not address slenderness of wall boundary elements, although the Uniform Building Code (1997) previously recommended $h_u/b \leq 16$. Moehle et al. (2011), writing about U.S. practice, recommended $h_u/b \leq 10$ within the intended hinge region and $h_u/b \leq 16$ elsewhere. Eurocode 8 (2004) specifies minimum wall thickness of 8 inches (200mm) for confined parts of walls. Moreover, if the length of the confined part does not exceed the larger of $2b$ and $0.2l_w$, b should be at least $h_u/15$. Otherwise, b should be at least $h_u/10$. According to NZ 3101 (2006), the thickness of the wall boundary over the height of the plastic hinge but not less than the full height of the first story shall be at least:

$$b_m = \frac{\alpha_r k_m \beta (h_u/l_w + 2) l_w}{1700\sqrt{\xi_r}} \tag{2.12}$$

In which $\alpha_r = 1$ for walls with two curtains of longitudinal reinforcement and 1.25 for walls with one curtain, $\beta = 7$ for ductile plastic regions, $k_m = 1$ except for long walls it can be defined as:

$$k_m = \frac{l_u}{(0.25 + 0.055\, h_u/l_w) l_w} \leq 1.0 \tag{2.13}$$

$$\xi_r = 0.3 - \frac{\rho_l f_y}{2.5\, f_c'} \geq 0.1 \tag{2.14}$$

The term ρ_l refers to the local longitudinal reinforcement ratio in the wall boundary. These equations result in wall slenderness ratio h_u/b ranging from around 8 for slender, heavily reinforced walls to around 30 for more squat, lightly reinforced walls.

2.3 WALLS MODELING

2.3.1 Curvature Integration Approach

A first simplified approach to obtain the relation between the top displacement and the strain profile at the wall base is to integrate the curvature diagram.

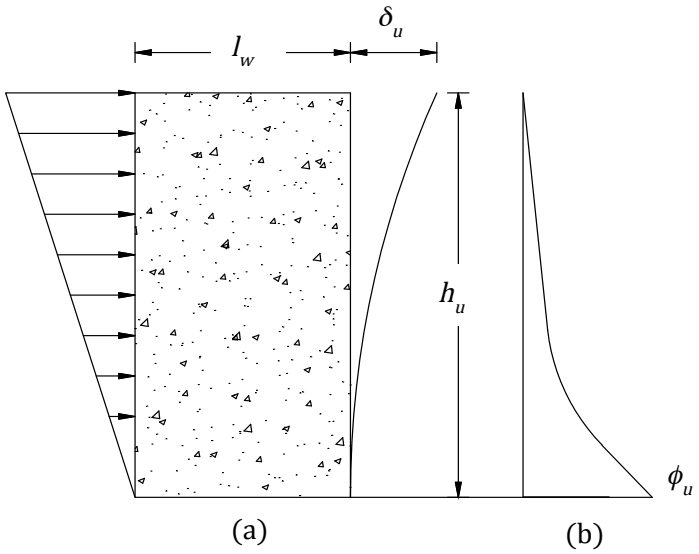

Figure 2.3 Wall flexural deformations: (a) elevation, loading and drift; (b) curvatures.

The lateral displacement at the top of the wall can be obtained from integration of the curvature diagram according to Equation (2.15). Note that this expression includes only wall flexure, and ignores displacement due to shear deformations and slip of reinforcement from the base anchorage.

$$\delta_u = \int_0^{h_u} \emptyset(x)(h_u - x)dx \tag{2.15}$$

Equation (2.16) shows the top displacement when numerical integration is used.

$$\delta_u = \sum_{i=1}^{N} \emptyset(x_i)(h_w - x_i)w_i \tag{2.16}$$

2.3.2 Plastic Hinge Approach

A second simplified approach to obtain the relation between the top displacement and the strain profile at the wall base is to use the plastic hinge approach, according to Figure 2.4.

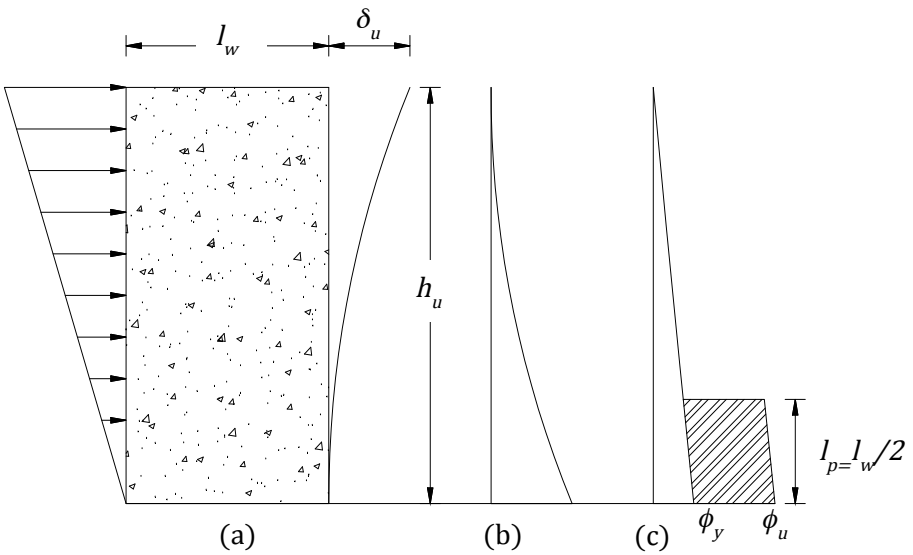

Figure 2.4 Wall flexural deformations: (a) elevation, loading and drift; (b) moments; (c) curvatures.

Equation (2.17) shows the top displacement for this approach.

$$\delta_u = \frac{1}{3}\emptyset_y h_u^2 + (\emptyset_u - \emptyset_y) l_p \left(h_u - \frac{l_p}{2}\right) \tag{2.17}$$

Rearranging terms of Equation (2.17).

$$\emptyset_u = \frac{1}{l_p \left(h_u - \frac{l_p}{2}\right)} \left(\delta_u - \frac{1}{3}\emptyset_y h_u^2\right) + \emptyset_y \tag{2.18}$$

If $\delta_u = DR\, h_u$, where DR is the average drift ratio, then Equation (2.18) can be expressed as shown.

$$\emptyset_u = \frac{h_u}{l_p \left(h_u - \frac{l_p}{2}\right)} \left(DR - \frac{1}{3}\emptyset_y\, h_u\right) + \emptyset_y \tag{2.19}$$

A simpler equation considers the top displacement to be due solely to rotation in the assumed plastic hinge zone, according to Figure 2.5 and Equation (2.20). This approach provides a suitable approximation for cases in which most of the curvature is at the base. Suitable examples include prismatic walls in which large inelastic curvatures occur at the base and nonprismatic walls with reduced sections at the plastic hinge region. According to the approach, the curvature distribution of Figure 2.4 is replaced by a simplified distribution shown in Figure 2.5, where all the elastic curvatures are ignored except those within the plastic hinge. To compensate the low estimate of the wall displacement capacity for a given maximum curvature, the plastic hinge is located centered at the wall base.

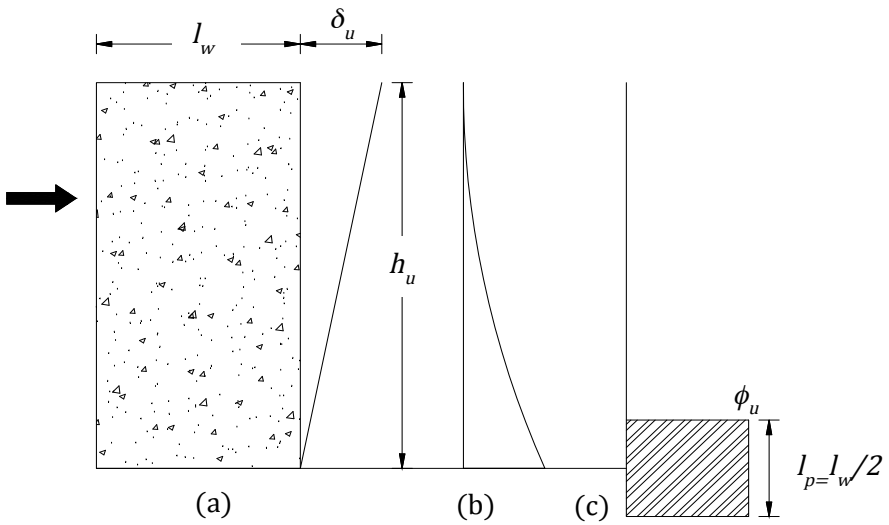

Figure 2.5 Wall flexural deformations: (a) elevation, loading and drift, (b) moments, (c) curvatures.

$$\emptyset_u = \frac{DR}{l_p} \tag{2.20}$$

2.3.3 Strain Profile in Plastic Hinge

The preceding sections define simplified approaches to estimate the relation between displacement at the wall top and the curvature at the base. Once the curvature at the base is calculated, the strain profile can be estimated using moment-curvature analysis considering strains vary linearly across the section depth, with appropriate stress-strain relations for materials. In this report, we use the software XTRACT with stress-strain relations based on monotonic stress-strain behavior and real material properties.

2.4 TENSION/COMPRESSION PRISM TESTS

2.4.1 Introduction

Several tests have been done (Chai and Elayer, 1999; Creagh et al., 2010; Acevedo et al., 2010) with prismatic sections loaded under tension/compression cycles.

The data from Chai and Elayer (1999) are especially relevant, as those tests gradually increased tensile and compressive strains until overall prism buckling occurred. These data were based on test of axial columns under large strain amplitudes expected in the plastic hinge region of a ductile reinforced concrete wall. This experimental program is presented in section 2.4.2.

2.4.2 Experimental Program

Fourteen reinforced concrete column specimens were tested under an axial reversed cyclic tension and compression. The column specimens were mounted vertically in a steel reaction

frame where a quasi-static axial force was applied to the specimen using a double acting actuator. Figure 2.6 shows a photograph of the test setup for the specimen. With the exception of two specimens, the loading cycle consisted of an initial half-cycle of axial tensile strain followed by compression half cycle with a nominal target compressive strain 1/7 of the axial tensile strain unless the compression cycle was limited by the capacity of the actuator that was approximately 185 kips (823 kN). In the other two specimens, the target compressive strain was increased to 1/5 of the axial tensile strain. A load cycle is considered to be stable if the target compressive strain or the compression capacity of the actuator can be reached in three successive cycles without developing an excessive out-of- plane displacement in the specimen.

Figure 2.7 shows the reinforcement details for the test specimens. The test specimens were 4 x 8 in. rectangular in cross section (102 x 203 mm), with height-to-thickness ratios L_o/b = 11.75, 14.75, and 17.75. The length of the specimen L_o included the 5.5-in. (140-mm) steel brackets used for connection to the actuator. Two longitudinal reinforcement area ratios, namely, 2.1 and 3.8 percent, were investigated and provided by six No. 3 or six No. 4 deformed bars. A cover of 0.5 in. (12.7 mm) was used for the longitudinal reinforcement. Transverse ties fabricated from ¼ in. (6.4 mm) diameter cold drawn smoothed bars were provided at a spacing of six times the longitudinal bar diameter, i.e., 2.25 in. (57 mm) for No. 3 bars, and 3 in. (76 mm) for No. 4 bars. The close spacing of the transverse ties was intended to simulate the well-confined condition in the end regions of ductile walls and to prevent the local buckling of the longitudinal bars. To insure a proper transfer of the actuator force to the specimen, six 3/8 in. (9.5 mm) diameter all thread rods with a 10 in. (254 mm) anchorage length were added to the two ends of the specimen to increase the tensile capacity at the connection. In addition to the all-thread rods, two sets of steel plates, 2.5 in. (64 mm) wide by 1 in. (25 mm) thick, were used to externally confine the concrete in the end regions to insure that the transfer of the longitudinal bar forces to the concrete would not result in a local bond failure for the longitudinal reinforcement.

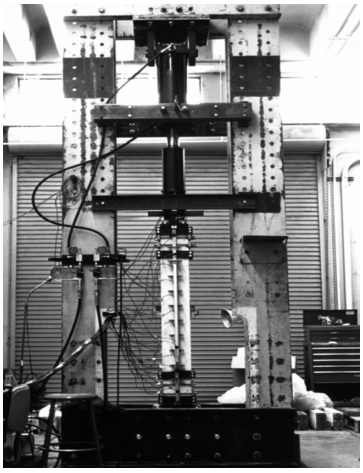

Figure 2.6 Experimental test setup.

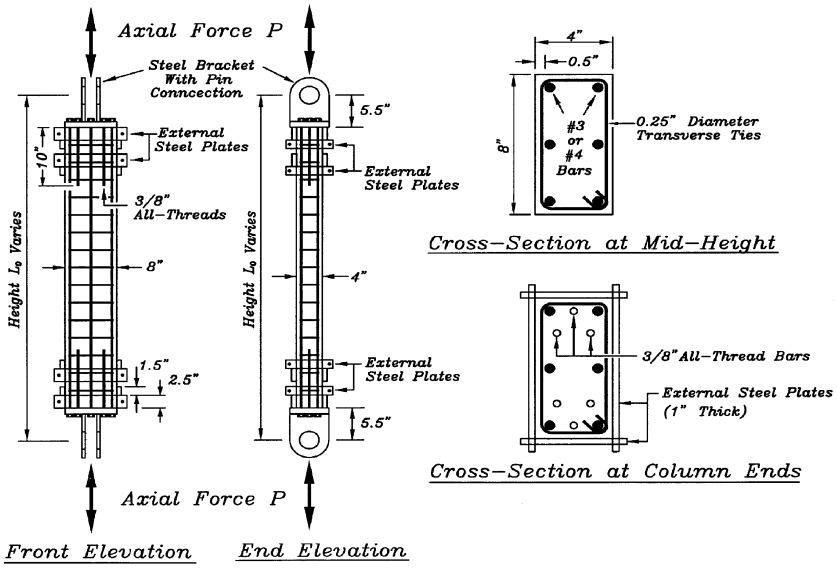

Figure 2.7 Reinforcement details for test specimens (1 in. = 25.4 mm).

Table 2.1 summaries the matrix for the test program.

Table 2.1 Test matrix.

Height-to-thickness ratio L_o/b	Longitudinal reinforcement ratio, percent	Transverse steel spacing, in. (mm)	No. of specimens tested
11.75	2.1	2.25 (57)	1
11.75	3.8	3.0 (76)	1
14.75	2.1	2.25 (57)	3
14.75	3.8	3.0 (76)	3
17.75	2.1	2.25 (57)	3
17.75	3.8	3.0 (76)	3

2.4.3 Material Properties

A normal weight concrete with an unconfined compressive strength of f'_c = 4,950 psi (34.1 MPa) was used for all specimens. The yield strengths of the longitudinal reinforcement were f_y = 51.8 and 66.0 ksi (357 and 455 MPa) for No. 3 and No. 4 bars, respectively, and the yield strength of the transverse ties was f_y = 99.0 ksi (683 MPa).

2.4.4 Results

Figure 2.8 compares results of Equation (2.10) with test data from prismatic sections that buckled following tensile strain excursions to $\in_{sm}$. All test specimens had pin-ended boundary conditions (k = 1) except the tests at $\in_{sm}= 0.04$, for which one end was fixed (k = 0.7). The results suggest that Equation (2.10) is a reasonable approximation to describe behavior of uniformly loaded prisms. (The available data could be represented equally well by a linear relation; however, such relation may unnecessarily penalize walls with $\in_{sm} > 0.04$).

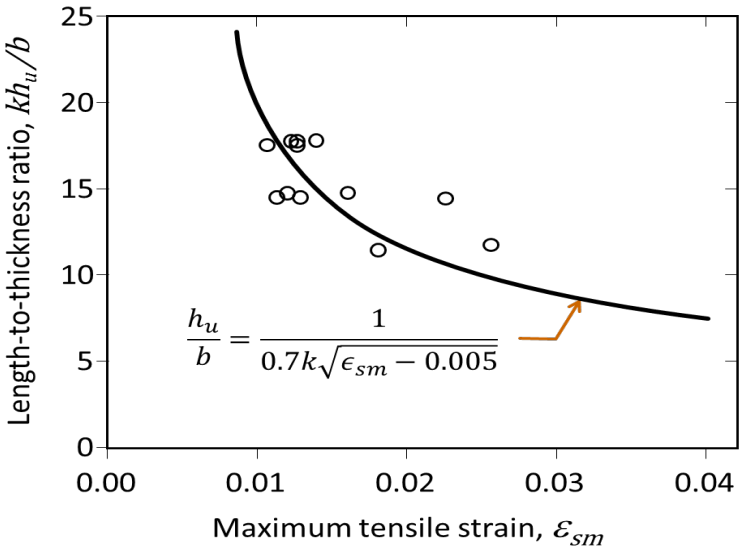

Figure 2.8 Buckling of prismatic sections reinforced as rectangular wall boundaries.

2.5 FLEXURAL COMPRESSION WALL TESTS

2.5.1 Thomsen and Wallace Wall Tests

2.5.1.1 Introduction

In zones where strong earthquake ground motions are anticipated, inelastic deformations may occur at the base of reinforced concrete walls. In order to exhibit stable inelastic response, the wall should be specially detailed at critical regions. Thomsen and Wallace (2004) conducted a combined experimental and analytical investigation to evaluate a displacement-based approach (Wallace and Moehle 1992; Wallace 1994) used to assess wall-detailing requirements.

2.5.1.2 Experimental Program

The laboratory test program include six wall specimens, approximately quarter-scale, including three with rectangular cross section (one with an opening), two with T-shaped cross section, and one with barbell-shaped cross section with an opening. Results for the walls with openings are presented elsewhere (Taylor et al., 1998).

2.5.1.3 Specimen Design

Figure 2.9 shows the specimens overall geometry. The walls were 12 ft (3.66 m) tall and 4 in. (102 mm) thick, with web and flange lengths of 4 ft (1.22 m). Floor slabs were provided at 3 ft (0.91 m) intervals over the height of the T-shaped walls.

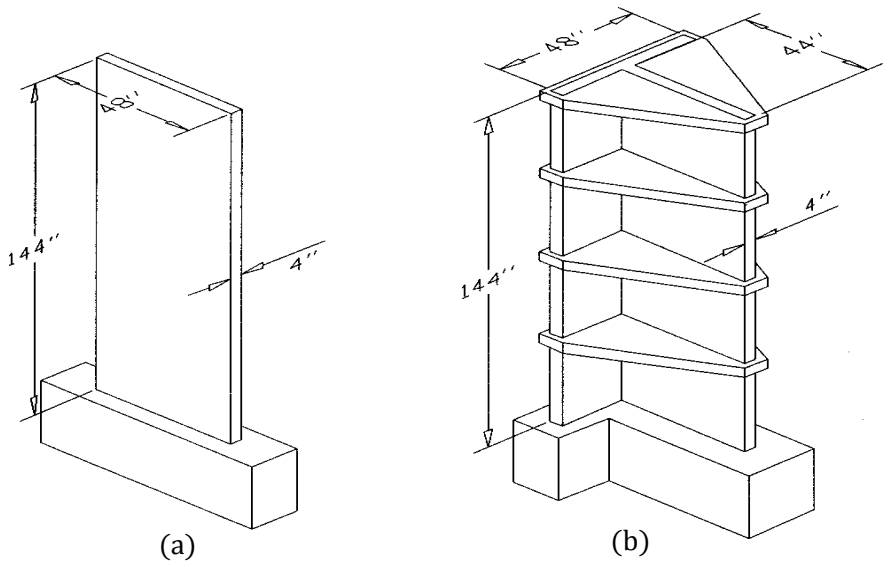

Figure 2.9 Overall geometry of specimens (a) RW1/RW2; (b) TW1/TW2 (1 in. = 25.4 mm).

A prototype building, representing a multistory office building in an area of high seismicity (for example Los Angeles), was used to assist in determining the wall geometry and reinforcing details for the testing program. The prototype building is six stories tall with a total height of 72 ft (21.9 m), and incorporates rectangular and T-shaped structural walls and moment-resisting frames to resist lateral and gravity loads (Figure 2.10).

Design actions on the walls were determined using the equivalent static lateral force procedure described in UBC-91.

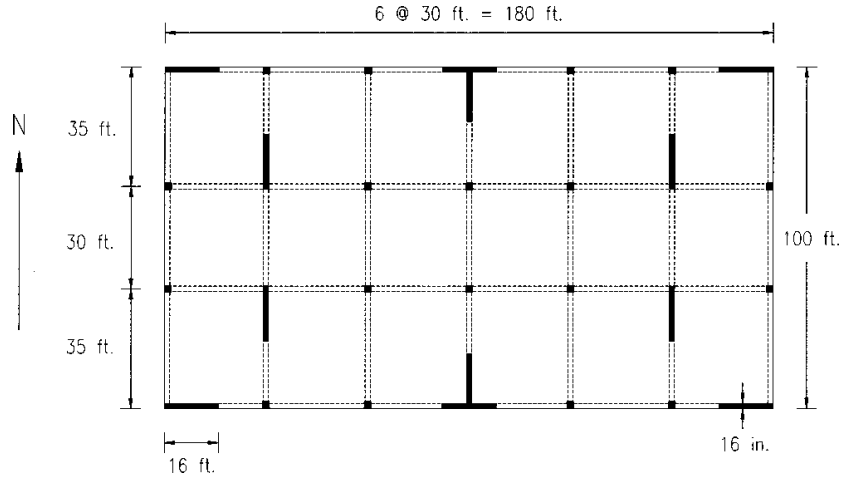

Figure 2.10 Prototype building (1 ft = 0.30 m).

The prototype rectangular wall is 16 in. (406 mm) thick and 16 ft (4.88 m) long with ten No. 11 (A_b=1.56in.^{2}; 1000 mm^2) boundary vertical bars and No. 5 (A_b=0.31in.^{2}; 200 mm^2) vertical and horizontal web reinforcement spaced at 12 in. (305 mm). Similar reinforcing quantities are used at the boundaries and within the webs for the T-shaped walls.

The wall specimens tested were approximately one-quarter scale representations of the prototype walls. Boundary vertical steel consisted of eight No. 3 (A_b=0.11in.^{2}; 71 mm^2) bars, whereas web bars were deformed No. 2 (A_b=0.049 in.^{2}; 32 mm^2). Areas of boundary and web steel were selected to be roughly equivalent to 1/16 (square of the scale factor) of those for the prototype walls so as to produce a similar neutral axis depth relative to the wall length in comparison with the prototype walls. The depth of the neutral axis for an axial load of $0.10A_g f'_c$ and an extreme fiber compression strain of 0.003 is 9.7 in. or $0.20l_w$ (246 mm) for the rectangular wall specimens. Neutral axis depths for an extreme fiber strain of 0.003 are 2 in. or $0.042l_w$ (51 mm) and 24.5 in. $0.51l_w$ (670 mm) for the flange in compression and tension, respectively, for the T-shaped wall specimens loaded parallel to the stem of the T.

Detailing requirements at the boundaries of the wall specimens were evaluated using the displacement-based design approach presented by Wallace (1994, 1995). In this approach, the design displacement is related to the curvature and strain demands at the critical section, and special transverse reinforcement is provided over the length of the wall cross section where the compression strain exceeds a critical value, typically taken as 0.003. A design roof drift equal to 1.5% of the wall height, or 2.16 in. (55 mm) was selected to determine the required transverse reinforcement at the wall boundaries for the test specimens. This drift was selected because it represents a reasonable upper bound drift level for structural wall buildings (Wallace and Moehle 1992), and more importantly for the test program, because transverse reinforcement was required at the wall boundaries (that is the extreme fiber compression strain exceeded the critical strain of 0.003). For a lower design drift, the lateral drift capacity of all the specimens would be limited by buckling of longitudinal reinforcement due to the relatively large spacing of the transverse reinforcement.

Figure 2.11 to Figure 2.13 show the cross sections of the test walls. Note that walls RW1 and TW1 have specially configured closely spaced transverse reinforcement in the wall boundaries. In contrast, the transverse reinforcement in RW2 and TW2 is not as well configured and is more widely spaced.

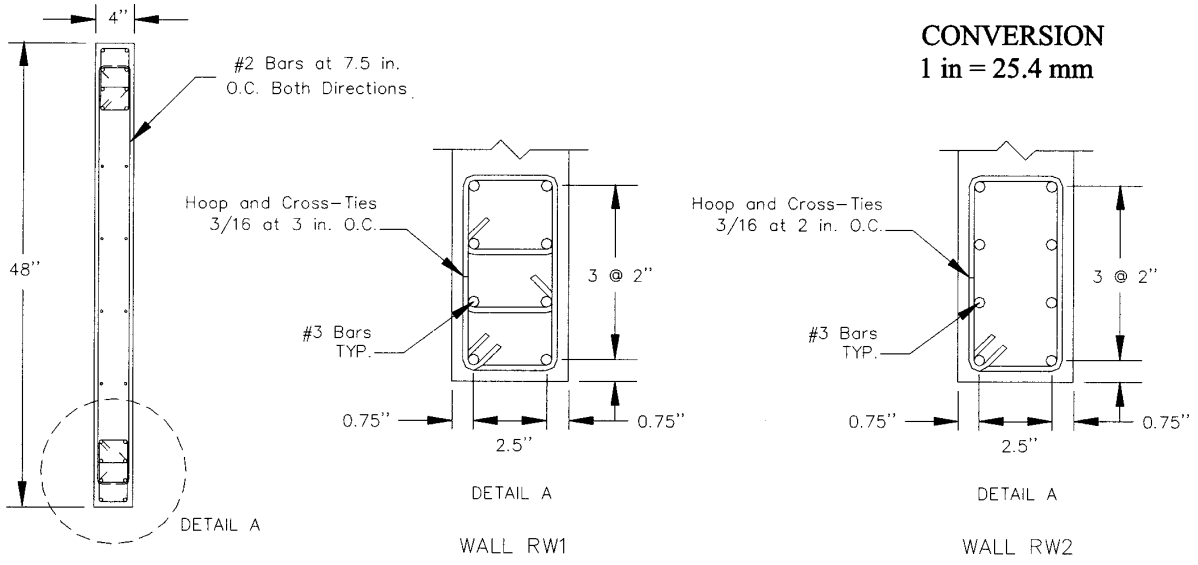

Figure 2.11 RW1 and RW2 reinforcing details.

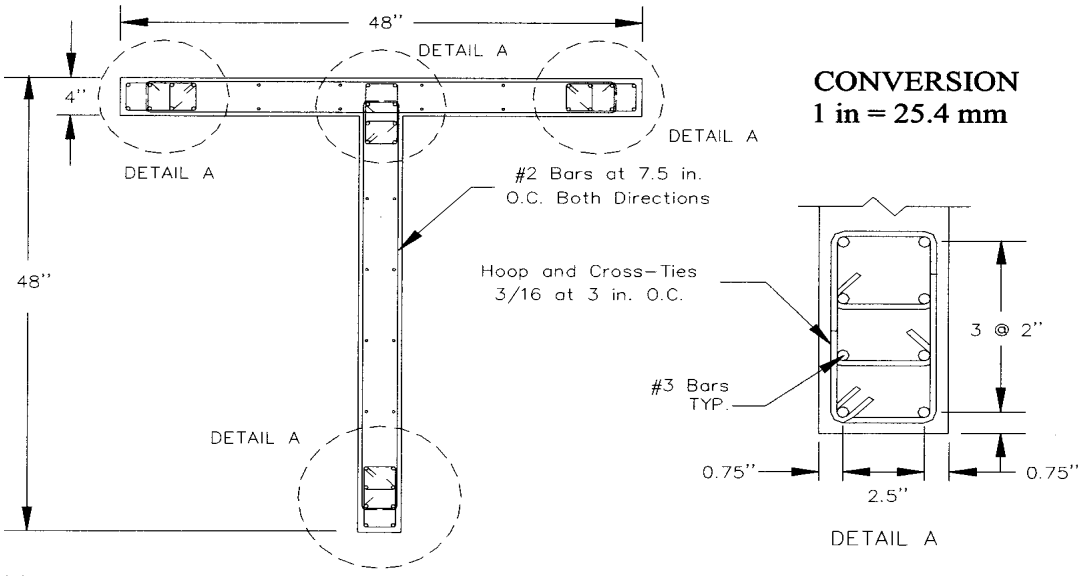

Figure 2.12 TW1 reinforcing details.

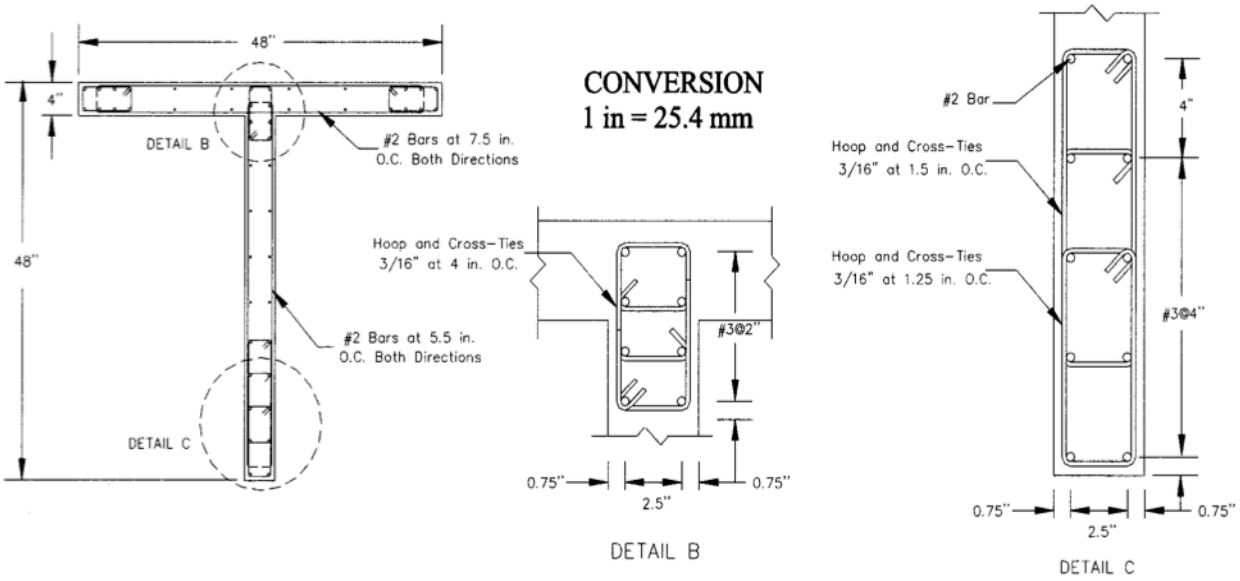

Figure 2.13 TW2 reinforcing details.

2.5.1.4 Material Properties

Design compressive strengths were 4,000 psi (27.6 MPa); however, strengths at the time of testing ranged from 4,150 to 8,460 psi (28.7 to 58.4 MPa) with mean compressive strengths at the base of the wall specimens (0 to 3 ft; 0 to 914 mm) of 4,580, 4,925, 6,330, and 6,050 psi (31.6, 34.0, 43.6, and 41.7 MPa) for Specimens RW1, RW2, TW1, and TW2, respectively. Three types of reinforcing steel were used in this study: (1) typical Grade 60 (414 MPa) deformed No. 3 (9.5 mm) bars for longitudinal reinforcement, (2) deformed No. 2 (6.4 mm) bars for uniformly distributed horizontal and vertical web reinforcement, and (3) 3/16 in. (4.75 mm) diameter smooth wire for boundary transverse reinforcement. The boundary transverse reinforcement was heat treated to produce material properties similar to those of Grade 60 (414 MPa) reinforcing steel. For comparison between analytical and experimental strain profiles, the moment-curvature

relations are based on the measured material properties of each specimen. The stress-strain relations proposed by Saatcioglu and Razvi (1992) for unconfined and confined concrete are used for analysis.

2.5.1.5 Test Setup

The wall specimens were tested in an upright position, as shown in Figure 2.14.

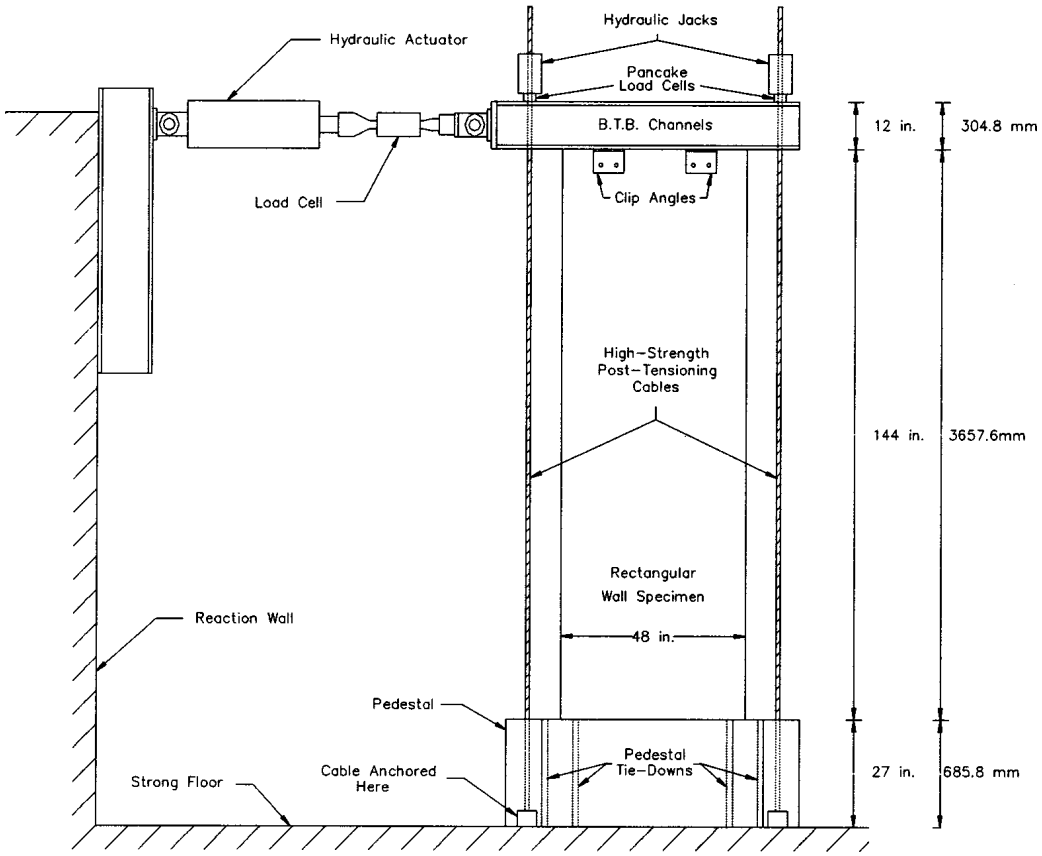

Figure 2.14 Specimen test setup – RW1 and RW2.

A specially fabricated steel load transfer assembly was used to transfer both axial and lateral loads to the wall specimen. An axial load of approximately $0.10A_g f'_c$ was applied at the top of the wall by hydraulic jacks mounted on top of the load transfer assembly. The axial stress was maintained constant throughout the duration of each test. Cyclic lateral displacements were applied to the walls by a 125 kip (556 kN) hydraulic actuator mounted horizontally to a reaction wall 12 ft (3.66 m) above the base of the wall. Out-of-plane support was provided to prevent twisting of the wall during testing.

Figure 2.15 shows the displacement history applied to RW2. The displacement history for RW1 was similar to RW2, except that the four additional cycles at 1% and 1.5% drift were not applied after applying the first two cycles at 1.5% drift. Displacement histories for TW1 and TW2 are identical to RW2.

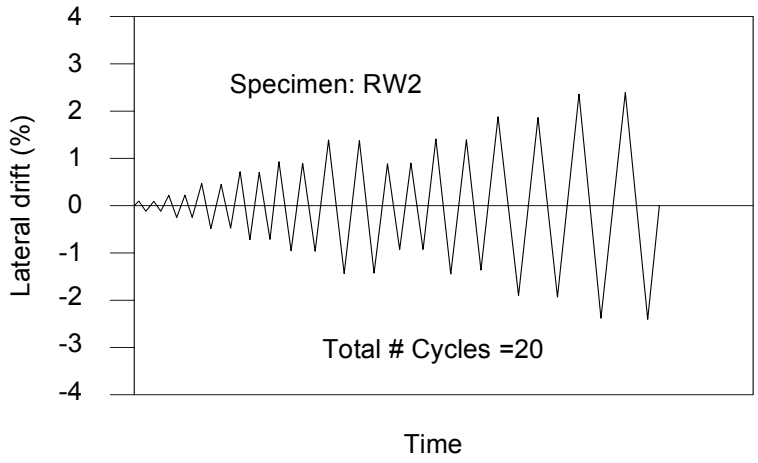

Figure 2.15 Applied displacement history.

2.5.1.6 RW1 Specimen: Analytical and Experimental Strain Profiles

The plastic hinge approach and numerical integration of the curvature diagram are used to analyze RW1. The curvature integration approach does not incorporate effects of reinforcement slip from the foundation. Absence of the slip component is likely to result in underestimation of flexibility near the yield point. The moment-curvature relation (Figure 2.16) is calculated with XTRACT based on the material properties indicated in section 2.5.1.4.

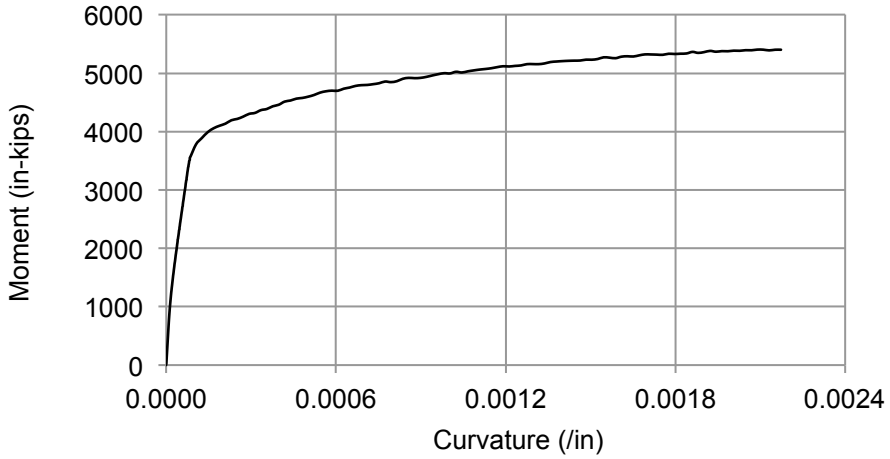

Figure 2.16 Moment-curvature relation for RW1 wall (1 in. = 25.4 mm; 1 in-kips = 0.11 kN-m).

Figure 2.17 shows the experimental cyclic response. For comparison, the lateral load required to produce the nominal moment at the base of the wall is also shown.

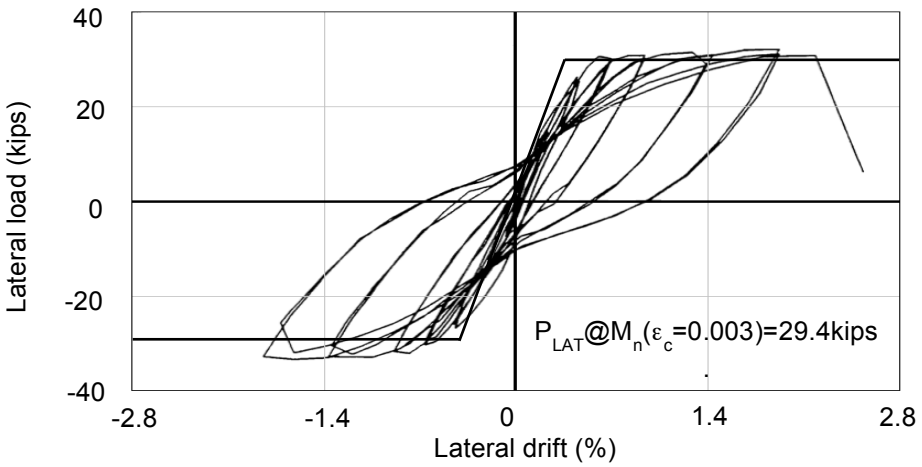

Figure 2.17 Cyclic response for RW1 wall (1 kip = 4.45 kN).

Figure 2.18 shows the calculated section strain profiles for four drift levels, obtained from both approaches.

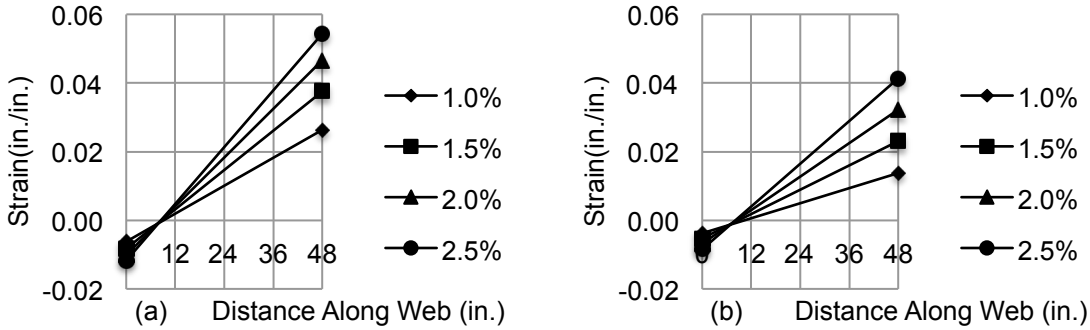

Figure 2.18 Strain profiles for RW1 wall: (a) curvature integration; (b) plastic hinge approach l_p=0.5l_w (1 in. = 25.4 mm).

The plastic hinge model strains are less than the numerical integration model strains for all displacement amplitudes. Figure 2.19 compares measured and calculated strain profiles using the plastic hinge approach (l_p=0.5l_w). The analysis strain distribution shows good accuracy with respect to the experimental values.

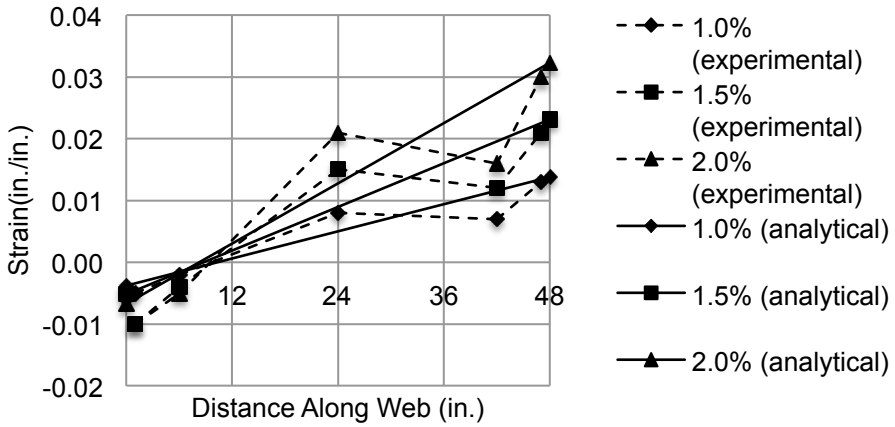

Figure 2.19 Measured strain versus analysis strain distribution plastic hinge approach l_p=0.5l_w (1 in. = 25.4 mm).

Figure 2.20 shows the strain profile at the base of the wall when the simplified plastic hinge method Equation (2.20) is used. The results of the simplified plastic hinge model are very similar to those of the more refined plastic-hinge model.

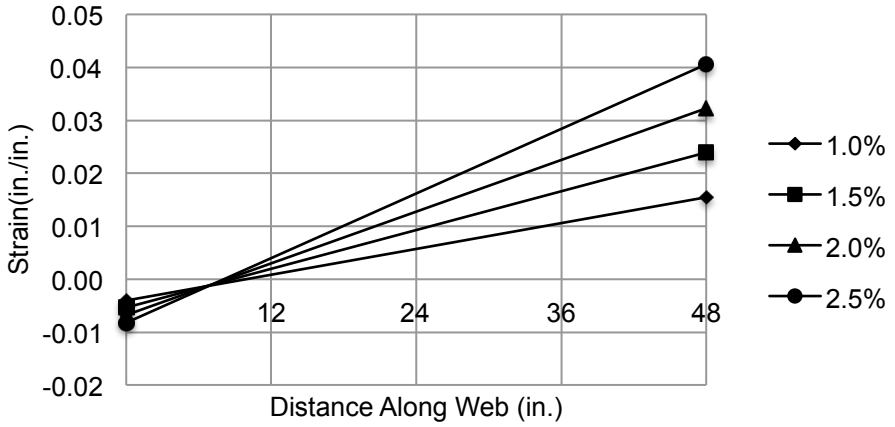

Figure 2.20 Strain profiles for RW1 wall from Equation (2.20) l_p=0.5l_w (1 in. = 25.4 mm).

2.5.1.7 RW2 Specimen: Analytical and Experimental Strain Profiles

The analytical models similarly were applied to test wall RW2. Figure 2.21 shows the calculated moment-curvature relation.

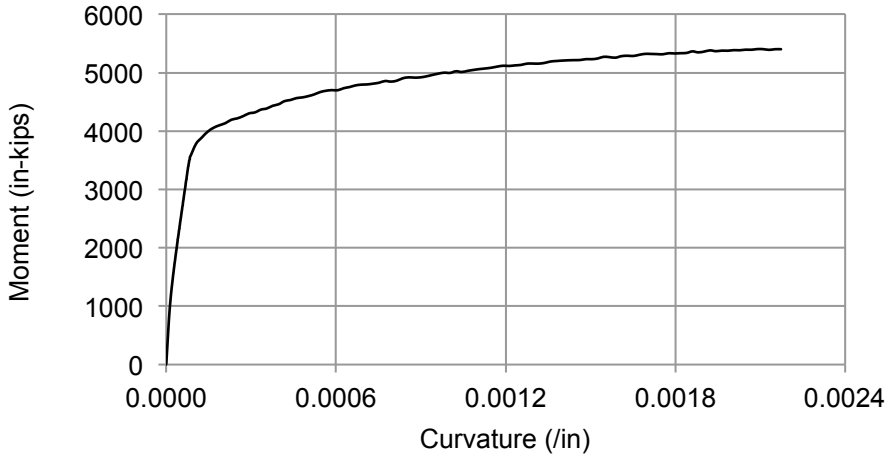

Figure 2.21 Moment-curvature relation for RW2 wall (1 in. = 25.4 mm; 1 in-kips = 0.11 kN-m).

Figure 2.22 shows the experimental cyclic response. For comparison, the lateral load required to produce the nominal moment at the base of the wall is also shown.

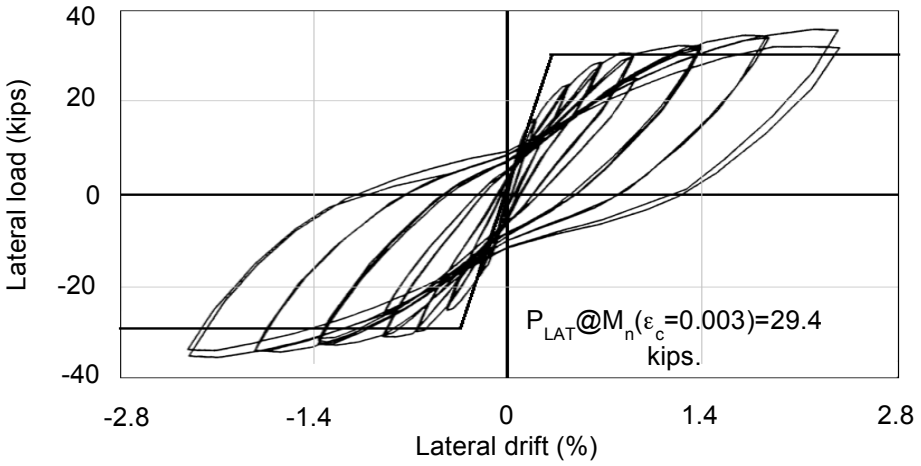

Figure 2.22 Cyclic response for RW2 wall (1 kip = 4.45 kN).

Figure 2.23 shows the calculated section strain profiles for four drift levels, obtained from both approaches. Results are similar to those obtained for RW1.

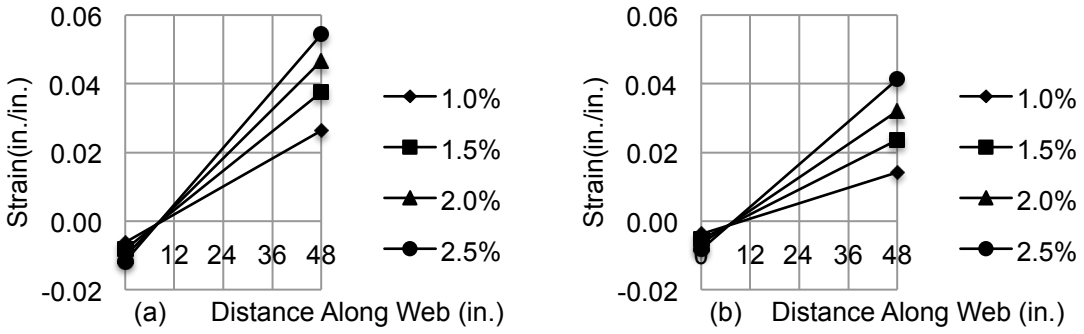

Figure 2.23 Strain profiles for RW2 wall: (a) curvature integration; (b) plastic hinge l_p=0.5l_w (1 in. = 25.4 mm).

Figure 2.24 compares measured and calculated strain profiles using the plastic hinge approach (l_p=0.5l_w). The analysis strain distribution shows good accuracy with respect to the experimental values.

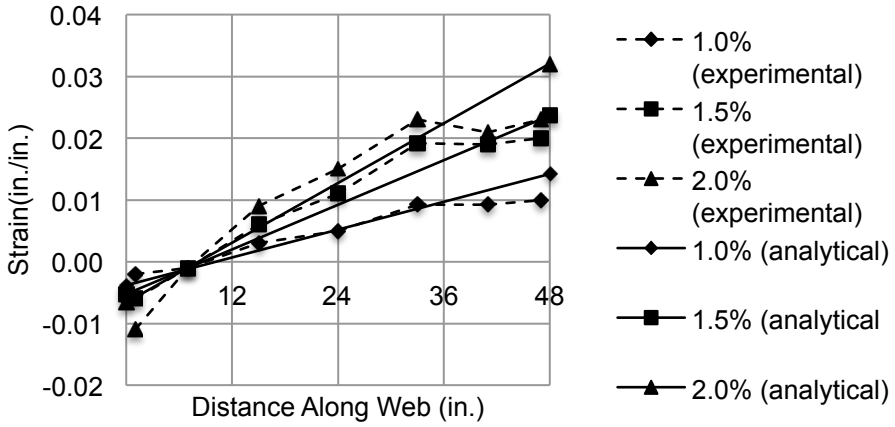

Figure 2.24 Measured strain versus analysis strain distribution plastic hinge approach l_p=0.5l_w (1 in. = 25.4 mm).

Figure 2.25 shows the strain profile at the base of the wall when the simplified plastic hinge method Equation (2.20) is used. Again, the analysis strain profile obtained from this simplified method is similar to the one obtained from the more complex plastic hinge procedure.

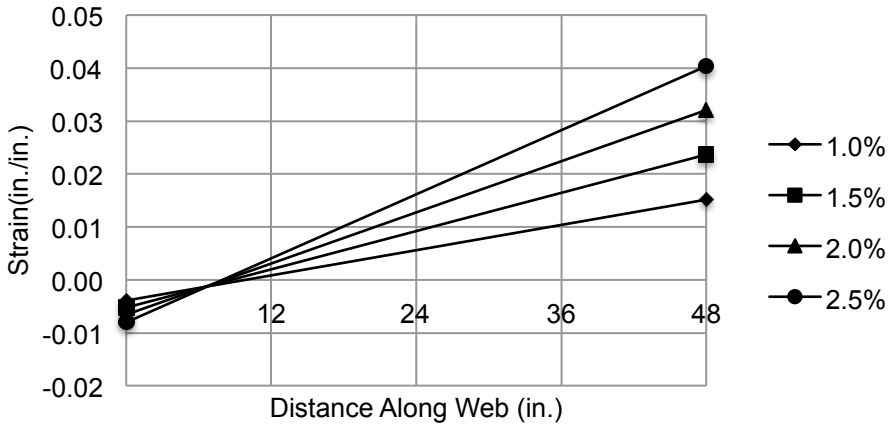

Figure 2.25 Strain profiles for RW2 wall from Equation (2.20) l_p=0.5l_w (1 in. = 25.4 mm).

2.5.1.8 TW1 Specimen: Analytical and Experimental Strain Profiles

Figure 2.26 shows the calculated moment curvature relations.

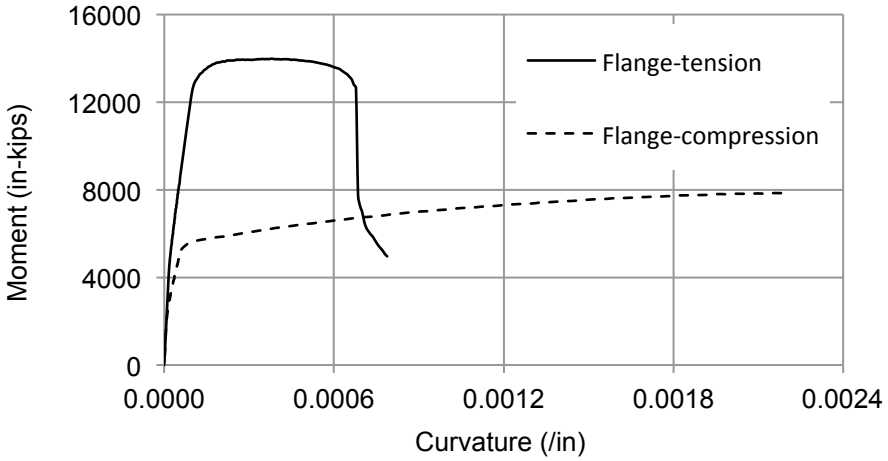

Figure 2.26 Moment-curvature relations for TW1 wall (1 in. = 25.4 mm; 1 in-kips = 0.11 kN-m).

To use numerical integration of the curvature diagram, it is necessary to have an ascending post-yielding branch in the moment-curvature relation. This is a requirement in order to spread the nonlinearity over the plastic hinge zone. If there were a strain-softening relation, the wall would unload past the yield point, with plastic curvature becoming concentrated at a point, which is physically impossible. In Figure 2.26 softening post-yielding behavior is observed for the case of flange in tension. Therefore, for TW1 wall only the plastic hinge approach is used to calculate the analytic response.

Figure 2.27 shows the experimental cyclic response, where positive load (or displacement) means wall flange in tension. For comparison, the lateral load required to produce the nominal moment at the base of the wall is also shown.

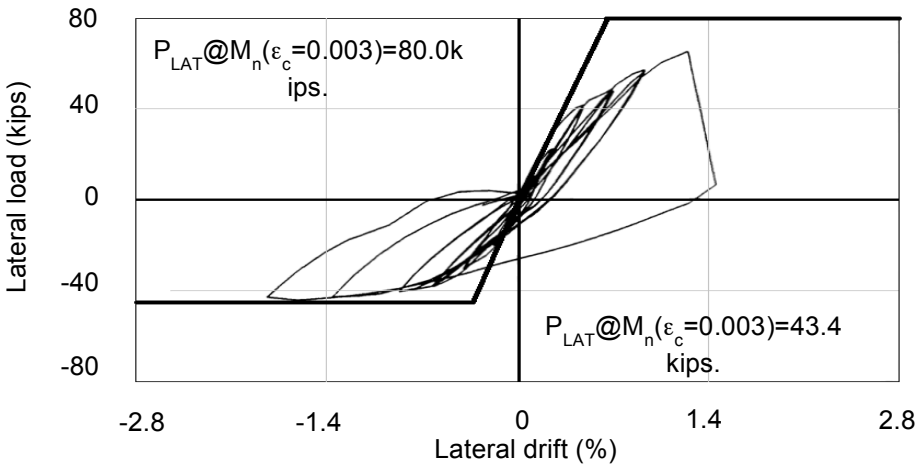

Figure 2.27 Cyclic response for TW1 wall (1 kip = 4.45 kN).

Figure 2.28 shows the calculated section strain profiles for three drift levels, obtained from the plastic hinge approach with l_p=0.5l_w.

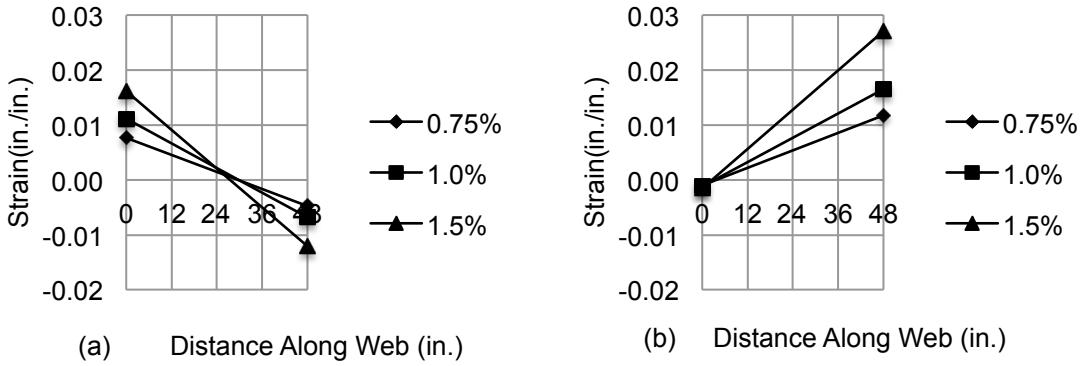

Figure 2.28 Strain profiles for TW1 (PH approach): (a) flange in tension; (b) flange in compression (1 in. = 25.4 mm).

Figure 2.29 compares measured and calculated strain profiles using the plastic hinge approach (l_p=0.5l_w). The accuracy of the analysis strain distribution is not as good as for the case of rectangular walls, and it seems to overestimate the maximum tensile strain for all drift levels, especially for the case of flange in tension. This over-prediction of the strain profile is introduced by the modeling, which assumes the entire flange is effective in both compression and tension, and it is expected to decrease as the drift ratio increases (Thomsen and Wallace, 2004).

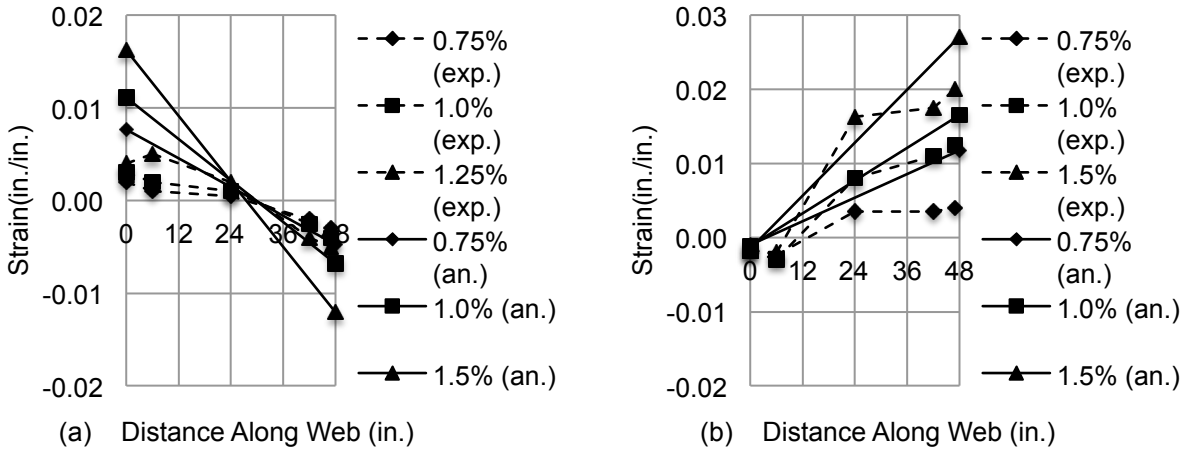

Figure 2.29 Experimental and plastic hinge (l_p=0.5l_w) strain profiles for TW1 wall (a) flange in tension; (b) flange in compression (1 in. = 25.4 mm).

Figure 2.30 shows the strain profile at the base of the wall when the simplified plastic hinge method Equation (2.20) is used. Again, the analysis strain profile obtained from this simplified method is similar to the one obtained from the more complex plastic hinge procedure.

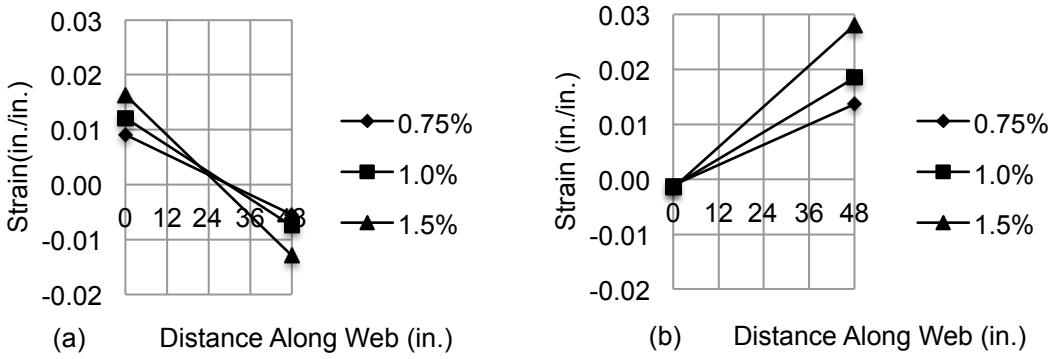

Figure 2.30 Strain profiles for TW1 Equation (2.20) l_p=0.5l_w (a) flange in tension; (b) flange in compression (1 in. = 25.4 mm).

2.5.1.9 TW2 Specimen: Analytical and Experimental Strain Profiles

As with TW1, only the plastic-hinge approach is used. Figure 2.31 shows the moment-curvature relations.

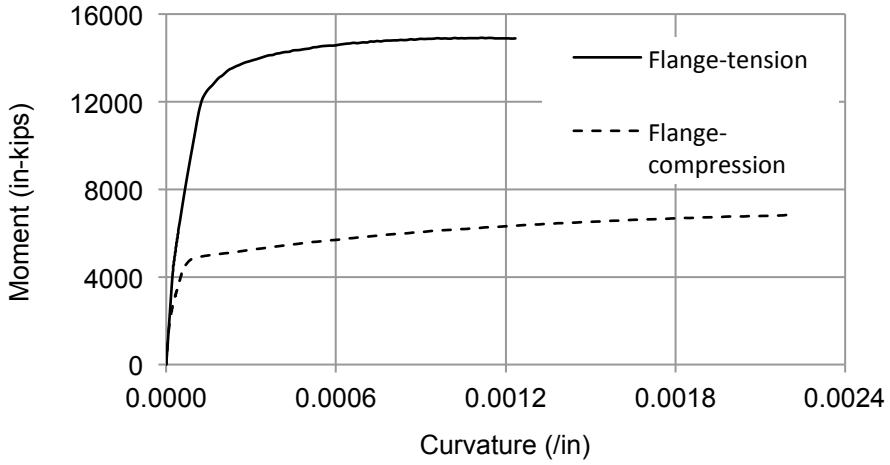

Figure 2.31 Moment-curvature relations for TW2 wall (1 in. = 25.4 mm; 1 in-kips = 0.11 kN-m).

Figure 2.32 shows the experimental cyclic response. Again positive load (or displacement) means wall flange in tension. For comparison, the lateral load required to produce the nominal moment at the base of the wall is also shown.

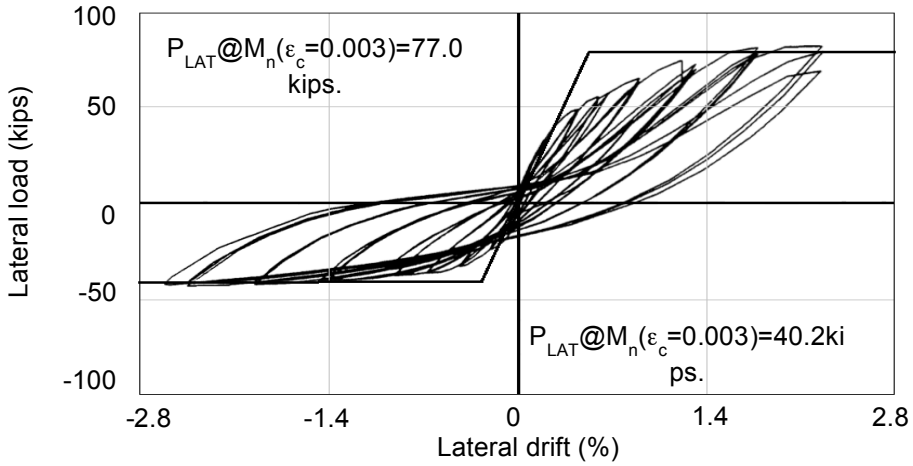

Figure 2.32 Cyclic response for TW2 wall (1 kip = 4.45 kN).

Figure 2.33 shows the calculated section strain profiles for four drift levels, obtained from the plastic hinge approach with l_p=0.5l_w.

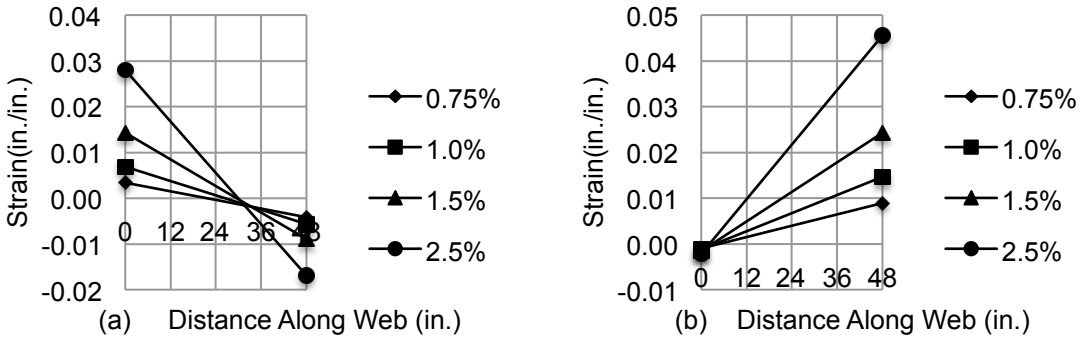

Figure 2.33 Strain profiles for TW2 (PH approach): (a) flange in tension; (b) flange in compression (1 in. = 25.4 mm).

Figure 2.34 compares measured and calculated strain profiles using the plastic hinge approach (l_p=0.5l_w). The analysis strain distribution shows good accuracy with respect to the experimental values when the flange is in compression. For the case of flange in tension, it seems to overestimate the maximum tensile strain for all drift levels, as was observed for TW1.

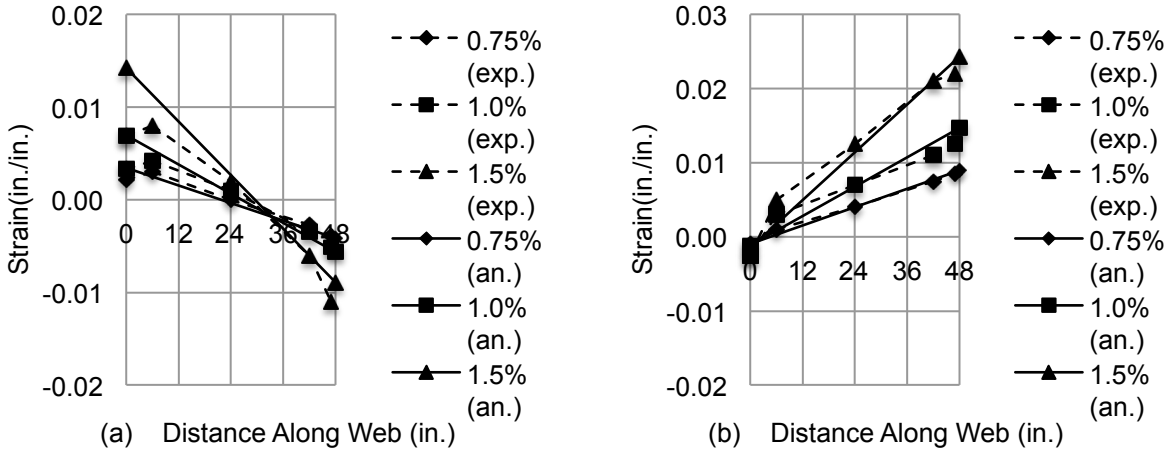

Figure 2.34 Experimental and plastic hinge (l_p=0.5l_w) strain profiles for TW2 wall (a) flange in tension; (b) flange in compression (1 in. = 25.4 mm).

Figure 2.35 shows the strain profile at the base of the wall when the simplified plastic hinge method Equation (2.20) is used. As before, the analysis strain profile obtained from this simplified method is similar to the one obtained from the more complex plastic hinge procedure.

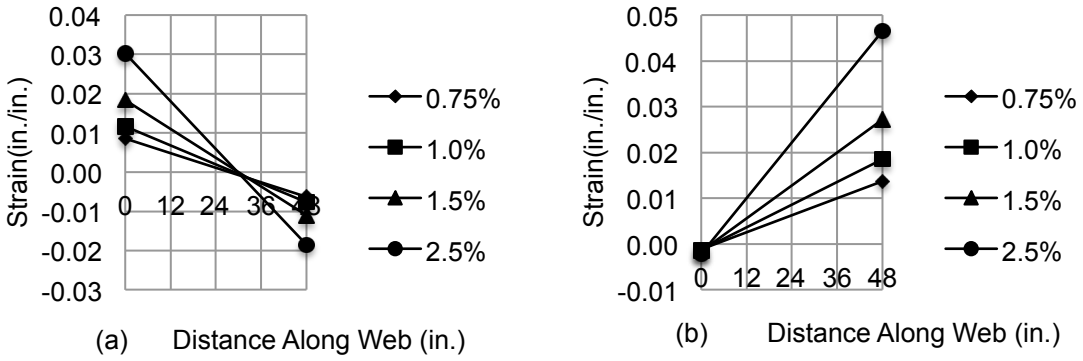

Figure 2.35 Strain profiles for TW2 Equation (2.20) l_p=0.5l_w (a) flange in tension; (b) flange in compression (1 in. = 25.4 mm).

2.5.1.10 Failure Description and Buckling Analysis

Figure 2.36 shows photos of the damaged boundary regions for all four specimens.

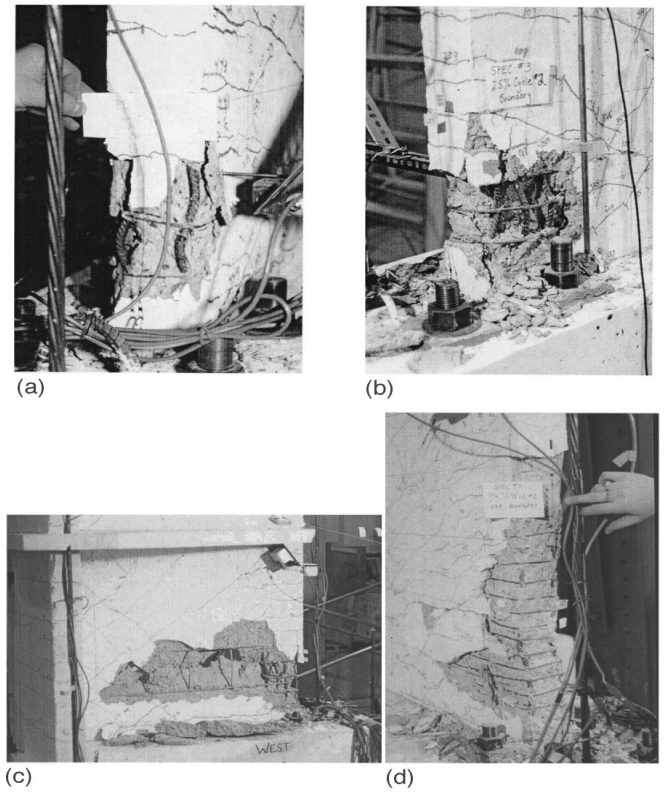

Figure 2.36 Specimens failure, after Thomsen and Wallace (1995) (a) RW1 (b) RW2 (c) TW1 (d) TW2.

For specimen RW1, two cycles at 2.0% lateral drift were completed prior to significant loss in lateral load capacity at approximately 2.5% drift due to buckling of longitudinal reinforcement. This failure mode was anticipated given the relatively large spacing ($8d_b$) of the hoops and crossties at the wall boundary.

Behavior of specimen RW2 was very similar to RW1, except lateral load capacity was maintained even after two complete cycles at 2.5% lateral drift. The improved behavior is attributed to the closer spacing of the hoops ($5.33d_b$) at the wall boundaries, which delayed the onset of buckling of the longitudinal reinforcement.

ACI 318-99 uses a maximum hoop/crosstie spacing of $6d_b$ to suppress buckling of vertical bars. Spacing of special boundary element transverse reinforcement exceeded this limit for RW1 and TW1 ($8d_b$), was slightly less than this for RW2 ($5.33d_b$), and considerably less than this for TW2 ($4d_b$).

For TW1, as a result of the poor detailing provided at the boundary of the web opposite the flange, the lateral load capacity dropped suddenly at an applied lateral drift of approximately 1.25%. The loss in lateral load capacity is attributed to the large spacing of transverse reinforcement used at the wall boundary, which was inadequate to suppress bucking of the longitudinal reinforcement.

Transverse reinforcement at the boundary opposite the flange was placed at a closer spacing and over an increased depth of the cross section for Specimen TW2 compared with specimen TW1 and specimen TW2 did not experience a loss of lateral load capacity until the second and third cycles at a lateral drift level of approximately 2.5%. The test was stopped midway through the first cycle at a lateral drift level of 3.0%. Under displacements that cause compression in the wall web, the entire web boundary element began to experience an out-of-plane stability failure at approximately 0.75% lateral drift.

From Equation (2.9), the required tensile strain in boundary bars to onset the out-of-plane buckling is given by Equation (2.21).

$$\in_{sm} = \kappa\xi \left(\frac{\pi b_{cr}}{k h_u}\right)^2 + 0.005 \tag{2.21}$$

Adopting values $\kappa = 0.8$, $\sqrt{\xi} = 0.5$ and k=0.5, Equation (2.21) for walls with two curtains of reinforcement becomes:

$$\in_{sm} = 7.90 \left(\frac{b_{cr}}{h_u}\right)^2 + 0.005 \tag{2.22}$$

From Equation (2.22), for all the specimens $\in_{sm} = 7.90 \left(\frac{4}{32}\right)^2 + 0.005 = 0.13$. Reported strains are far below this value for all cases.

If spalling occurs first, the parameters values adopted for Equation (2.21) are $\kappa = 1$, $\sqrt{\xi} = 0.5$ and k=0.5. Then $\in_{sm}$ is given by Equation (2.23).

$$\in_{sm} = 9.87 \left(\frac{b_{cr}}{h_u}\right)^2 + 0.005 \tag{2.23}$$

Using the core dimension of 2.5 in, Equation (2.23) gives $\in_{sm} = 9.87 \left(\frac{2.5}{32}\right)^2 + 0.005 = 0.065$, which occurs at a curvature ϕ_u.

From Equation (2.20), the drift ratio at a curvature ϕ_u is given by Equation (2.24)

$$DR = \emptyset_u \; l_p \tag{2.24}$$

The required drift ratio for each specimen to reach $\in_{sm} = 0.065$ is shown in Table 2.2.

Table 2.2 Required drift ratio to reach $\in_{sm} = 0.065$.

Specimen	ϕu, $in.^{-1}$ (mm^{-1})	DR
RW1	0.0017 (0.00007)	4.1%
RW2	0.0017 (0.00007)	4.1%
TW1	0.0014 (0.00006)	3.4%
TW2	0.0014 (0.00006)	3.4%

For all specimens with exception of TW2, failure was triggered by local buckling of longitudinal reinforcement, due to the spacing of the hoops and crossties at the wall boundary, for drift ratios smaller than 2.5% (TW1 had the poorest behavior with failure at 1.25% drift ratio).

Only TW2 was able to develop a drift ratio greater than 2.5% (due to the closer hoop spacing of $4d_b$) and close to the value given in Table 2.2. Thus, the observation of out-of-plane buckling of TW2 is reasonably consistent with the presented theory and the spalled condition of the boundary element before failure.

2.5.2 Oesterle et al. Wall Tests

2.5.2.1 Introduction

Oesterle et al. (1976) conducted a combined experimental and analytical investigation to develop design criteria for reinforced concrete structural walls in earthquake resistant buildings. The primary purpose of the investigation was to determine the ductility, energy dissipation and strength of the walls. As a part of the experimental program, reversing loads were applied to isolated walls. The results of nine tests were presented.

One of the rectangular specimens (R2) experienced out of plane buckling (after thirty-five loading cycles) at an average drift ratio of 2.8%. Only this case will be presented and analyzed in the following sections, according to the buckling theory of section 2.2.

2.5.2.2 Experimental Program

An experimental program was developed to investigate the behavior of large isolated reinforced concrete walls. Test specimens were approximately 1/3-scale representations of full-size walls, although no specific prototype walls were modeled. Controlled variables included in the tests were the shape of the wall cross-section, the amount of main flexural reinforcement and the amount of hoop reinforcement around the main flexural reinforcement. In addition, one wall was subjected to monotonic loading and one wall was repaired and retested. Table 2.3 provides a summary of test specimen details.

Table 2.3 Summary of test specimens.

Specimen	Shape	Reinforcement (%)			
		ρ_f	ρ_h	ρ_n	ρ_s
R1	Rectangular	1.47	0.31	0.25	-
R2	Rectangular	4.00	0.31	0.25	2.07
B1	Barbell	1.11	0.31	0.29	-
B3	Barbell	1.11	0.31	0.29	1.28
B4 (monotonic loading)	Barbell	1.11	0.31	0.29	1.28
B2	Barbell	3.67	0.63	0.29	-
B5	Barbell	3.67	0.63	0.29	1.35
B5R (repaired specimen)	Barbell	3.67	0.63	0.29	1.35
F1	Flanged	3.89	0.71	0.3	-

Where:

- ρ_f Ratio of main flexural reinforcement area to gross concrete area of boundary element
- ρ_h Ratio of horizontal shear reinforcement area to gross concrete area of a vertical section of wall web
- ρ_n Ratio of vertical web reinforcement area to gross concrete area of a horizontal section of wall web

- ρ_s Ratio of effective volume of confinement reinforcement to the volume of core in accordance with Eq. A.4 of ACI 318-71

Figure 2.37 shows the dimensions of test specimens. Figure 2.38 shows the nominal cross-sectional dimensions of these sections.

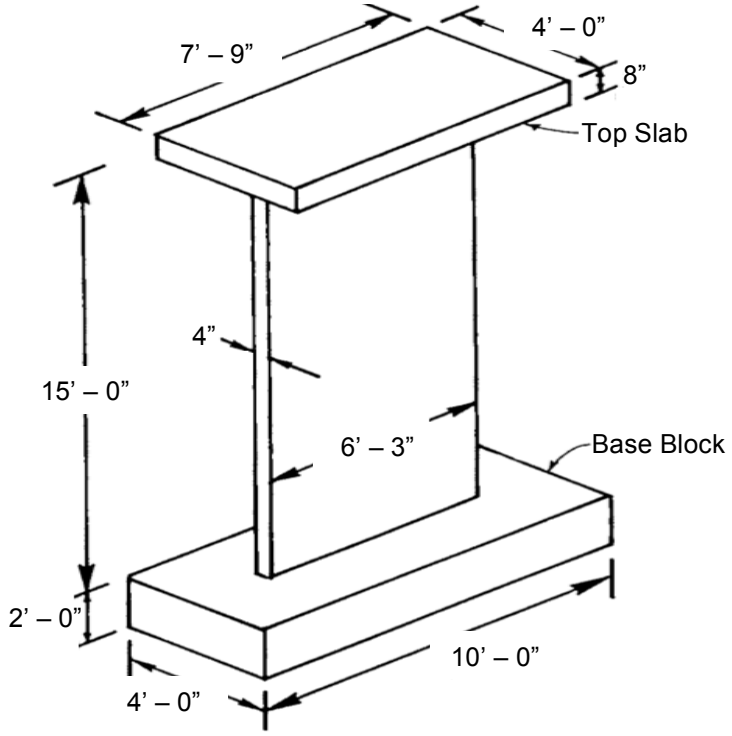

Figure 2.37 Nominal dimensions of test specimens with rectangular cross section (1 ft= 0.30 m).

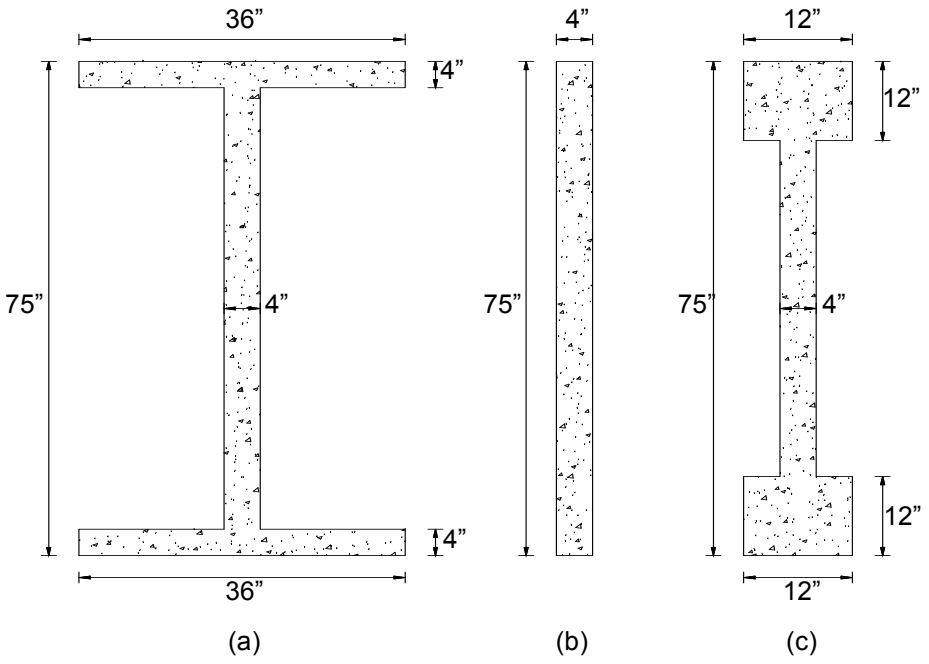

Figure 2.38 Nominal cross-sectional dimensions of test specimens (1 in. = 25.4 mm).

In proportioning the walls, the design moment was calculated following procedures in the ACI Building Code. Strain hardening of the steel was neglected. Horizontal shear reinforcement was provided so that the calculated design moment would be developed. Shear reinforcement was provided to satisfy the ACI Building Code. Design yield stress of the steel was 60 ksi (414 MPa) and design concrete strength was 6,000 psi (41.4 MPa).

The test specimens were constructed in six vertical lifts. Each specimen was loaded as a vertical cantilever with forces applied through the top slab. The test specimens were loaded in a series of increments. Each increment consisted of three complete reversed cycles. About three increments of force were applied prior to initial yielding. Subsequent to initial yielding, loading was controlled by deflections in 1 in. increments.

Free vibration tests were conducted at selected stages as the number and magnitude of loading increments applied to the specimen increased. These tests were carried out to determine the frequency and damping characteristics of the walls.

2.5.2.3 Specimen Design

The overall dimensions of specimen R2 was shown in Figure 2.37. The "boundary element" was taken to extend 7.5 in. (191 mm) from each end of the wall. The percentage of flexural reinforcement (Table 2.3) was chosen to give a section moment capacity corresponding to high nominal shear stress.

Nominal vertical web reinforcement provided in the wall was 0.25% of the gross concrete area of the horizontal wall section. This is the minimum amount permitted by the 1971 ACI Building Code. Once the nominal vertical reinforcement percentage were selected, bar sizes and locations were determined based on modeling and construction requirements.

The moment capacity of the section was calculated according to Section 10.2 of the 1971 ACI Building Code. Design yield stress of the steel was taken as 60 ksi, and design concrete strength was taken as 6,000 psi. Strain hardening of the steel was neglected for section design.

The vertical reinforcement was continuous from the base block to the bottom of the top slab. The vertical bars were lap spliced with the top slab bars in the top 32 in. (0.81 m) of the wall.

Horizontal shear reinforcement was designed to develop the calculated ACI moment capacity. The shear design was made according to Section 11.16 of the 1971 ACI Building Code. The horizontal reinforcement was placed at a constant spacing over the height of the wall.

Horizontal steel in the boundary elements (rectangular hoop and supplementary crosstie reinforcement) were provided in accordance with Section A.6.4 of the 1971 ACI Building Code. This confinement was placed at a spacing of 1.33 in. (34 mm) over the first 6 ft (1.83 m) of the wall. Ordinary column ties were used over the remaining height of the wall.

Anchorage for the horizontal steel was provided by embedment in the boundary elements plus a standard 90° hook around the outer main flexural steel.

Figure 2.39 shows the reinforcing details. Confinement reinforcement was detailed according to Section A.6.4.3 of the 1971 ACI Building Code. A ten bar diameter extension was used on all confinement steel hooks. Each end of the supplementary crossties had a semicircular hook.

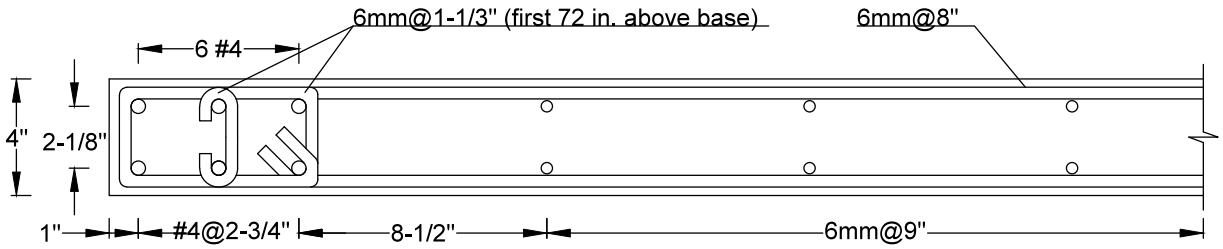

Figure 2.39 R2 specimen reinforcing details (1 in. = 25.4 mm).

2.5.2.4 Material Properties

The concrete compressive strength was determined from compressive tests on 6x12-in. (152x305 mm) cylinders. No. 4 bars conforming to ASTM A615 Grade 60 designation were used as reinforcement. Deformed 6 mm hot rolled bars with properties similar to Grade 60 were also used. Measured properties of the materials are:

- Concrete
  - f'_c= 6,700 psi (46 MPa)
- Steel (No. 4 bars)
  - f_u= 102.7 ksi (708 MPa)
  - f_y= 65.3 ksi (450 MPa)
- Steel (6mm bars)
  - f_u= 100.2 ksi (691 MPa)
  - f_y= 77.6 ksi (535 MPa)

The stress-strain relations proposed by Saatcioglu and Razvi (1992) for unconfined and confined concrete are used for analysis.

2.5.2.5 Test Setup

Figure 2.40 shows the apparatus used for walls testing.

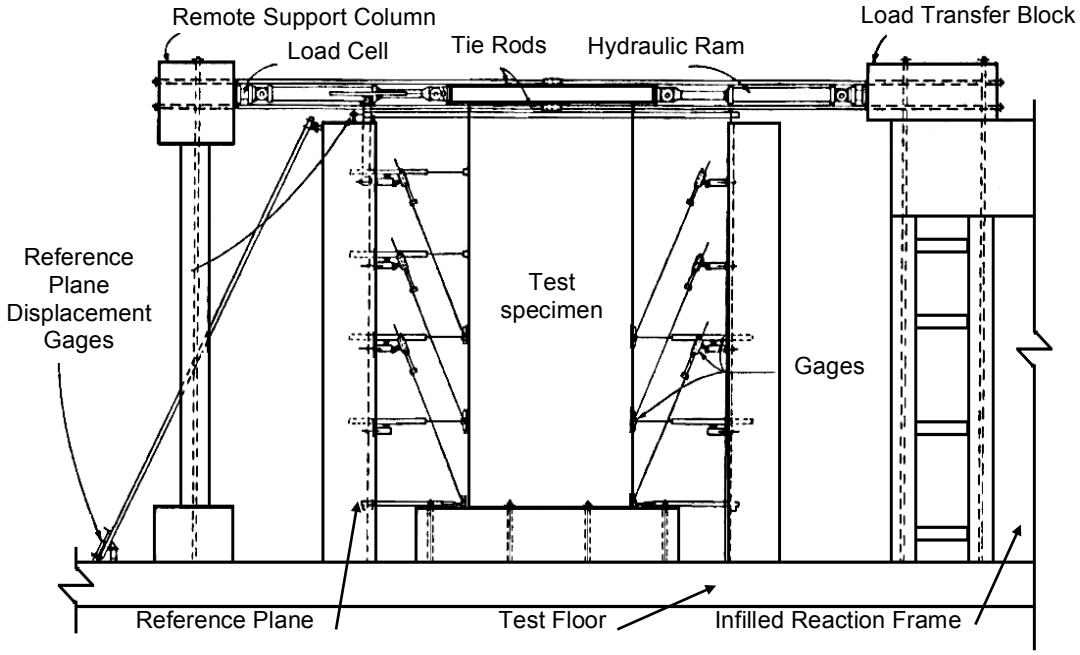

Figure 2.40 Wall testing apparatus.

Each test specimen was post-tensioned to the floor using eight 1-3/8 in. (34.9 mm) diameter stress steel bars. Loads were applied to the specimen as a vertical cantilever with concentrated forces at the top. Hydraulic rams on each side of the specimen alternately applied force to first one side then the other side of the top slab. Reactions from the applied loads were transferred to the test floor through a large infilled reaction frame. This load transfer occurred directly when the rams closest to the reaction frame were activated, and indirectly through the remote support column and tie rods, wen the rams farthest from the reaction frame were activated. A system of one or two rams on each side of the specimen was used depending on the anticipated capacity of each specimen. The hydraulic rams have a capacity of 200 kips (890 kN) and a stroke of 36 in. (0.91 m). At each end of the ram, a clevis bracket and pin arrangement formed a link assembly.

For specimen R2, the test consisted of 39 loading cycles. Figure 2.41 shows the applied displacement history.

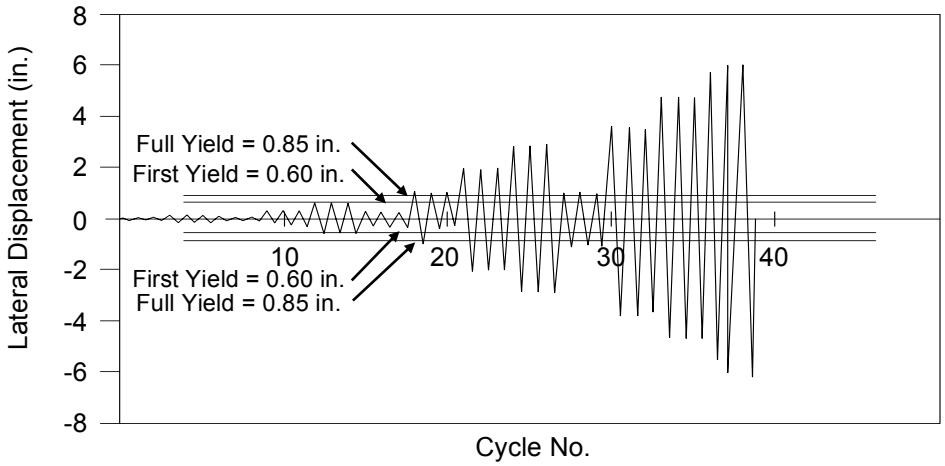

Figure 2.41 Applied displacement history (1 in. = 25.4 mm).

2.5.2.6 Analytical and Experimental Strain Profiles

Only the plastic hinge approach is used. The moment-curvature relation (Figure 2.42) is calculated with XTRACT based on the material properties indicated in section 2.5.2.4.

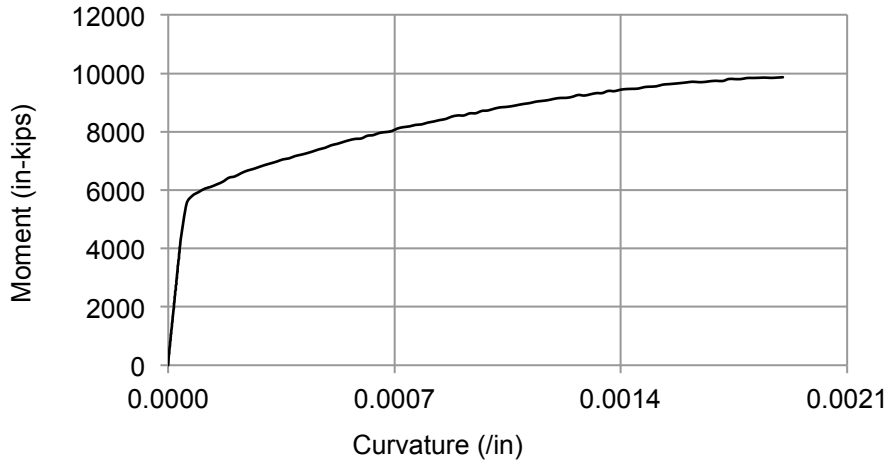

Figure 2.42 Moment-curvature relation for R2 wall (1 in. = 25.4 mm; 1 in-kips = 0.11 kN-m).

Figure 2.43 shows the experimental cyclic response.

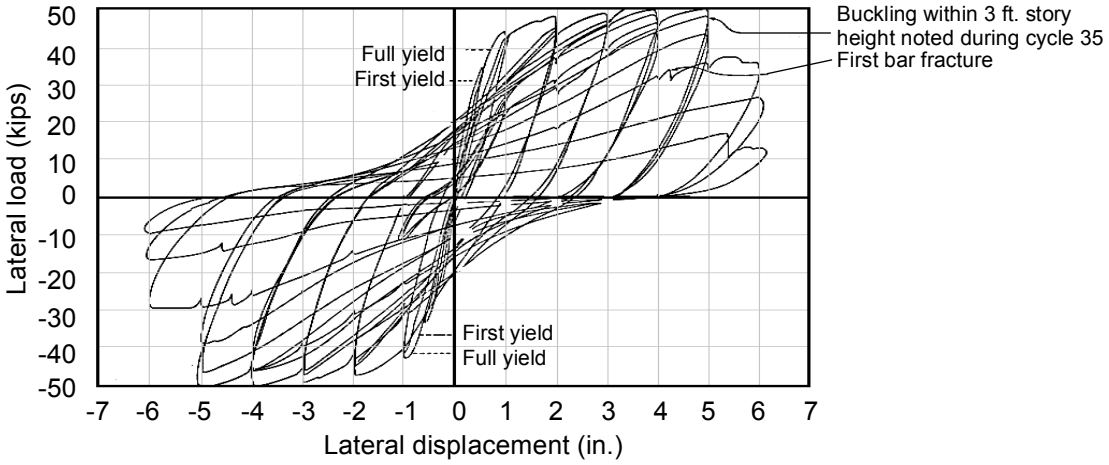

Figure 2.43 Cyclic response for R2 wall (1 kip = 4.45 kN).

The lateral instability indicated in Figure 2.43 occurs at an average drift ratio of 2.8% during Cycle 35. Figure 2.44 shows the calculated section strain profiles for four drift levels.

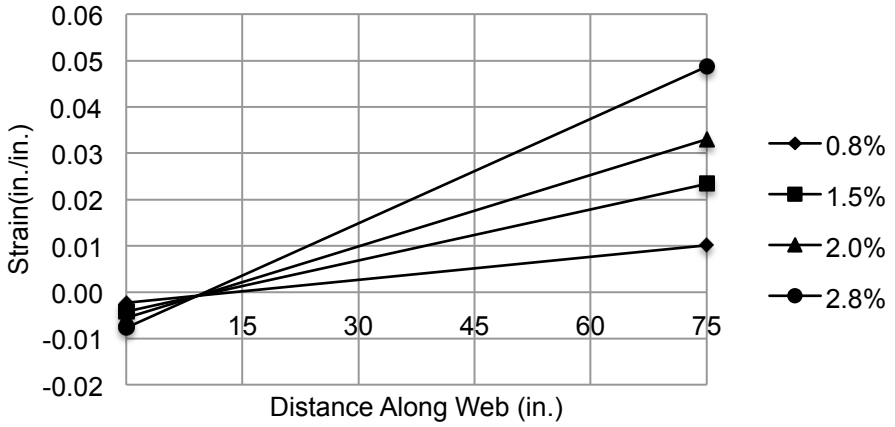

Figure 2.44 Strain profiles for R2 wall using plastic hinge approach l_p=0.5l_w (1 in. = 25.4 mm).

Figure 2.45 compares an experimental and analytical strain profile at an average drift ratio of 0.8%. Experimental strain profiles at higher drifts are not available for the wall base. The analysis strain distribution shows good accuracy with respect to the experimental values.

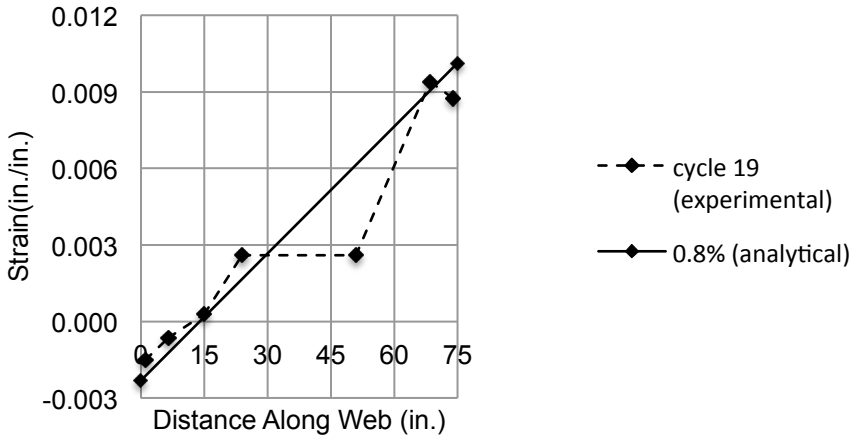

Figure 2.45 Measured strain versus analysis strain distribution (plastic hinge approach l_p=0.5l_w) (1 in. = 25.4 mm).

Figure 2.46 shows the strain profile at the base of the wall when the simplified plastic hinge method Equation (2.20) is used. The results of the simplified plastic hinge model are very similar to those of the more refined plastic-hinge model.

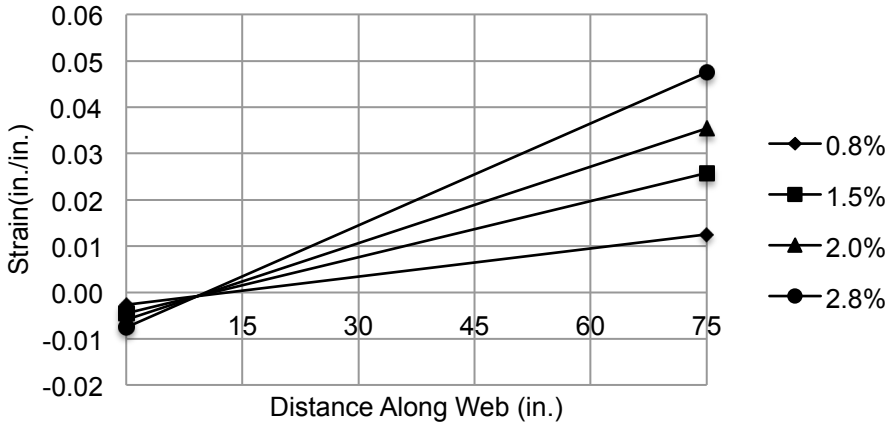

Figure 2.46 Strain profiles for R2 wall from Equation (2.20) l_p=0.5l_w (1 in. = 25.4 mm).

2.5.2.7 Failure Description and Buckling Analysis

The first significant flexural cracking occurred in Cycle 4 at a load of 15 kips (66.7 kN). The flexural cracking in the end regions was very finely distributed due to the close spacing of confinement steel. These flexural cracks progressed into coarsely distributed diagonal and horizontal cracks in the web. The cracks from the opposite directions of loading intercept each other. These cracks segment the web into large pieces. Several horizontal cracks completely traversed the width of the wall. The horizontal cracks formed at the levels of the horizontal steel in the web, which was at 8 in. (203.2 mm) on center.

In the first 3 in. deflection Cycle 25, it was noted that the cracks in the compression zone remained open 0.003 in. (0.076 mm). First indication of crushing of the outer shell at the base of

the wall had been noted in Cycle 22. A significant increase in spalling and flaking along the horizontal cracks was observed during the 3 in. deflection cycles.

During Cycle 28, a 1 in. (25.4 mm) deflection cycle, bowing of the compression end was observed. The compression boundary element was 0.25 in. (6.4 mm) out of plane at a point 3 ft-6 in. (1.1 m) above the base. Although this bowing progressed further with each cycle the load carrying capacity of the wall remained stable. After Cycle 32, the compression end of the wall was 3 in. (76.2 mm) out of plane at point 3 ft-6 in. (1.1 m) above the base. Figure 2.47 shows the specimen after Cycle 32.

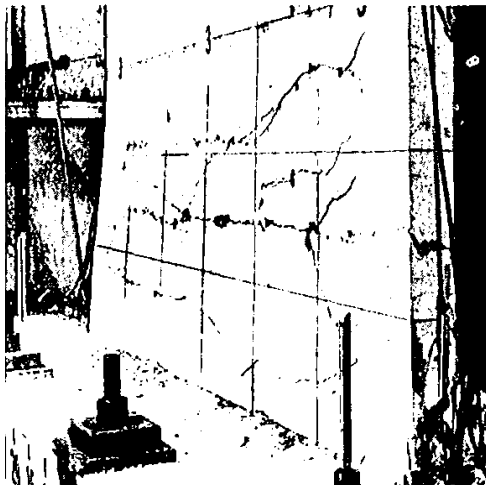

Figure 2.47 Lateral displacement of compression zone after 4 in. deflection for R2 specimen.

The test was stopped after Cycle 32 and lateral bracing was added to the test step-up. An omni-direction ball caster was placed against the face of the each boundary element at a level 3 ft-6 in. (1.1 m) above the base. This simulated lateral support at approximately the first story height.

The test was continued with the third 4 in. (101.6 mm) deflection Cycle 33. Considerable grinding and spalling along web cracks occurred during the 4 in. deflection cycles. Also, the end hooks of several horizontal bars started to open during the 4 in. cycles.

The maximum measured load, -48.8 kips (216.6 kN), occurred in Cycle 34 at a -5 in. deflection.

In Cycle 35, a large out of plane displacement of the compression zone within the lower 3 ft-6 in. (1.1 m) height was observed and the load carrying capacity of the wall decreased. The maximum negative load in the third cycle of the 5 in. (127.0 mm) deflection increment was 79% of the maximum in the first cycle.

Several bars fractures in Cycle 37 and out of plane displacement of the compression zones progressed further. Considerable crushing and loss of concrete occurred in subsequent cycles and the load carrying capacity continued to decrease.

The specimen sustained at least 80% of the maximum measured load through 14 complete inelastic cycles. The last inelastic loading increment in which the load was sustained at or above 80% of the maximum for all 3 cycles was at ±4 in. (±101.6 mm).

Buckling analysis is performed now. Adopting values $\kappa = 0.8$, $\sqrt{\xi} = 0.5$ and k=0.5, then Equation (2.22) can be used to estimate the required tensile strain in the boundary reinforcement to trigger the lateral instability. Therefore, $\in_{sm} = 7.90\left(\frac{4}{42}\right)^2 + 0.005 = 0.08$. Reported strains are below this value.

Due to considerable spalling occurred during the 4 in. deflection cycles, then Equation (2.23) can be used for this analysis. Using the core dimension of 2.13 in., Equation (2.23) gives $\in_{sm} = 9.87\left(\frac{2.13}{42}\right)^2 + 0.005 = 0.03$. From Figure 2.44, this strain is reached at an average drift ratio of 2.0%. From experimental data, this drift occurred during Cycle 31. Important out of plane displacement was observed in the lower portion of the wall during this cycle. Therefore, it seems likely to explain the wall lateral instability by crushing first and then lateral buckling according to the theory presented in section 2.2.

3 Alto Huerto Building

3.1 GEOMETRY

Alto Huerto building is located in Las Margaritas #1328, San Pedro de la Paz, Chile (latitude: -36.83690475273046, longitude: -73.10302734375). The structure was severely damaged after Chile earthquake on February 27th, 2010. The building was designed during 2007-2008 and constructed in 2009. It has fifteen stories and two subterranean levels. The seismic force-resisting system is composed of reinforced concrete walls of 7.87 in. (200 mm) typical thickness. The gravity force-resisting system comprises the reinforced concrete walls plus some interior reinforced concrete columns. The typical story height is 8.37 ft (2.55 m). There are some discontinuities in the vertical members in the first story with respect to the upper stories. For example, walls K and Ñ (and other walls) step back from the building perimeter by approximately 6.5 ft (2 m), resulting in reduced wall length in the first story compared with typical stories above. The building sustained a variety of apparent damage during the 2010 earthquake, with main damage characterized by wall crushing in the first story or in subterranean levels. Some walls, and in particular the first story wall along line Ñ, showed apparent out-of-plane buckling (Figure 1.1). Figure 3.1 shows the typical plan view.

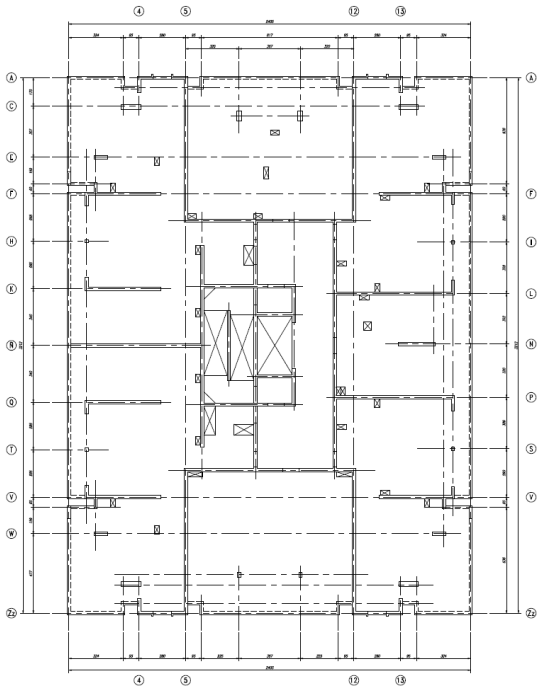

Figure 3.1 Alto Huerto building (San Pedro de la Paz-Chile) – Typical plan view.

Figure 3.2 shows the first-story plan view.

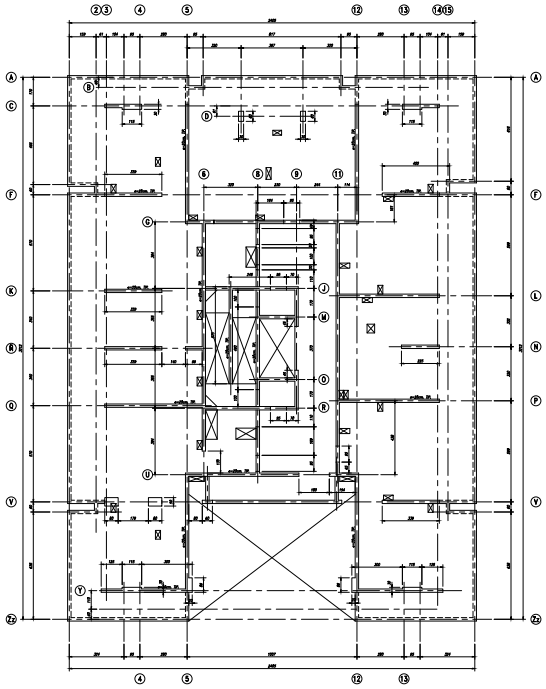

Figure 3.2 Alto Huerto building (San Pedro de la Paz-Chile) – First story plan view.

3.2 ANALYSIS AND DESIGN STANDARDS

Gravity and seismic loads were calculated following the Chilean standards NCh 1537 Of. 1986 and NCh 433 Of. 1996. Reinforced concrete members were designed according to ACI 318 (2005).

3.3 DESIGN SPECTRUM

The parameters used in the building seismic design according to NCh 433. Of. 1996 are:

- Building category C
- Seismic zone 3
- Soil type III
- Damping ratio 5%

NCh 433. Of. 1996 response spectrum analysis was performed, according to Equations (3.1) to (3.3).

$$S_\alpha = \frac{IA_0\alpha}{R^*} \tag{3.1}$$

$$\alpha = \frac{1 + 4.5\left(\frac{T_n}{T_0}\right)^p}{1 + \left(\frac{T_n}{T_0}\right)^3} \tag{3.2}$$

$$R^* = 1 + \frac{T^*}{0.1T_0 + \frac{T^*}{R_0}} \tag{3.3}$$

Where:

- S_α Pseudo acceleration
- I Importance factor = 1 for building category C
- A_0 Peak ground acceleration = 0.4 g for seismic zone 3
- g Acceleration of gravity, 386 in./s^2 (9.81 m/s^2)
- T_n Mode nth vibration period (s)
- T_0 Soil dependent parameter = 0.75 (s) for soil type III
- p Soil dependent parameter = 1 for soil type III
- T^* Vibration period of the mode with greatest equivalent mass in the analysis direction (s)
- R_0 Response modification factor = 11

Figure 3.3 shows the elastic response obtained from Equations (3.1) to (3.3).

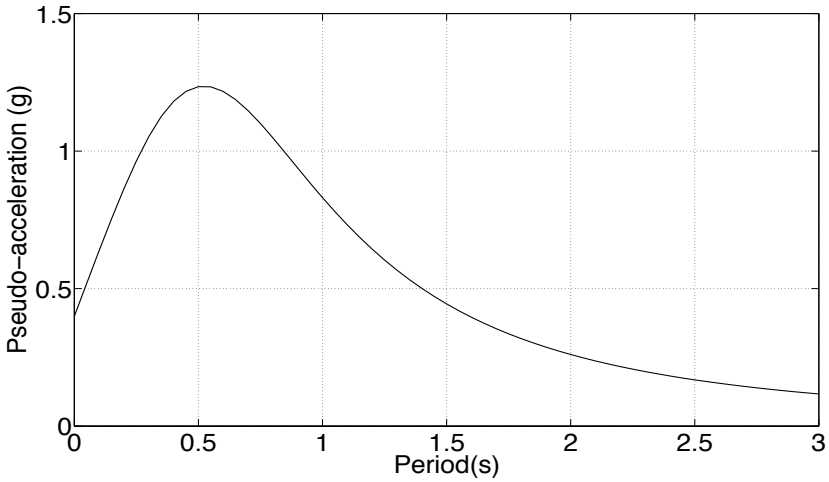

Figure 3.3 NCh 433 Of. 1996 elastic response spectrum (*R=1).**

3.4 RECORDED GROUND MOTION

Instruments recorded the ground acceleration during the February 27th 2010 Chile earthquake in a location close to Alto Huerto building (Colegio San Pedro, San Pedro de la Paz). Figure 3.4 to Figure 3.6 show the acceleration records for the three measured directions.

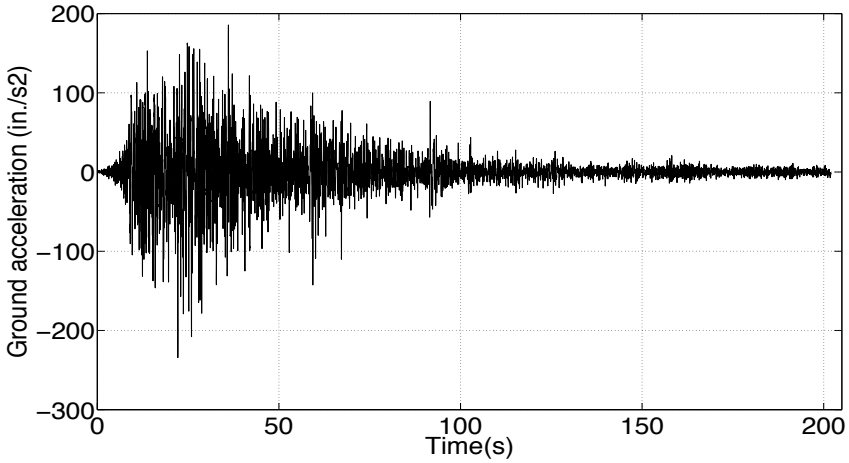

Figure 3.4 Corrected ground motion San Pedro de la Paz – EW direction (1 in.=25.4 mm).

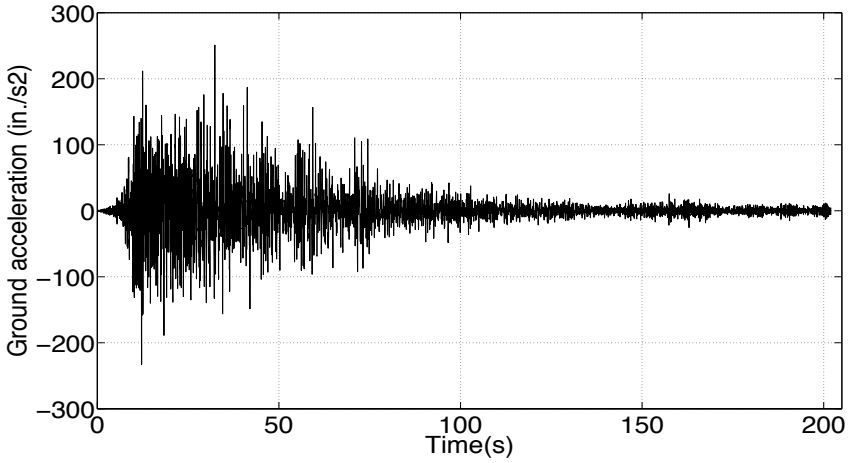

Figure 3.5 Corrected ground motion San Pedro de la Paz – NS direction (1 in.=25.4 mm).

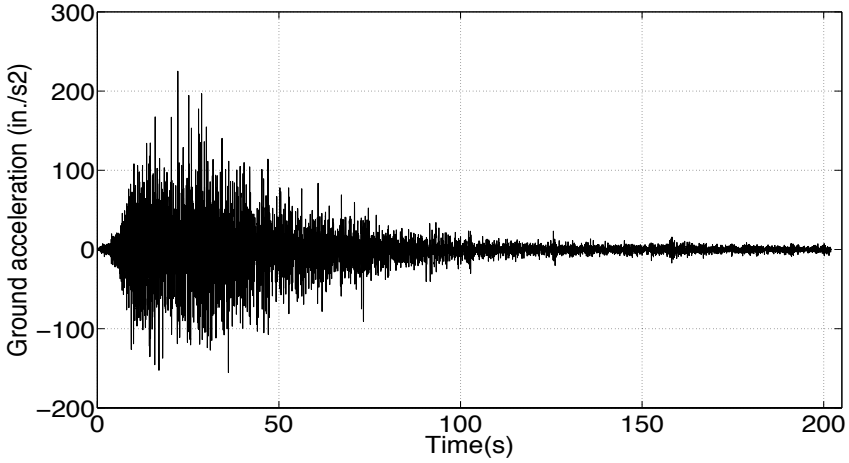

Figure 3.6 Corrected ground motion San Pedro de la Paz – UD direction (1 in.=25.4 mm).

Figure 3.7 to Figure 3.9 show the pseudo acceleration, pseudo velocity, and the displacement response spectrum (2% damping ratio).

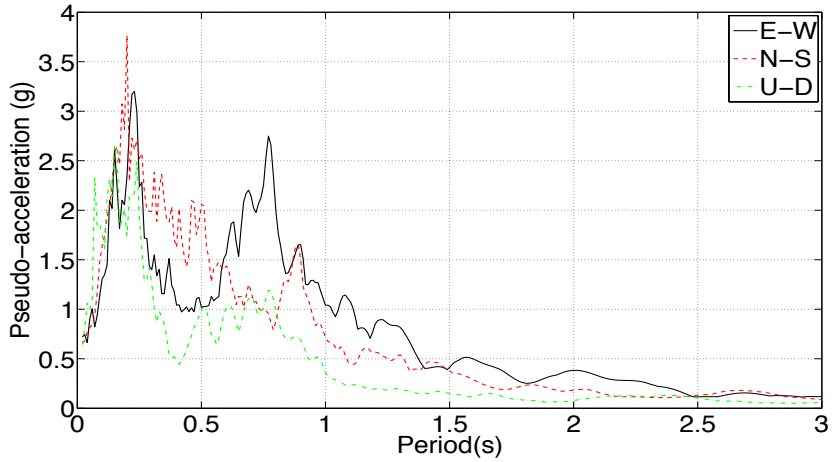

Figure 3.7 Pseudo acceleration spectrum San Pedro de la Paz.

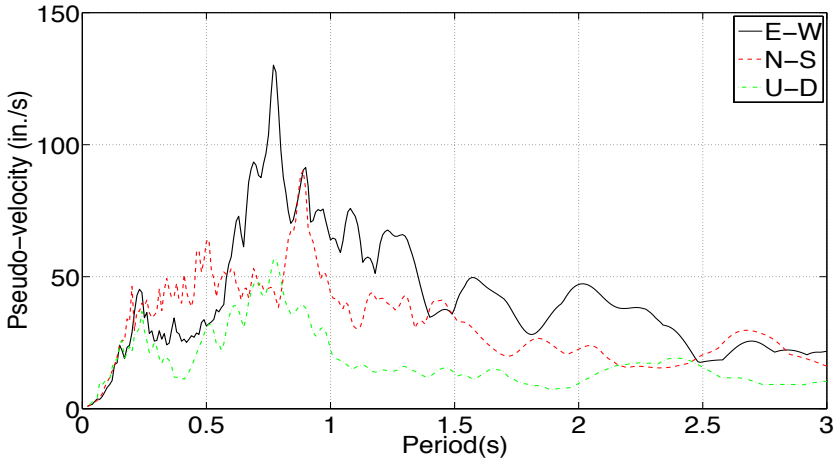

Figure 3.8 Pseudo velocity spectrum San Pedro de la Paz (1 in.=25.4 mm).

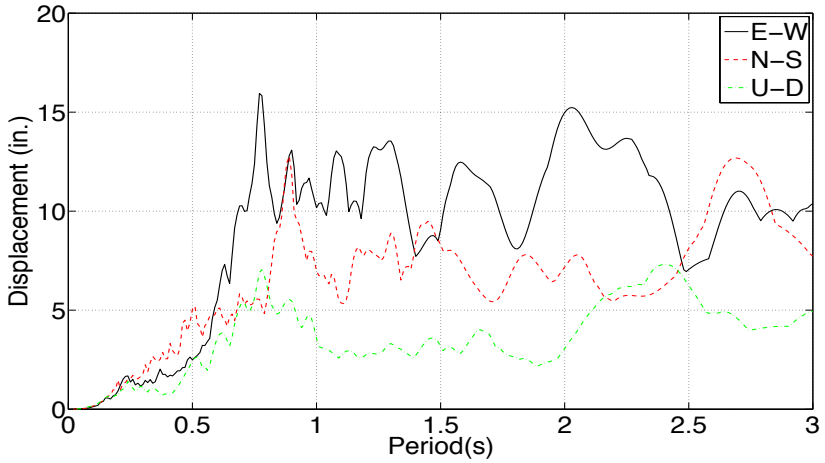

Figure 3.9 Displacement spectrum San Pedro de la Paz (1 in.=25.4 mm).

From an ETABS linear analysis model (see section 3.8), the first-mode period in the EW direction is $T = 0.57\ s$. This period is based in several assumptions regarding material properties and loads. In Figure 3.7 is observed that the calculated period falls in the valley of the EW pseudo-acceleration spectrum, and a large peak is observed at $T \sim 0.76\ s$. Therefore, a sensitivity analysis should be done regarding the first-mode period and its influence on the calculated structure response.

According to Figure 3.9, in the EW direction the peak spectral displacement is between 9.8-15.8 in. (250-400 mm) for the reasonable building period range. Therefore, the maximum average drift ratio is:

$$DR_{max} = 1.28\frac{D}{\Delta h} = 1.28\frac{15.8}{1412.2} = 1.43\% \tag{3.4}$$

Figure 3.10 shows a comparison between the computed PSA spectrum (2% damping ratio) and the NCh 433 Of. 1996 elastic spectrum (R^*=1).

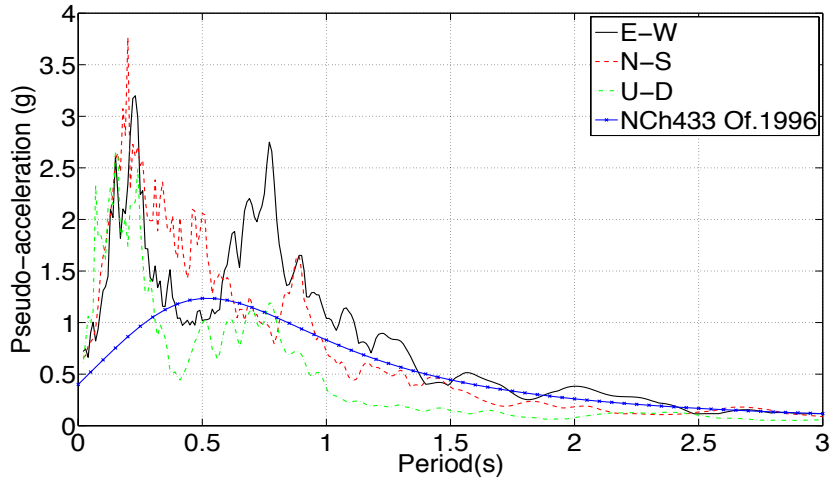

Figure 3.10 Pseudo acceleration spectrum comparison.

Figure 3.11 shows a tripartite plot for E-W, N-S and U-D motion.

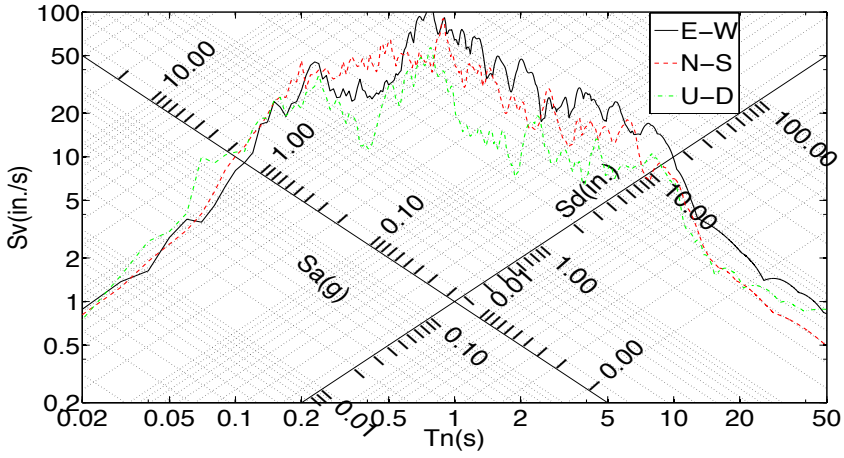

Figure 3.11 Tripartite plot for E-W, N-S and U-D motion (1 in.=25.4 mm).

From Figure 3.11 it is clear that for the period range $0.57\ s \leq T \leq 0.76\ s$ the structure is in the displacement preserved zone ($R = \mu\ and\ \gamma = 1$), therefore:

$$DR_{max}^{non\ linear} \approx DR_{max}^{elastic} \tag{3.5}$$

3.5 MATERIAL PROPERTIES

According to the building design documents, the material nominal properties are:

- Concrete H30 NC 90%: maximum compressive strength in cubic test specimen 4,350 psi (30 MPa)
- Reinforcement steel A63-42H: tensile strength f_u= 91 ksi (630 MPa), yield strength f_y= 60 ksi (420 MPa)

Table 3.1 shows the relationship between f'_c and the maximum cubic compressive stress.

Table 3.1 NCh 430 Of. 2008 conversion table.

f'_c, psi (Mpa)	Concrete grade (NCh170 confidence level 90%)
2,320 (16)	H20
2,900 (20)	H25
3,630 (25)	H30
4,350 (30)	H35
5,080 (35)	H40
5,800 (40)	H45

Therefore, for this case f'_c= 3,630 psi (25 MPa).

Several tests were done to determine real concrete properties, which are used later for analysis, according to the Chilean standards NCh 1171/1 Of.2001 and NCh 1171/2 Of.2001. Table 3.2 quantifies those tests.

Table 3.2 Alto Huerto building tests (DICTUC report #906575/10-056-EN-01-R0, 2010).

Test	Quantity
Compressive strength	12
Tensile strength	-
Thickness determination	12
Density determination	12
Detailed visual inspection	12

Table 3.3 shows the location where each core was obtained.

Table 3.3 Cores location (DICTUC report #906575/10-056-EN-01-R0, 2010).

Core	Position
TH01	Wall level -2, axis K between 3-5, 4.43 ft (1.35 m) from 3 and 3.61 ft (1.10 m) from floor level.
TH02	Wall level -1, axis 5 between C-G, 4.87 ft (1.48 m) from C and 2.20 ft (0.67 m) from floor level.
TH03	Wall level -1, axis L between 11-14, 3.94 ft (1.20 m) from 14 and 1.97 ft (0.60 m) from floor level.
TH04	Wall level 1, axis U between 5-9, 4.27 ft (1.30 m) from 9 and 3.12 ft (0.95 m) from floor level.
TH05	Wall level 1, axis 11 between G-U, 21.65 ft (6.60 m) from U and 3.84 ft (1.17 m) from floor level.
TH06	Column level 1, axis F between 12-14, 3.77 ft (1.15 m) from 14 and 4.27 ft (1.30 m) from floor level.
TH07	Wall level 2, axis 12 between ZZ-U, 12.14 ft (3.70 m) from ZZ and 3.44 ft (1.05 m) from floor level.
TH08’	Slab level 1, axis U-V between 8-9, 0.98 ft (0.30 m) from U and 2.62 ft (0.80 m) from 9.
TH09	Wall level 4, axis Q between 5-1, 9.84 ft (3.00 m) from 1 and 3.94 ft (1.20 m) from floor level.
TH10	Wall level 6, axis 5 between A-G, 10.33 ft (3.15 m) from A and 3.02 ft (0.92 m) from floor level.
TH11’	Slab level 9, axes E-G between 9-12, 9.02 ft (2.75 m) from G and 4.53 ft (1.38 m) from 12.
TH12’	Wall level 13, axis 5 between U-ZZ, 11.32 ft (3.45 m) from ZZ and 4.43 ft (1.35 m) from floor level.

Table 3.4 shows the results of the compressive strength tests.

Table 3.4 Cores strength (DICTUC report #906575/10-056-EN-01-R0, 2010).

Core	Maximum Load, lb (kN)	Core compressive strength, psi (MPa)	Cylindrical compressive strength, psi (MPa)	Cubic compressive strength, psi (MPa)
TH01	116,451 (518)	9,384 (64.7)	9,384 (64.7)	10,109 (69.7)
TH02	100,265 (446)	8,079 (55.7)	8,079 (55.7)	8,804 (60.7)
TH03	99,141 (441)	7,977 (55.0)	7,977 (55.0)	8,702 (60.0)
TH04	97,117 (432)	7,818 (53.9)	7,818 (53.9)	8,543 (58.9)
TH05	108,133 (481)	8,702 (60.0)	8,702 (60.0)	9,427 (65.0)
TH06	90,598 (403)	7,295 (50.3)	7,295 (50.3)	8,021 (55.3)
TH07	115,552 (514)	9,311 (64.2)	9,311 (64.2)	10,037 (69.2)
TH08	76,435 (340)	6,150 (42.4)	5,598 (38.6)	6,324 (43.6)
TH09	109,482 (487)	8,818 (60.8)	8,818 (60.8)	9,543 (65.8)
TH10	71,040 (316)	5,714 (39.4)	5,598 (38.6)	6,324 (43.6)
TH11	70,365 (313)	5,671 (39.1)	5,047 (34.8)	5,773 (39.8)
TH12	67,443 (300)	5,424 (37.4)	5,279 (36.4)	6,005 (41.4)

In Table 3.4, cylindrical compressive strengths are obtained from core compressive strengths after applying the modification factors indicated in the Chilean standard NCh 1171/1 Of.2001.

After February 2010 Chile earthquake, one wall apparently buckled at the first story in Alto Huerto building (Figure 1.1). As response at the first story was the primary interest, linear and nonlinear models were assembled based on the compressive strength obtained from a first story core. Periods would not be much affected by using an alternative value for compressive strength. Therefore, the cubic compressive strength is taken as 8,000 psi (55 MPa), cylinder strength as f'_c= 7,300 psi (50 MPa), and the Young's modulus is E_c=4,800 ksi.

For linear analysis, the effective flexural and axial rigidity (including cracking) is used, according to ASCE 41 (2006), section 6.3.1.2.

- Walls-cracked: 0.5 $E_c I_g$ (flexural), 0.4 $E_c A_w$ (shear)
- Columns: 0.3 $E_c I_g$ (flexural), 0.4 $E_c A_w$ (shear)
- Slabs: 1/3 $E_c I_g$ (flexural)

Kent and Park (1971) unconfined concrete model is used for nonlinear analysis. Measured reinforcement properties from coupons from the building are tensile strength f_u= 110 ksi (759 MPa) and yield strength f_y= 73.4 ksi (506 MPa).

3.6 SOIL CONDITIONS

The soil layers (EMPRO report # 71071-07, 2007) are indicated below:

- H-1 From 0.0 ft to 18.0 ft (0.00m-5.50m)
- H-2 From 18.0 ft to 34.4 ft (5.50m-10.50m)
- H-3 From 34.4 ft to 38.1 ft (10.50m-11.60m)
- H-4 From 38.1 ft to 50.7 ft (11.60m-15.45m)
- H-5 From 50.7 ft to 52.2 ft (15.45m-15.90m)
- H-6 From 52.2 ft to 65.8 ft (15.90m-20.06m)

Table 3.5 indicates the soil parameters for each layer.

Table 3.5 Soil properties.

	H-1	H-2	H-3	H-4	H-5	H-6
USCS classification	SP,SM	SP	ML	SP	ML	SP
Fines (%)	<12%	3	84	1	57	3
Plasticity index	NP	NP	NP	NP	NP	NP
Solids specific weight (Gs)	2.7	2.77	2.53	2.7	2.61	2.76
Nspt, blows/ft	>40	29 to 73	9	57 to 62	13	>60
Internal friction angle	38	38	-	40	-	42
Effective cohesion, psi (MPa)	0	0	-	0	0	0

According to the Chilean standard NCh 433 Of. 1996, the soil classifies as type III for seismic zone 3.

3.7 MAIN DAMAGE DESCRIPTION

The main post-earthquake damage of the building (DICTUC report #906575/10-056-EE-01-R0, 2010) is described in this section. Even though no major exterior damage is apparent, the floors cantilevering from the walls to form balconies showed obvious sagging.

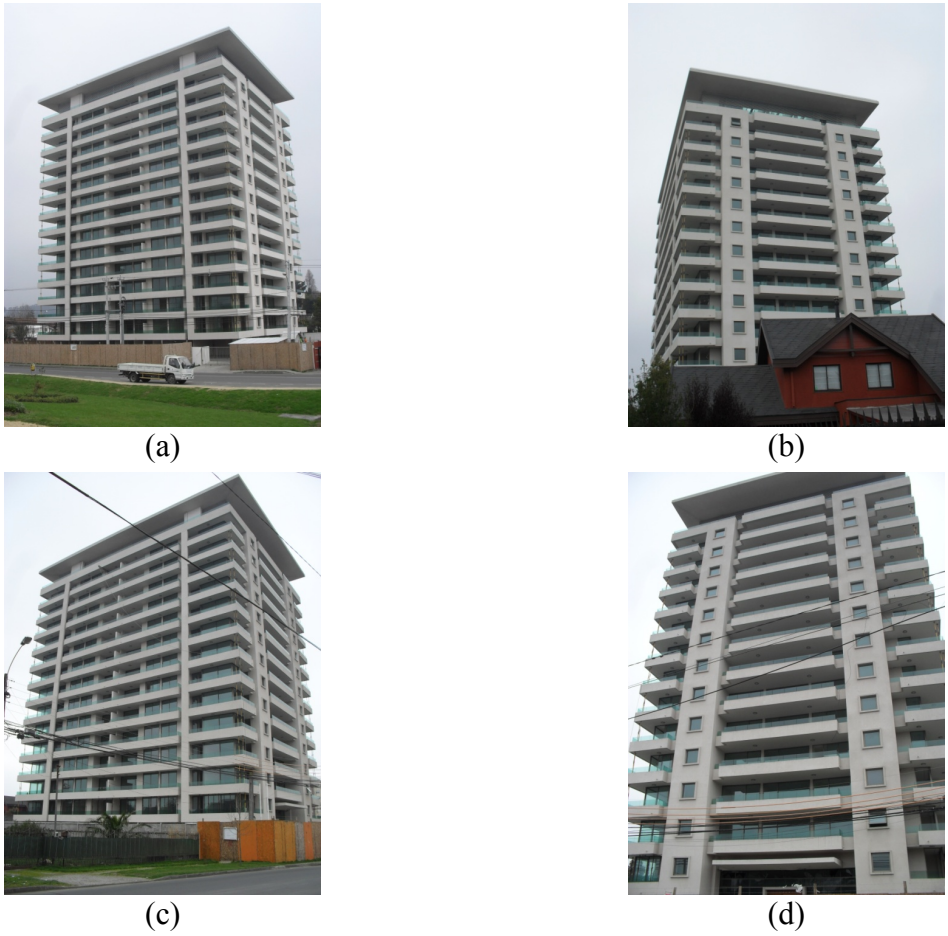

(a) (b)

(c) (d)

Figure 3.12 Exterior views: (a) east view; (b) axis A; (c) west view; (d) axis Zz.

Severe damage, which affects the structure stability, was observed from the second subterranean level to the first story, in walls oriented east-west between axes 12 and 14. In general terms, this entire line of walls failed in one of those stories. Repetitive damages are observed from the second to the fourteenth story, without affecting the structure stability. Finally, in the fifteenth story and in the mechanical room, damage increases due to the changes on the lateral force-resisting system.

The main damage in the second subterranean level is concentrated in two walls. Supplementary reinforcement cages have been added adjacent to the original wall sections.

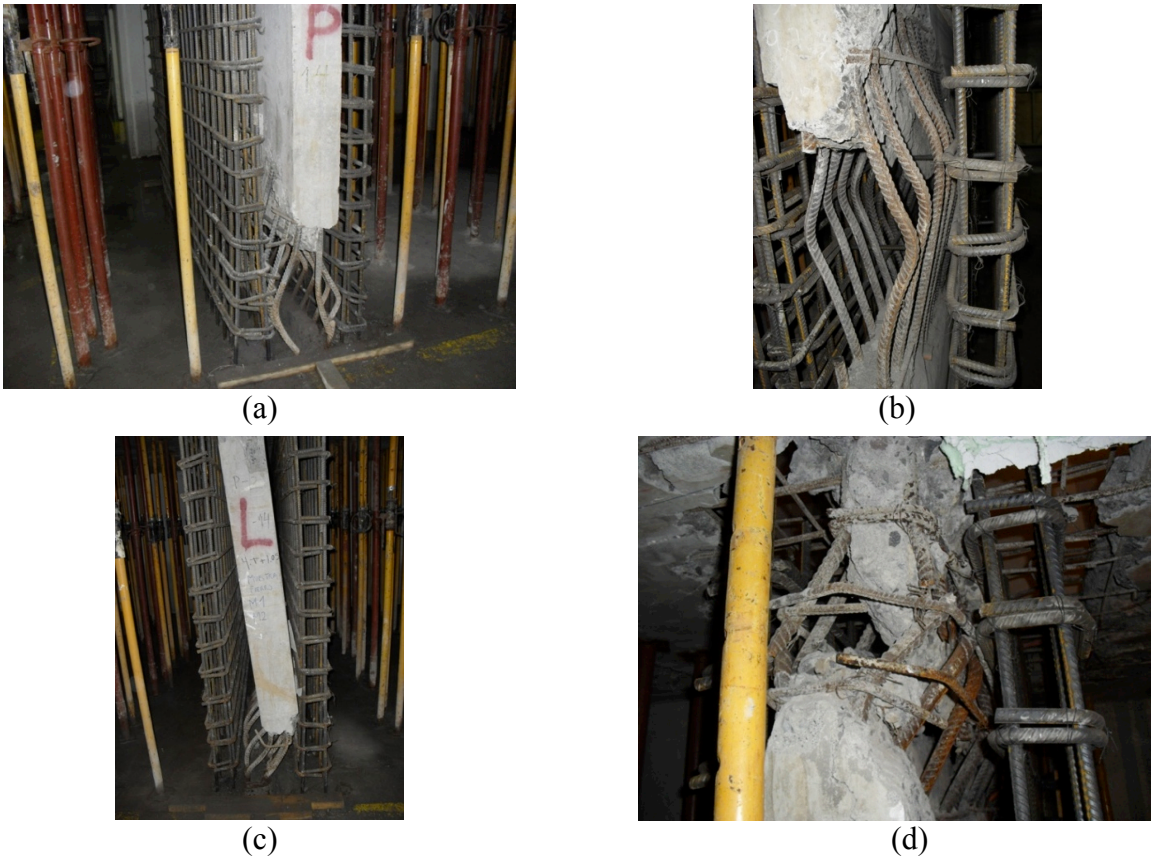

(a) (b)

(c) (d)

Figure 3.13 Damage in second subterranean level: (a) axis P, between axes 12 and 14; (b) detail of axis P; (c) axis L, between axes 11 and 14; (d) axis G, between axes 7 and 10.

Similar damage is observed in the first subterranean level. There are two failures in walls located in axis V and F, between 14 and 12.

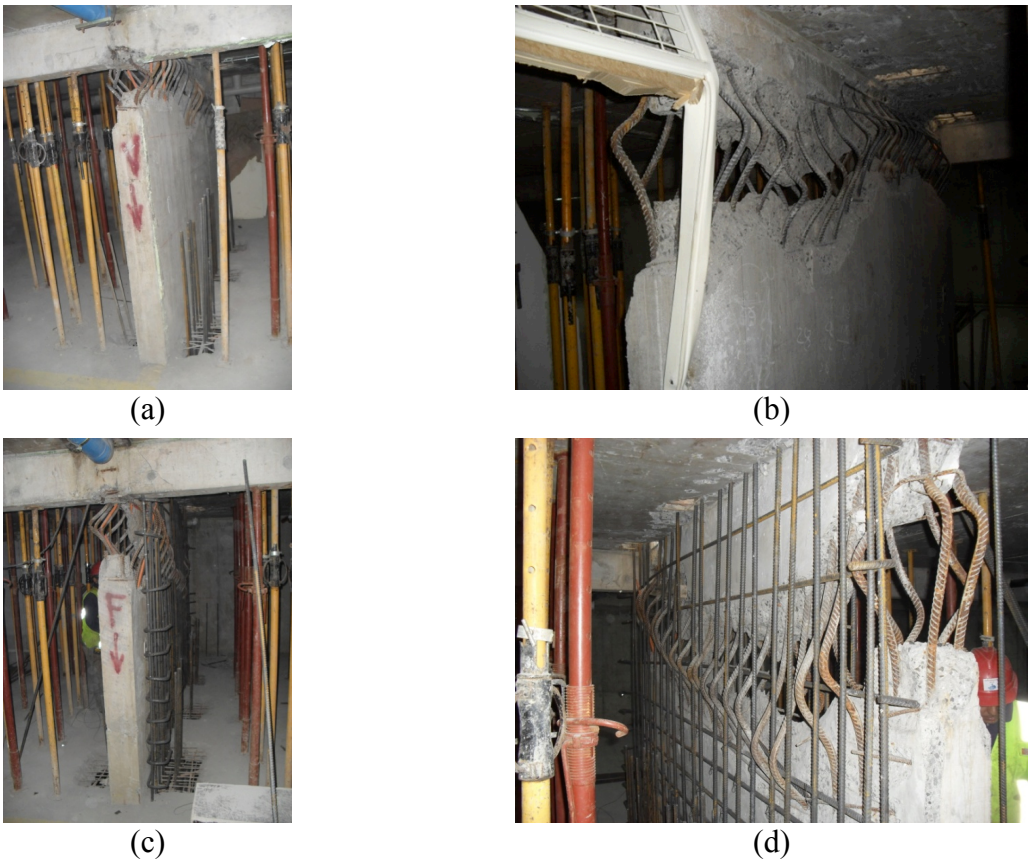

(a) (b)

(c) (d)

Figure 3.14 Damage in first subterranean level: (a) axis V, between axes 12 and 14; (b) detail of axis V; (c) axis F, between axes 12 and 14; (d) detail of axis F.

In the first story, two specific failures types were observed. The wall in axis Ñ, between axes 3 and 4, has apparent compression failure. Note that axis Ñ wall has an irregularity (indicated in Figure 3.21) in this story that could have been a contributing factor. The axis J wall, between axes 6 and 9, also had a compression failure.

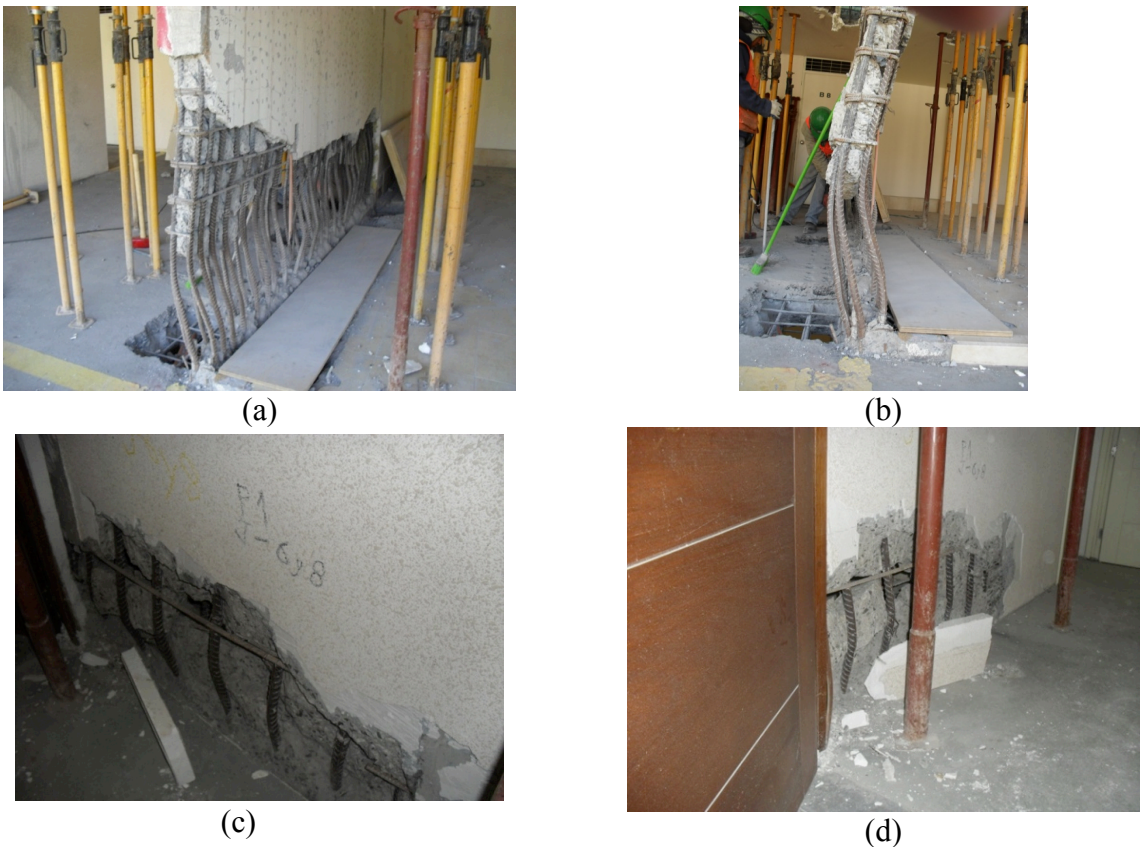

Figure 3.15 First story damage: (a) axis Ñ, between axes 3 and 5; (b) detail of axis Ñ; (c) axis J, between axes 6 and 8; (d) detail of axis J.

Another important damage is located in axis U, between axes 5 and 9. This wall has a compression failure. This failure is consistent with the predominant east-west direction of the earthquake shaking previously mentioned. It should be noticed that this is an L-shaped wall (flange in axis 5), so the flange may have had an influence in the failure mode.

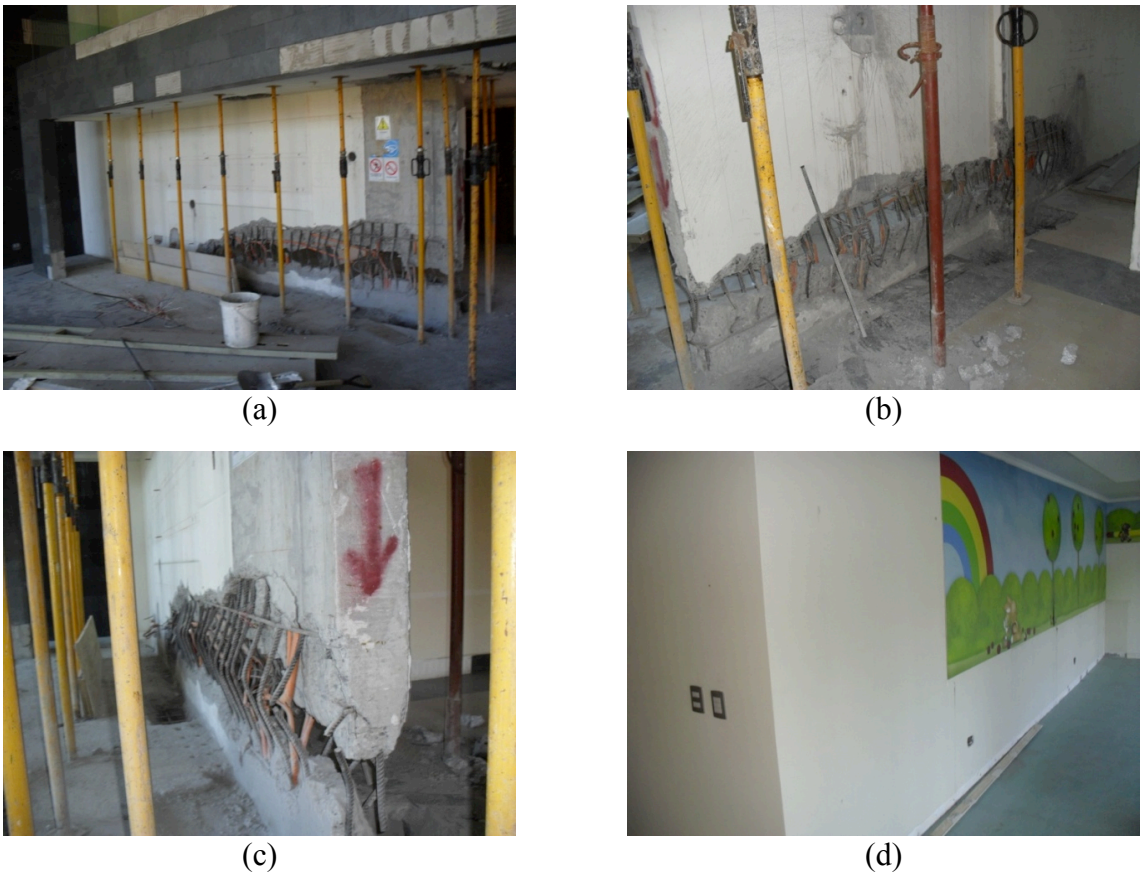

(a) (b)

(c) (d)

Figure 3.16 First story damage: (a) axis U, between axes 5 and 9; (b) detail of axis U; (c) axis U, between axes 5 and 9; (d) axis 5, between axes U and Y (view of the perpendicular wall).

At the four corners of the building, in the first story, there are walls of non-uniform thickness (200/300 mm). Failures can be observed in the section of thickness change.

Figure 3.17 First story damage: (a) axis C, between axes 13 and 14; (b) axis C, between axes 13 and 14; (c) axis C, slab damage; (d) axis C, between axes 3 and 4; (e) axis Y, between axes 3 and 4; (f) axis Y, between axes 13 and 14.

Connections between walls and slabs sustained damage as shown next.

(a) (b)

Figure 3.18 Second story damage in axis C, between 13 and 14: (a) view 1; (b) view 2.

The following table lists damage to various walls in the building, using terminology borrowed from DICTUC report #906575/10-056-EE-01-R0 (2010).

Table 3.6 Walls state in Alto Huerto building (1 in. = 25.4 mm).

Story	l_w (in.)	b (in.)	h_u (in.)	h_u/b	N/S Line	E-W Line	Damage level	Failure type
-2	133.5	7.9	102.4	13.0	12-14	F	Low	Compression
-2	63.8	7.9	102.4	13.0	8-9	G	Total	Compression
-2	233.5	7.9	102.4	13.0	11-14	L	Total	Compression / Shear
-2	133.5	7.9	102.4	13.0	12-14	P	Total	Compression
-1	133.5	7.9	102.4	13.0	12-14	F	Total	Compression
-1	133.5	7.9	102.4	13.0	12-14	P	Low	Compression
-1	133.5	7.9	102.4	13.0	12-14	V	Total	Compression
1	82.7	11.8	100.4	8.5	13-14	C	Total	Shear
1	82.7	11.8	100.4	8.5	3-4	C	Low	Shear
1	133.5	7.9	100.4	12.8	3-4	F	Total	Compression
1	133.5	7.9	100.4	12.8	13-14	F	Low	Tension
1	55.1	7.9	100.4	12.8	7-8	J	Total	Compression
1	133.5	7.9	100.4	12.8	3-4	K	Low	Compression
1	233.5	7.9	100.4	12.8	13-14	L	Severe	Tension
1	133.5	7.9	100.4	12.8	3-4	Ñ	Total	Compression
1	244.9	7.9	100.4	12.8	11	N	Severe	Shear
1	133.5	7.9	100.4	12.8	3-4	Q	Low	Tension
1	233.5	7.9	100.4	12.8	13-14	P	Severe	Tension
1	39.4	7.9	100.4	12.8	5	Q	Severe	Compression
1	265.0	7.9	100.4	12.8	6-9	U	Total	Compression
1	133.5	7.9	100.4	12.8	13-14	V	Low	Tension
1	94.5	11.8	100.4	8.5	3-4	Y	Low	Shear
1	94.5	7.9	100.4	12.8	13	Y	Total	Shear

Story	l_w (in.)	b (in.)	h_u (in.)	h_u/b	N/S Line	E-W Line	Damage level	Failure type
2	208.7	5.9	100.4	17.0	8-9	G	Total	Shear
2	244.5	7.9	100.4	12.8	12	W-X	Total	Shear
14	123.2	7.9	107.1	13.6	11	P-S	Severe	Shear
15	46.9	7.9	100.4	12.8	5-6	G	Low	Shear
15	83.9	7.9	100.4	12.8	8	G	Severe	Shear / Compression
15	44.9	7.9	100.4	12.8	9-11	G	Total	Shear / Compression
15	126.0	7.9	100.4	12.8	6-8	K	Low	Shear
15	24.8	7.9	100.4	12.8	8-9	K	Total	Shear / Compression
15	47.2	7.9	100.4	12.8	8	K-H	Severe	Shear / Compression
15	90.6	7.9	100.4	12.8	9	K-M	Severe	Shear
15	338.6	7.9	100.4	12.8	11	L-Ñ	Low	Shear / Tension
15	96.1	7.9	100.4	12.8	6	Q-U	Low	Shear / Tension / Compression
15	66.5	7.9	100.4	12.8	8	Q-U	Low	Tension
15	216.5	7.9	100.4	12.8	8-9	U	Low	Shear
15	216.5	7.9	100.4	12.8	9	U	Total	Shear / Punching shear in slab
16	88.2	7.9	100.4	12.8	9-11	J	Total	Shear
16	186.6	7.9	100.4	12.8	8-11	U	Total	Shear

3.8 BUILDING LINEAR MODEL

Figure 3.19 shows the ETABS linear fixed-base model.

Figure 3.19 ETABS model for Alto Huerto building.

3.8.1 Loads

Table 3.7 shows the calculated gravity loads.

Table 3.7 Gravity loads per floor for Alto Huerto building.

Floor	Slab thickness, in. (mm)	Dead Load, psf (kPa)	Live Load, psf (kPa)
-2	7.87 (200)	112.99 (5.41)	10.03 (0.48)
-1	7.87 (200)	112.99 (5.41)	10.03 (0.48)
1	5.91 (150)	87.09 (4.17)	10.03 (0.48)
2 to 14	5.91 (150)	87.09 (4.17)	10.03 (0.48)
Roof	5.91 (150)	87.09 (4.17)	10.03 (0.48)

For the purpose of defining seismic mass 50% of live load is considered.

3.8.2 Seismic Analysis

Table 3.8 shows the building modes periods and modal participating mass ratios.

Table 3.8 Modal analysis output for Alto Huerto building.

Mode	Period (s)	Modal mass ratio X direction	Modal mass ratio Y direction
1	0.78	0.18	0.00
2	0.57	60.19	0.02
3	0.47	0.02	60.16
4	0.19	0.00	0.18
5	0.18	0.05	0.01
6	0.15	0.14	0.05
7	0.14	11.92	0.07
8	0.13	2.26	0.42
9	0.12	0.60	1.43
10	0.11	0.20	10.04

Therefore, the 2nd mode has the greatest effective modal mass in x direction (T=0.57 s), and the 3rd mode has the greatest effective modal mass in y direction (T=0.47 s).

As noted in section 3.4, according to the elastic response spectrum of the nearby recorded ground motion, lateral displacement is sensitive to the vibration period, with peak displacement occurring for fundamental period $T = 0.76\ s$. To achieve this increased period, the seismic mass was artificially increased. Modifying the stiffness properties could have done this as an alternative approach. For this model, the building modal analysis output is modified as shown in Table 3.9.

Table 3.9 Modal analysis output for fundamental period EW direction T=0.76 s.

Mode	Period (s)	Effective modal mass X direction	Effective modal mass Y direction	Effective modal mass Z direction
1	1.05	0.18	0.00	0.00
2	0.76	60.19	0.02	0.00
3	0.63	0.02	60.16	0.00
4	0.26	0.00	0.19	4.27
5	0.18	14.02	0.00	0.49
6	0.17	0.12	1.02	29.95
7	0.16	0.00	11.24	3.97
8	0.10	0.02	0.88	44.57
9	0.09	13.43	1.55	0.06
10	0.08	1.59	13.13	1.81

In section 3.9, a non-linear fixed-base model is developed for the wall with the most obvious buckling. This wall is oriented in the EW direction. For that analysis, it will be necessary to have an estimate of the maximum displacement that the building experienced during the earthquake.

Figure 3.20 shows the maximum floor displacements in the east-west direction for the model with the modified seismic mass (Table 3.9).

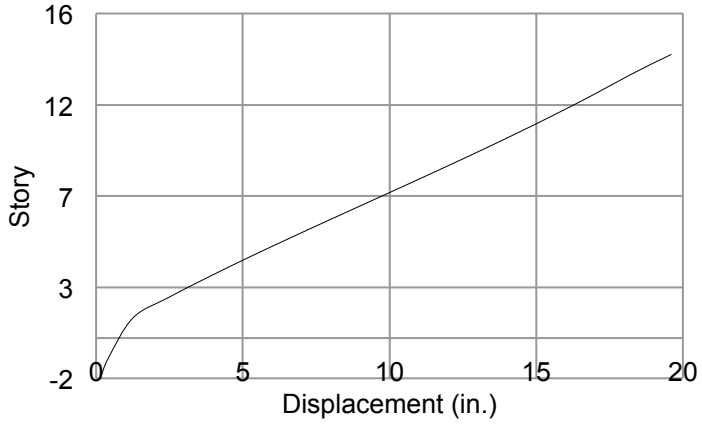

Figure 3.20 Maximum floor displacements, east-west direction (1 in. = 25.4 mm).

From Figure 3.20 the average drift is 19.60/1412.2=1.4% as expected from Equation (3.4).

3.9 WALL Ñ ANALYSIS

Several analyses were performed for the wall with the most obvious buckling as pictured in Figure 1.1. Figure 3.21 shows an elevation view of wall Ñ.

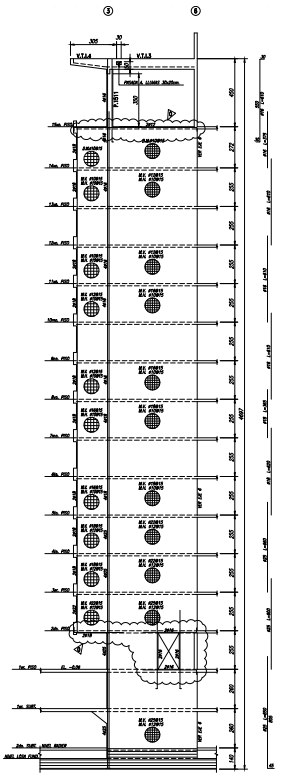

Figure 3.21 Elevation view of wall Ñ.

3.9.1 Loads

Figure 3.22 shows the tributary area on the typical floor.

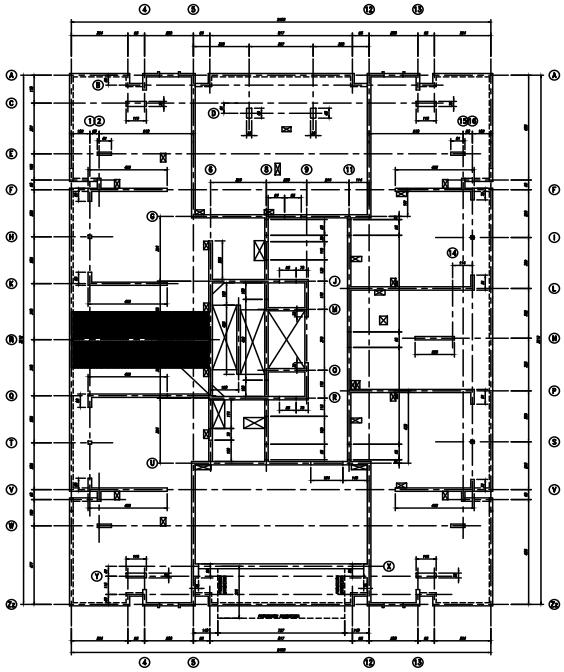

Figure 3.22 Tributary area at level 2-14 (typical floor).

Table 3.10 indicates loads per floor.

Table 3.10 Gravity load per floor wall Ñ.

Floor	Area, ft^2 (m^2)	Dead Load, kips (kN)	Live Load, kips (kN)
-2	400.80 (37.24)	45.15 (200.84)	4.10 (18.24)
-1	400.80 (37.24)	45.15 (200.84)	4.10 (18.24)
1	248.10 (23.05)	21.60 (96.08)	2.54 (11.30)
2 to 14	284.70 (26.45)	24.78 (110.23)	2.92 (12.98)
Roof	339.60 (31.55)	29.56 (131.49)	3.48 (15.48)

The wall self-weight is automatically calculated by PERFORM 3D. The axial load at the first story bottom level is P= 863 kips (3839 kN). Therefore $P/A_g f'_c$=0.05.

3.9.2 PERFORM 3D Nonlinear Approach

A non-linear, fixed-base model was developed using PERFORM 3D. Two different approaches are followed for analysis:

- Non-linear response history analysis. The seismic mass is calculated by tributary areas considering 50% of the live load. A multiplier factor is applied over the seismic load in order to get the same lateral displacement given in Equation (3.4). The ground motion is defined in section 3.4.
- Pushover analysis. A lateral force pattern proportional to the height over the ground level is applied. A pushover analysis is performed until reaching an average drift ratio of 1.43%.

From these two analyses it is possible to estimate the boundary bars strain.

Figure 3.23 shows the base-overturning moment versus the average drift ratio for the nonlinear response history analysis.

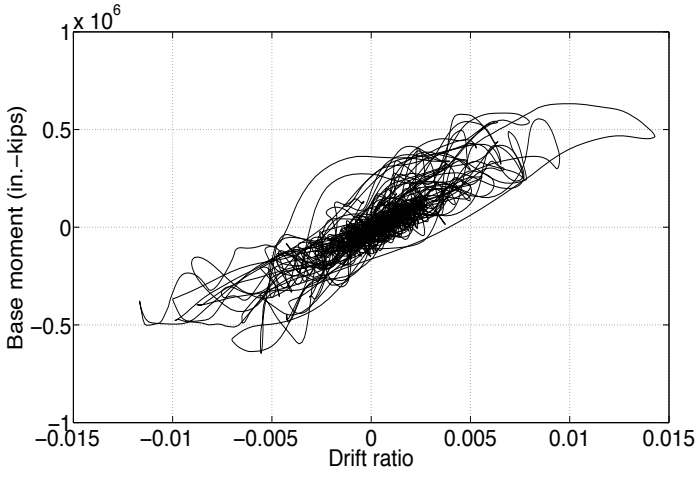

Figure 3.23 Nonlinear response history analysis – base overturning moment v/s average drift ratio (1 in-kips = 0.11 kN-m).

Figure 3.24 and Figure 3.25 show calculated section strain profiles from nonlinear response history and pushover analyses.

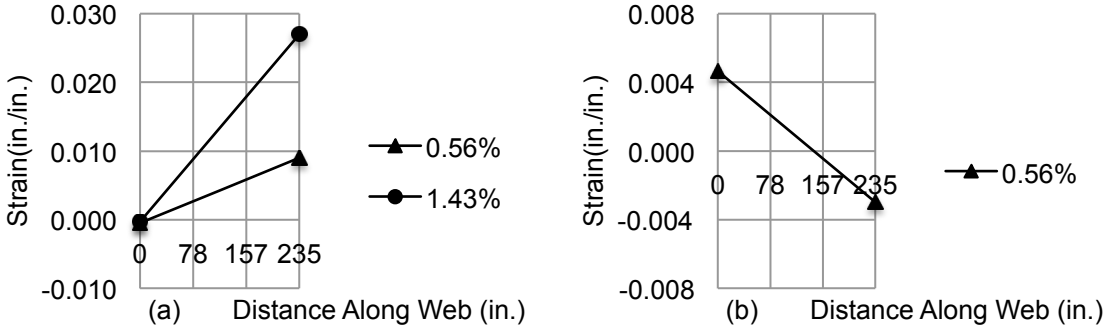

Figure 3.24 Strain profiles for wall Ñ from nonlinear response history analysis: (a) flange in compression; (b) flange in tension.

Figure 3.25 shows calculated section strain profiles from pushover analysis.

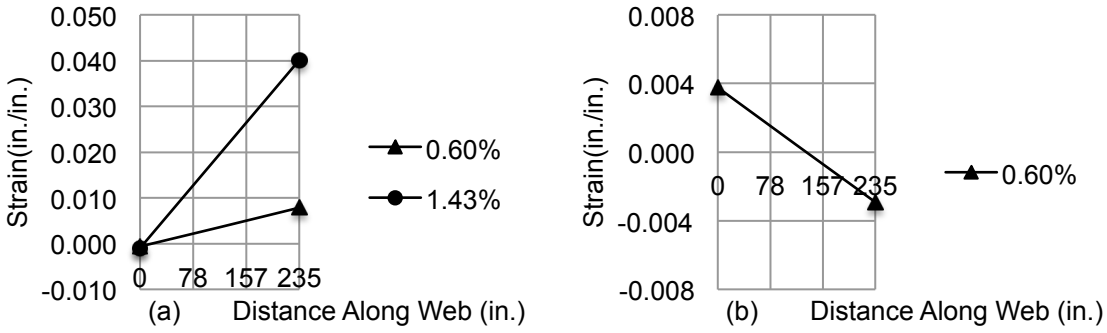

Figure 3.25 Strain profiles for wall Ñ from pushover analysis: (a) flange in compression; (b) flange in tension.

Both figures show the strain profile at $DR = 1.43\%$ (maximum elastic drift ratio), when the flange is in compression. For this case, the maximum stem tensile strain is close to $\epsilon_{sm} = 0.030$ for the dynamic analysis and $\epsilon_{sm} = 0.040$ for the pushover analysis. But the stem compressive failure occurs at a lower drift, when DR is between 0.56% and 0.60%. At this drift ratio, when the flange is in compression (Figure 3.24a), the stem tensile strain for both analyses is close to $\epsilon_{sm} = 0.010$.

3.9.3 Curvature Integration Approach

The procedure indicated in section 2.3.1 is followed. The simplified model has concentrated nonlinearity in the first story, and linear elastic behavior is assumed in the other stories. This is reasonable considering the wall has a relatively weak first story due to a setback.

For the first story, the moment curvature relation is calculated with XTRACT. For the upper stories, the cracked properties indicated in ASCE 41 (2006) are used.

Figure 3.26 shows the section properties used in the XTRACT model.

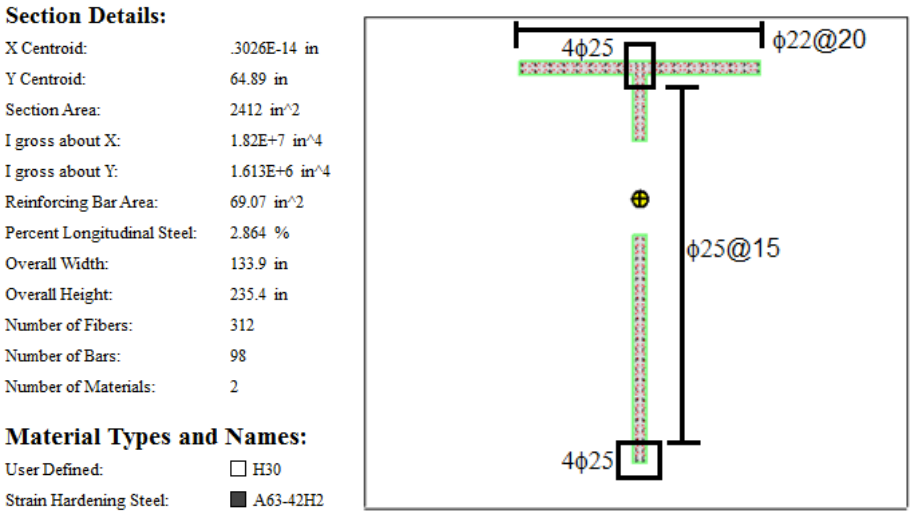

Figure 3.26 XTRACT model section properties for wall Ñ (1 in. = 25.4 mm, bars diameter in mm).

Figure 3.27 shows the moment-curvature relations.

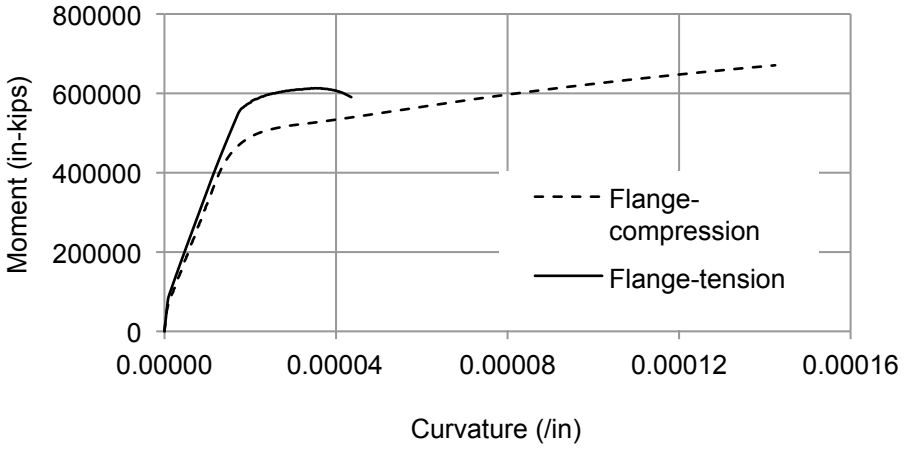

Figure 3.27 Moment-curvature relations axial load *N*=863 kips (1 in. = 25.4 mm; 1 in-kips = 0.11 kN-m).

The reference lateral force distribution used in this model is inverted triangular. The amplitude of this distribution was increased until achieving the target drift of 1.43%. For the case of flange in compression, the target displacement is reached without tensile failure in the steel reinforcement bars or compressive failure in concrete. Figure 3.28 shows the normalized moment and curvature over the height for this case ($DR = 1.43\%$).

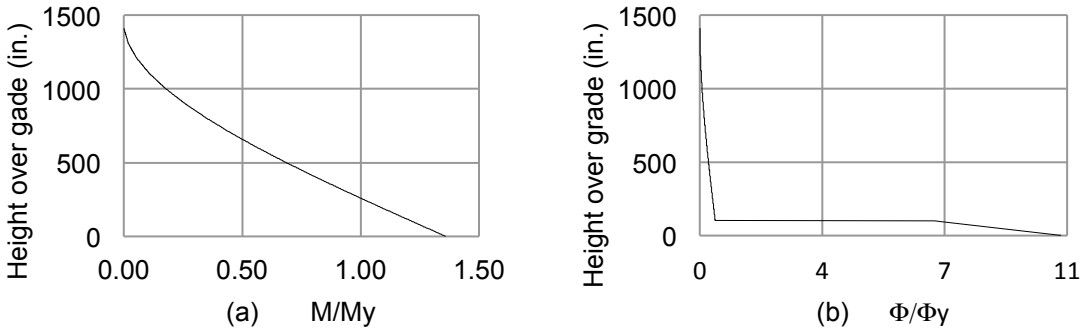

Figure 3.28 (a) Normalized moment; (b) curvature for flange in compression.

As expected, the curvature demand is concentrated in the first story. (Note that the calculated curvature distribution shows a sharp spike toward the base level, indicating that the calculated strain and curvature may be sensitive to minor variations in the deformation or moment demands. A plastic hinge model is used later in this chapter to reduce the sensitivity of the result. For the case of flange in tension, Figure 3.29 shows the normalized moment and curvature over the height ($DR = 0.49\%$), when the stem experienced compressive failure.

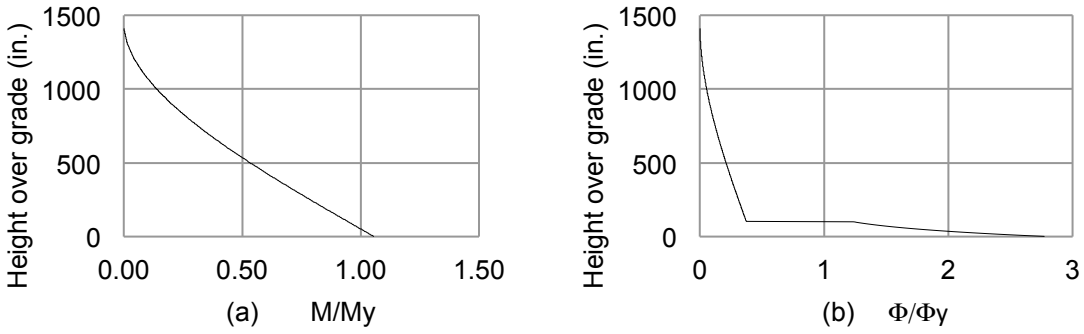

Figure 3.29 (a) Normalized moment; (b) curvature for flange in tension.

Figure 3.30 shows the calculated section strain profiles.

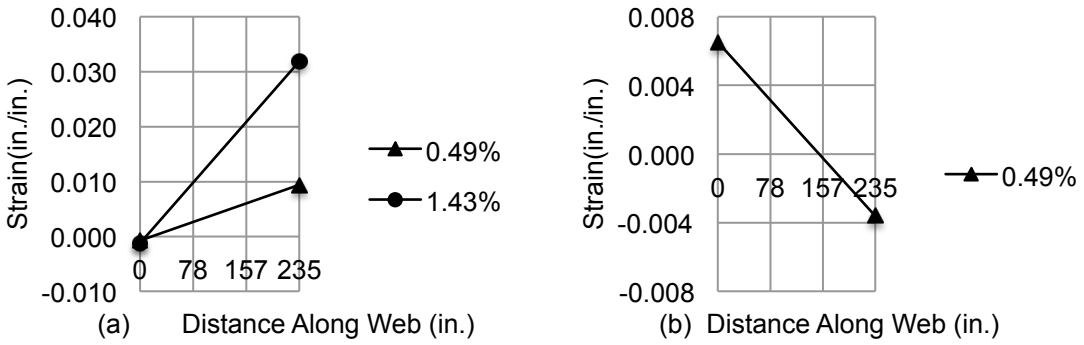

Figure 3.30 Strain profiles for wall Ñ from curvature integration: (a) flange in compression; (b) flange in tension.

For the case of flange in compression, the target drift ratio of 1.43% is reached without section failure, with a maximum tensile strain in the wall stem close to $\epsilon_{sm} = 0.030$.

For flange in tension, the ultimate state is triggered by compressive failure at the wall stem, when the maximum compressive strain reaches $\epsilon_c = 0.0036$. The average drift ratio at this point is 0.49%. At this drift ratio, when the flange is in compression, the tensile strain in the stem is close to $\epsilon_{sm} = 0.010$.

3.9.4 Simplified Plastic Hinge Approach

As was indicated in section 3.9.3, the wall has a relatively weak first story due to a setback. The nonlinear behavior will be concentrated here, and the contribution to the top displacement of the elastic deformation in the upper stories is expected to be small in comparison to the contribution given by the first story nonlinearity. A simplified plastic hinge approach according to Equation (2.20) is appropriate to model this behavior.

For the case of flange in compression, the curvature at 1.43% average drift ratio is given by $\emptyset_u = \frac{1.43\%}{0.5 \cdot 235} = 1.22 \cdot 10^{-4}$ in.$^{-1}$. For flange in tension, the ultimate state is triggered by compressive failure at the wall stem, at a curvature $\emptyset_u = 4.36 \cdot 10^{-5}$ in.$^{-1}$. Therefore, the drift ratio is DR $= \emptyset_u \, l_p = 4.36 \cdot 10^{-5} \cdot 0.5 \cdot 235 = 0.51\%$. Figure 3.31 shows the calculated section strain profiles.

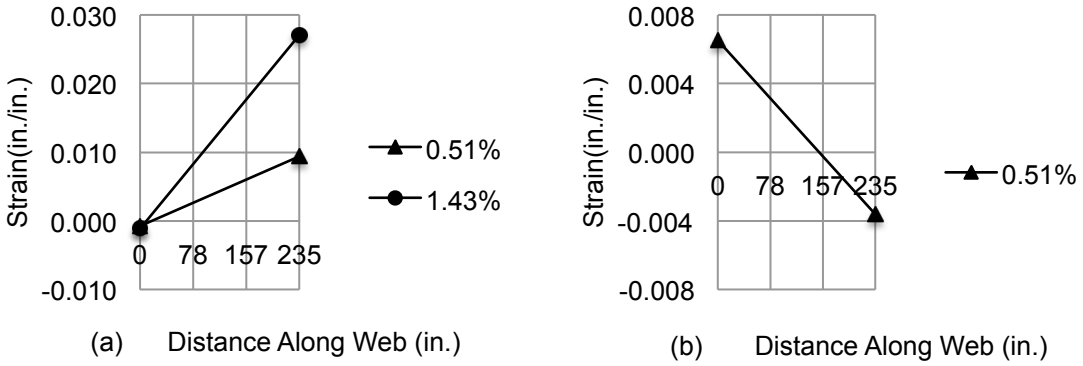

Figure 3.31 Strain profiles for wall Ñ from simplified plastic hinge approach: (a) flange in compression; (b) flange in tension.

The strain profiles obtained from both approaches (curvature integration and plastic hinge) are very similar. There is only a slight difference in the drift ratio value at which the compressive failure is triggered in the wall stem (0.49% for curvature integration and 0.51% for plastic hinge approach).

3.9.5 Buckling Analysis

The wall out-of-plane buckling is triggered when the maximum boundary bars tensile exceeds the value given by Equation (2.21). Considering b_{cr}=7.87 in. (200 mm), k=0.5, h_u= 100.39 in. (2.55 m), $\kappa = 0.8$, vertical reinforcement $\emptyset 25mm@15cm$, $f'_c = 7.3\ ksi$ (50 MPa) and $f_y = 73.4\ ksi$ (506 MPa), we obtain ϵ_{sm}= 0.035.

From different analyses different values of ϵ_{sm} were obtained, according to Table 3.11.

Table 3.11 Boundary bar tensile strain for different analyses.

Analysis	ε_{sm}
PERFORM 3D nonlinear response history analysis	0.03
PERFORM 3D pushover analysis DR=1.43%	0.04
Numerical integration of curvatures DR=1.43%	0.03
Simplified plastic hinge DR=1.43%	0.03

All the calculated strain values are reasonably close to each other and to the limit value given by Equation (2.21). But the failure due to stem compression occurs at an average drift ratio between 0.5% and 0.6%. After the wall crushes, it is possible to use the buckling model to investigate the stability of the section with the cover spalled off. For this case, b_{cr}=4.0 in. (101 mm) and $\kappa = 1$. Therefore $\in_{sm} = 0.011$.

At this drift ratio the maximum tensile strain in the stem is $\in_{sm} = 0.010$, close to the required value to trigger the wall lateral buckling. Therefore, it is reasonable to explain the wall failure by crushing first and then lateral buckling consistent with the theory presented in section 2.2, at an average drift ratio between 0.5% and 0.6%.

3.10 WALL K ANALYSIS

Several analyses were performed for wall K, shown in Figure 3.32.

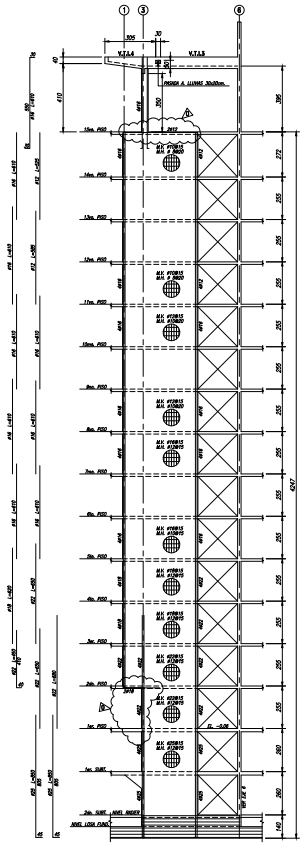

Figure 3.32 Elevation view of wall K.

3.10.1 Loads

Figure 3.33 shows the tributary area for gravity loads (typical floor).

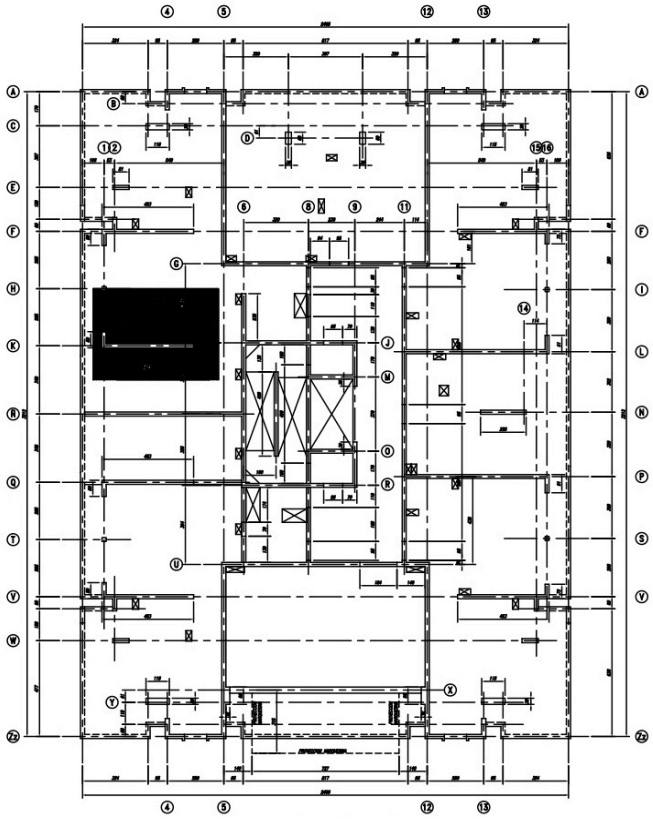

Figure 3.33 Tributary area at level 2-14 (typical floor).

Table 3.12 gives the gravity load per floor for wall K.

Table 3.12 Gravity load per floor wall K.

Floor	Area, ft^2 (m^2)	Dead Load, kips (kN)	Live Load, kips (kN)
-2	368.34 (34.22)	41.49 (184.56)	3.77 (16.77)
-1	368.34 (34.22)	41.49 (184.56)	3.77 (16.77)
1	275.98 (25.64)	24.02 (106.85)	2.83 (12.59)
2 to 14	303.90 (28.23)	26.45 (117.66)	3.11 (13.83)
Roof	249.29 (23.16)	21.70 (96.53)	2.55 (11.34)

The axial load at the first story bottom level is P=633 kips (2816 kN). Therefore, $P/A_g f'_c$=8.5%.

3.10.2 Curvature Integration Approach

This section follows the procedure developed in 3.9.3. Figure 3.34 shows the section properties used in the XTRACT model.

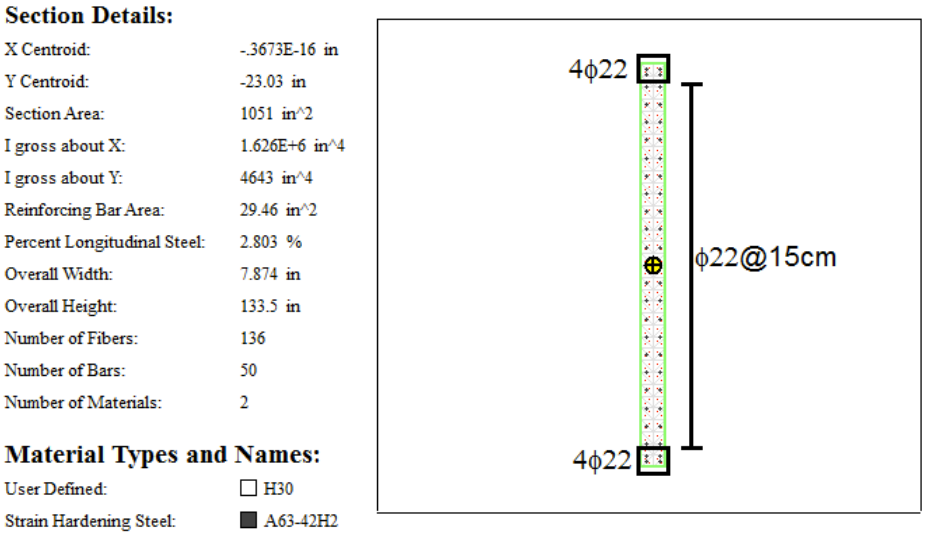

Figure 3.34 XTRACT model section properties for wall K (1 in. = 25.4 mm, bars diameter in mm).

Figure 3.35 shows the moment-curvature relation.

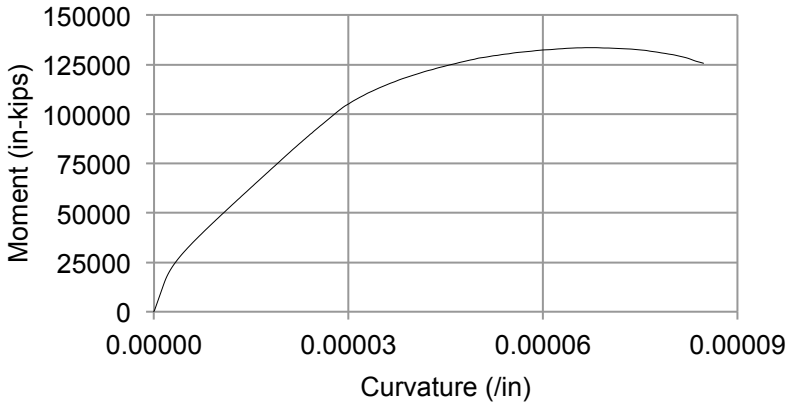

Figure 3.35 Moment-curvature relation axial load *N*=633 kips (1 in. = 25.4 mm; 1 in-kips = 0.11 kN-m).

As for wall Ñ, the reference lateral force distribution used in this model is inverted triangular and the amplitude of this distribution was increased until achieving the target displacement. Figure 3.36 shows the normalized moment and curvature over the height diagrams.

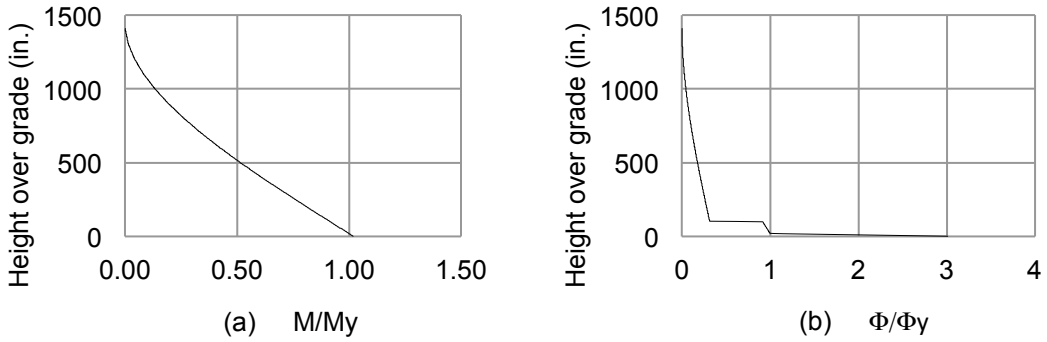

Figure 3.36 (a) Normalized moment; (b) curvature.

As expected, all the curvature demand is concentrated in the first story. Again as for wall Ñ, the calculated curvature distribution shows a sharp spike toward the base level, indicating that the calculated strain and curvature may be sensitive to minor variations in the deformation or moment demands. The plastic hinge model gets rid of this shortcoming.

Figure 3.37 shows the calculated section strain profile.

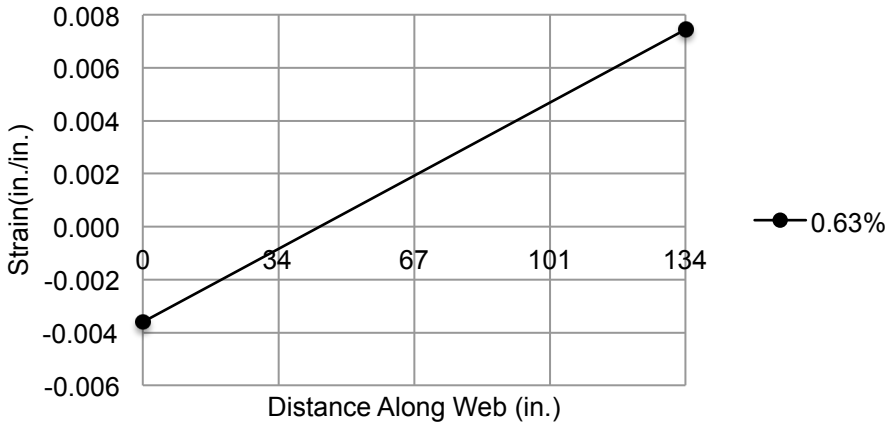

Figure 3.37 Strain profile for wall K from curvature integration.

As shown in Figure 3.37, for this case the ultimate state is triggered by compressive failure at the wall boundary, when the maximum compressive strain reaches $\epsilon_c = 0.0036$ at an average drift ratio of 0.63%.

3.10.3 Simplified Plastic Hinge Approach

A simplified plastic hinge approach according to Equation (2.20) is used as in wall Ñ. The ultimate state is triggered by compressive failure at the wall boundary, at a curvature $\emptyset_u = 4.36 \cdot 10^{-5}$ in.$^{-1}$. Therefore, the drift ratio is DR $= \emptyset_u \, l_p = 8.47 \cdot 10^{-5} \cdot 0.5 \cdot 134 = 0.57\%$.

Figure 3.38 shows the calculated section strain profiles.

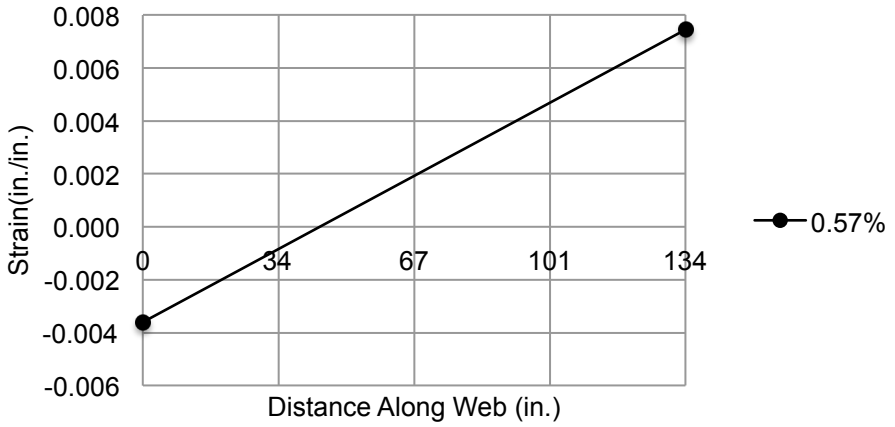

Figure 3.38 Strain profile for wall K from simplified plastic hinge approach.

The strain profiles obtained from both approaches (curvature integration and plastic hinge) are exactly the same. There is only a slight difference in the drift ratio value at which the compressive failure is triggered in the wall boundary (0.63% for curvature integration and 0.57% for plastic hinge approach).

3.10.4 Buckling Analysis

First it is required to find the strain limit value of Equation (2.21). For this case b_{cr}=7.87 in. (200 mm), k=0.5, h_u= 100.39 in. (2.55 m), $\kappa = 0.8$, vertical reinforcement $\emptyset 22mm@15cm$, $f'_c = 7.3\ ksi$ $(50\ MPa)$ and $f_y = 73.4\ ksi$ $(506\ MPa)$. Therefore, $\in_{sm} = 0.039$. This limit is higher than the maximum tensile strain obtained for analysis $\in_{sm} = 0.008$ (Figure 3.38). But at this stage the wall boundary is crushed. Then, it is possible to use the buckling model to investigate the stability of the section with the cover spalled off. For this case, b_{cr}=4.0 in. (101 mm) and $\kappa = 1$. Therefore $\in_{sm} = 0.012$.

The maximum tensile strain $\in_s = 0.008$ and the limit value $\in_{sm} = 0.012$ are close, but boundary crushing or lateral buckling were not observed after the 2010 Chile earthquake. Therefore, the analysis suggests that the building did not reach a drift ratio greater than 0.57% during the earthquake.

3.11 WALL Q ANALYSIS

Figure 3.39 shows an elevation view of wall Q.

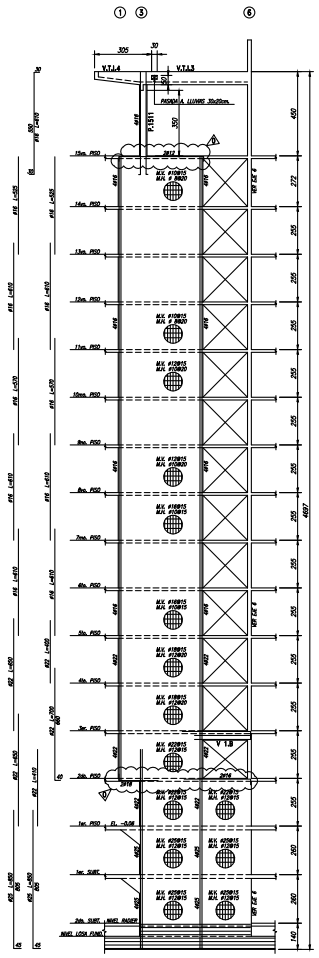

Figure 3.39 Elevation view of wall Q.

Wall Q starts in the second story. For the first story and below, walls Q and R are a single unit. Therefore, for modeling issues, nonlinearity must be concentrated in the second story (first "weak" level).

3.11.1 Loads

Figure 3.40 shows the tributary area for gravity loads (typical floor).

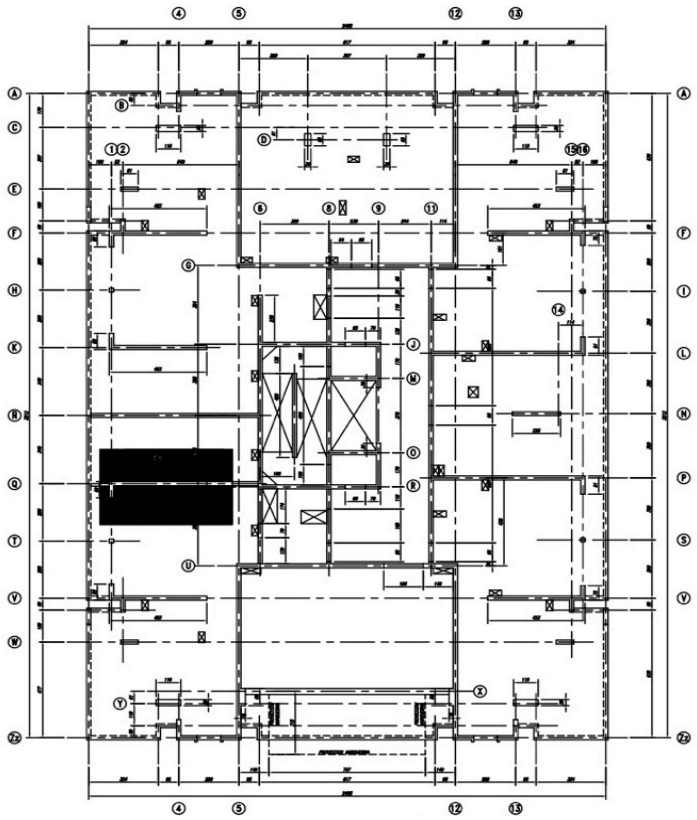

Figure 3.40 Tributary area at level 2-14 (typical floor).

Table 3.13 shows the gravity load per floor for wall Q.

Table 3.13 Gravity load per floor wall Q.

Floor	Area, ft^2 (m^2)	Dead Load, kips (kN)	Live Load, kips (kN)
-2	673.12 (62.53)	75.83 (337.31)	6.89 (30.65)
-1	673.12 (62.53)	75.83 (337.31)	6.89 (30.65)
1	498.58 (46.32)	43.40 (193.05)	5.11 (22.73)
2 to 14	248.11 (23.05)	21.60 (96.08)	2.54 (11.30)
Roof	201.15 (18.69)	17.51 (77.89)	2.06 (9.16)

The axial load at the bottom level of the second story is P=522 kips (2322 kN). Therefore $P/A_g f'_c$=5%.

3.11.2 Curvature Integration Approach

Figure 3.41 shows the XTRACT model section properties.

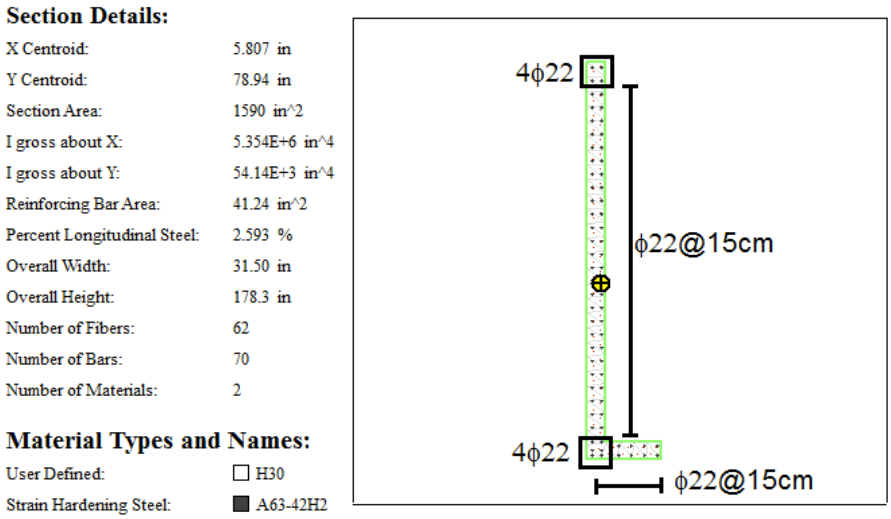

Figure 3.41 XTRACT model section properties for wall Q (1 in. = 25.4 mm, bars diameter in mm).

Figure 3.42 shows the moment-curvature relations.

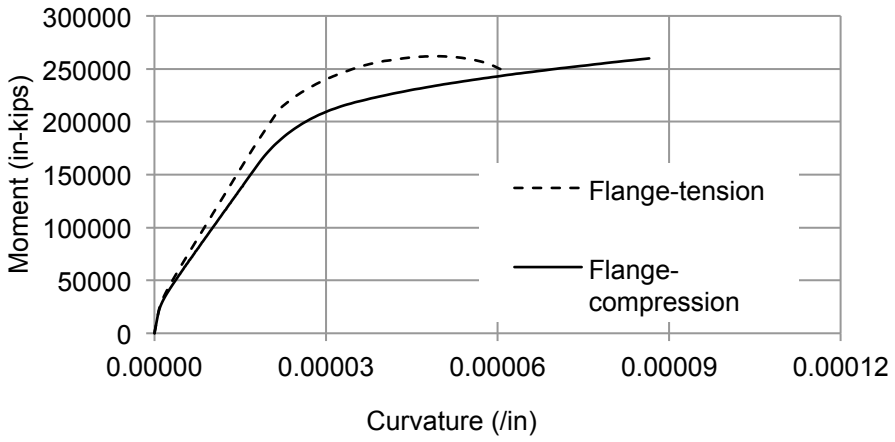

Figure 3.42 Moment-curvature relations axial load *N*=522 kips (1 in. = 25.4 mm; 1 in-kips = 0.11 kN-m).

As for wall Ñ, the reference lateral force distribution used in this model is inverted triangular and the amplitude of this distribution was increased until achieving the target displacement. Figure 3.43 shows the normalized moment and curvature over the height diagram for the case of flange in tension ($DR = 0.68\%$), when the stem experienced compressive failure.

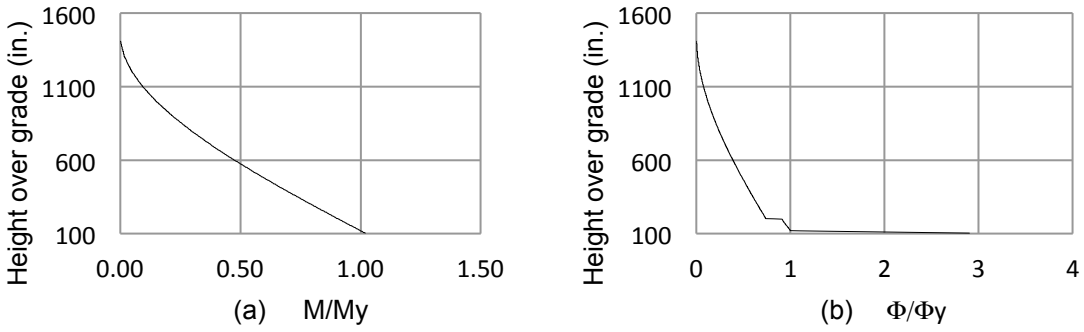

Figure 3.43 (a) Normalized moment; (b) curvature for flange in tension.

Figure 3.44 shows the normalized moment and curvature over the height diagram for the case of flange in compression ($DR = 0.68\%$).

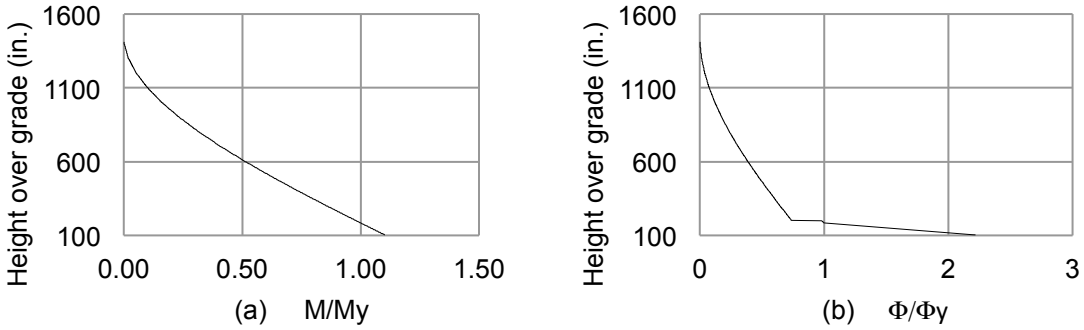

Figure 3.44 (a) Normalized moment; (b) curvature for flange in compression.

Figure 3.45 shows the calculated section strain profiles.

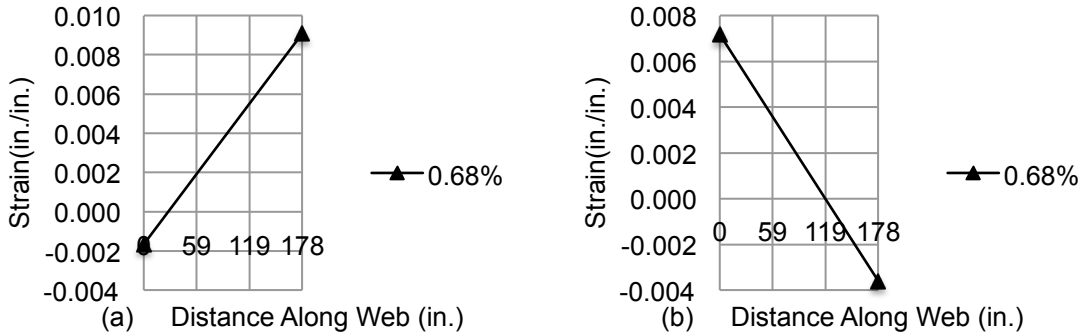

Figure 3.45 Strain profiles for wall Q from curvature integration: (a) flange in compression; (b) flange in tension.

From Figure 3.45, for the case of flange in tension, the ultimate state is triggered by compressive failure at the wall stem, when the maximum compressive strain reaches $\epsilon_c = 0.0036$ at an average drift of 0.68%. At this drift ratio, when the flange is in compression, the tensile strain in the stem is close to $\epsilon_{sm} = 0.009$.

3.11.3 Simplified Plastic Hinge Approach

A simplified plastic hinge approach according to Equation (2.20) is used as in wall Ñ. When the flange is in tension, the ultimate state is triggered by compressive failure at the wall stem, at a curvature $\emptyset_u = 6.18 \cdot 10^{-5}$ in.$^{-1}$. Therefore, the drift ratio is DR $= \emptyset_u \, l_p = 6.18 \cdot 10^{-5} \cdot 0.5 \cdot 178 = 0.6\%$. Figure 3.46 shows the calculated section strain profiles.

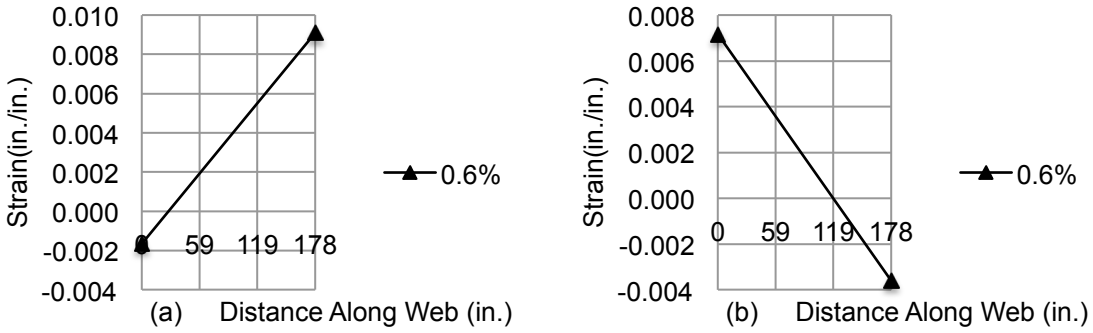

Figure 3.46 Strain profiles for wall Q from simplified plastic hinge approach: (a) flange in compression; (b) flange in tension.

The strain profiles obtained from both approaches (curvature integration and plastic hinge) are exactly the same. There is only a slight difference in the drift ratio value at which the compressive failure is triggered in the wall stem.

3.11.4 Buckling Analysis

In wall Q, the stem crushes at a drift ratio between 0.6% and 0.68% when the flange is in tension. At this stage, it is possible to evaluate Equation (2.21) for the spalled off condition. Then b_{cr}=4.0 in. (101 mm), k=0.5, h_u= 100.39 in. (2.55 m), $\kappa = 1$, vertical reinforcement $\emptyset 22mm@15cm$, $f'_c = 7.3\ ksi\ (50\ MPa)$ and $f_y = 73.4\ ksi\ (506\ MPa)$. Therefore $\in_{sm}$= 0.012.

Even though the maximum tensile strain and the limit value given by Equation (2.21) are close, lateral buckling was not observed after the 2010 Chile earthquake. Therefore, the analysis suggests that the building did not reach a drift ratio of 0.6% during the earthquake.

3.12 ANALYSIS SUMMARY

Three walls of Alto Huerto building were analyzed: Ñ, K and Q. All of them are oriented in the east-west direction. Walls Ñ and K were chosen because they are located at a close distance, 11.15 ft (3.40 m). Both could have failed in the first story and only wall Ñ buckled. Wall Q is a different case because its failure can be triggered in the second story (Figure 3.39).

The estimated elastic drift ratio for this building is 1.43%. This value was calculated from a linear elastic analysis using the software ETABS.

According to this study, none of the walls is able to reach $DR = 1.43\%$ without failure. Crushing is obtained in the stem of walls K and Q at $DR \sim 0.6\%$. Only minor post-earthquake

damage was observed in these walls in the plastic hinge zone. Probably, the building did not reach $DR = 0.6\%$. Wall Ñ stem crushes at $DR \sim 0.5\%$. After the wall crushes, the study showed that it is possible to trigger the wall lateral instability with the cover spalled off. This agrees with the observed post-earthquake damage.

4 Emerald Building

4.1 GEOMETRY

Emerald building is located in Av. Irarrazabal #2931 Ñuñoa, Santiago, Chile (latitude: -33.4546341, longitude: -70.6005649). The structure was severely damaged by the Chile earthquake on February 27th, 2010.

The building was designed in 2006 and constructed in 2009. It has twenty stories and four subterranean levels. Its total plan area is 220,660 ft^2 (20,500 m^2) approximately. The gravity and seismic force-resisting system are composed of reinforced concrete walls of 6.69 in. (170 mm) typical thickness. The typical story height is 8.27 ft (2.52 m).

Figure 4.1 shows the typical plan view.

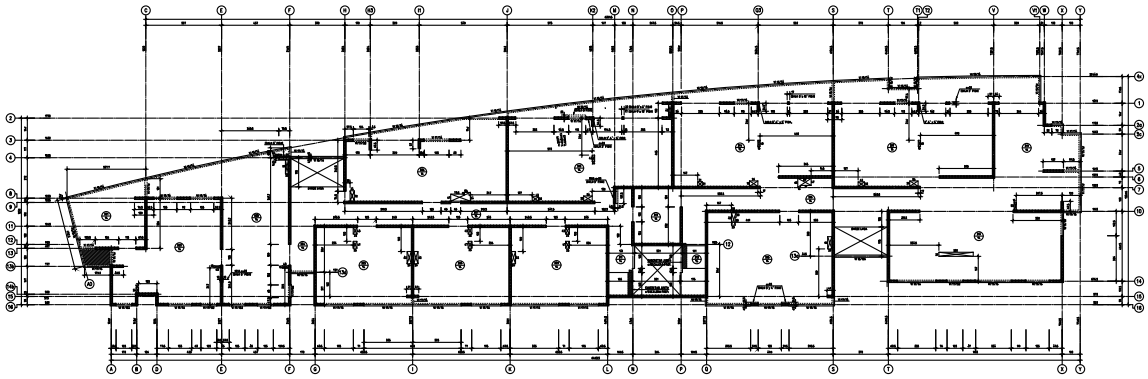

Figure 4.1 Emerald building (Santiago-Chile) – Typical plan view.

The damage is mainly concentrated in the first subterranean level.

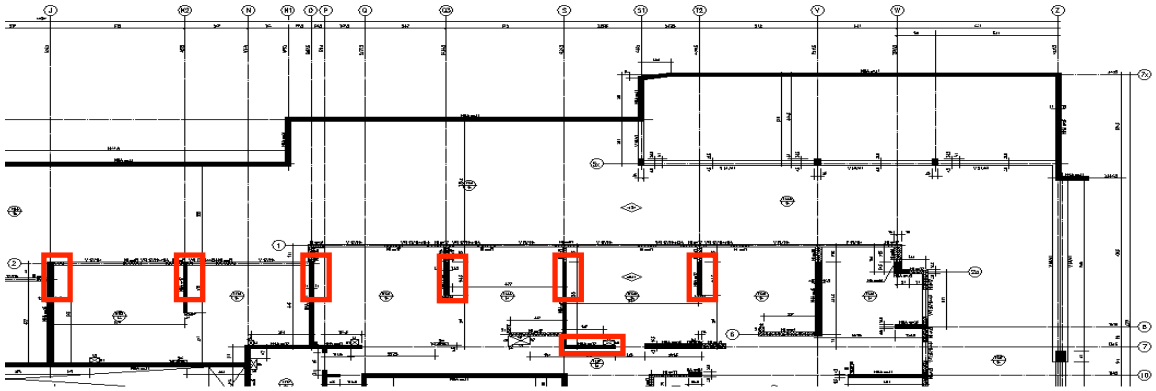

Figure 4.2 Emerald building (Santiago-Chile) – Damaged walls in the first subterranean level.

4.2 ANALYSIS AND DESIGN STANDARDS

Gravity and seismic loads were calculated following the Chilean standards NCh 1537 Of. 1986 and NCh 433 Of. 1996. Reinforced concrete members were designed according to ACI 318 (2005).

4.3 DESIGN SPECTRUM

The parameters used in the building seismic design according to NCh 433. Of. 1996 are:

- Building category C
- Seismic zone 2
- Soil type II
- Damping ratio 5%

NCh 433. Of. 1996 response spectrum analysis was performed, according to Equations (4.1) to (4.3).

$$S_\alpha = \frac{IA_0\alpha}{R^*} \tag{4.1}$$

$$\alpha = \frac{1 + 4.5\left(\frac{T_n}{T_0}\right)^p}{1 + \left(\frac{T_n}{T_0}\right)^3} \tag{4.2}$$

$$R^* = 1 + \frac{T^*}{0.1T_0 + \frac{T^*}{R_0}} \tag{4.3}$$

Where:

- S_α Pseudo acceleration
- I Importance factor = 1 for building category C
- A_0 Peak ground acceleration = 0.3 g for seismic zone 2
- g Acceleration of gravity, 386 in./s^2 (9.81 m/s^2)
- T_n Mode nth vibration period (s)
- T_0 Soil dependent parameter = 0.30 (s) for soil type II
- p Soil dependent parameter = 1.5 for soil type II
- T^* Vibration period of the mode with greatest equivalent mass in the analysis direction (s)
- R_0 Response modification factor = 11

Figure 4.3 shows the elastic response spectrum.

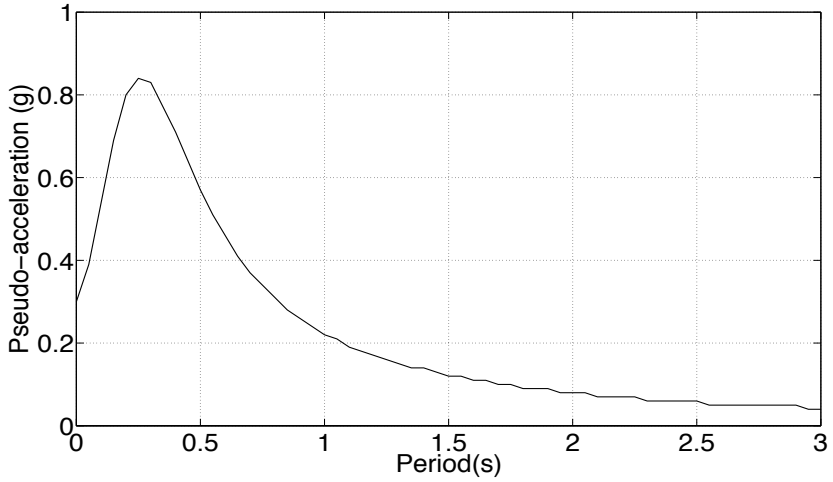

Figure 4.3 NCh 433 Of. 1996 elastic response spectrum (*R=1).**

4.4 RECORDED GROUND MOTION

Instruments recorded the ground acceleration during the February 27th 2010 Chile earthquake in several locations in Santiago. Three stations close to the building site are located in Santiago-Centro, La Florida and Peñalolen.

The highest displacement demands are obtained for the Santiago-Centro record. This is the closest station to the building site, and the soil type is similar in Santiago-Centro and Ñuñoa, where the building is located. In both cases the soil classifies as type II according to NCh 433 Of. 1996. Therefore, the Santiago-Centro record is selected for analysis.

Figure 4.4 to Figure 4.6 show the acceleration records for the three measured directions.

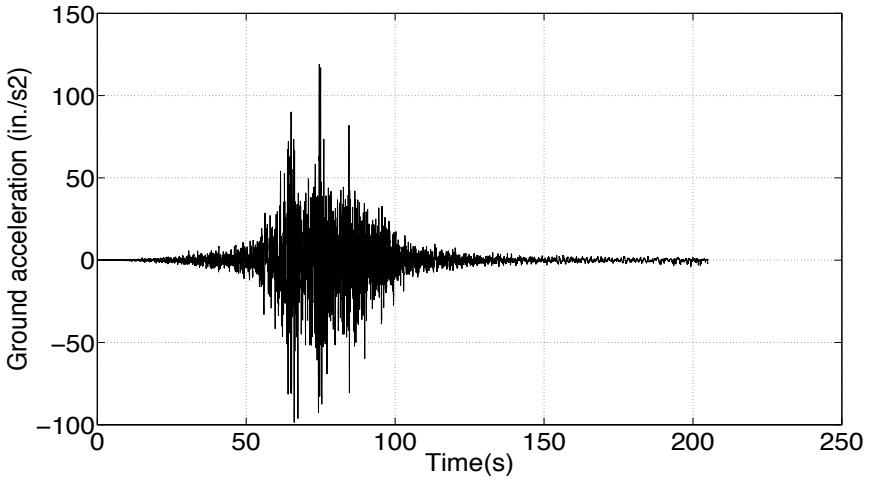

Figure 4.4 Corrected ground motion Santiago Centro – EW direction (1 in.=25.4 mm).

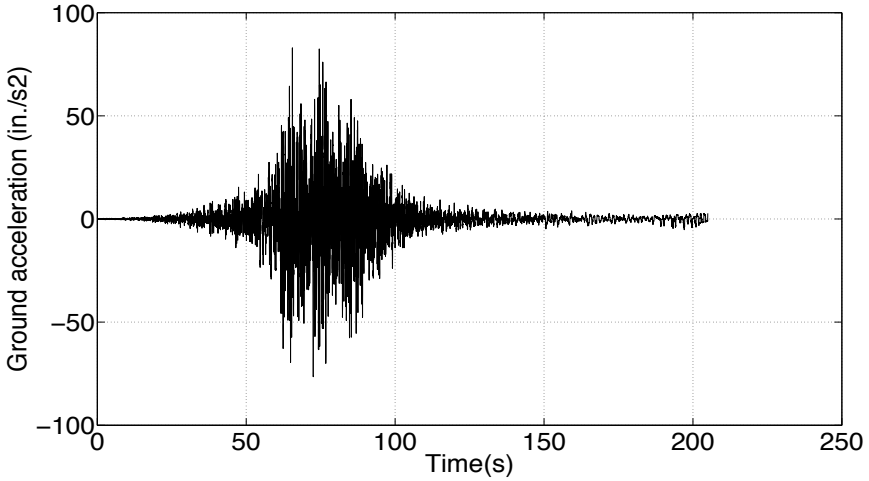

Figure 4.5 Corrected ground motion Santiago Centro – NS direction (1 in.=25.4 mm).

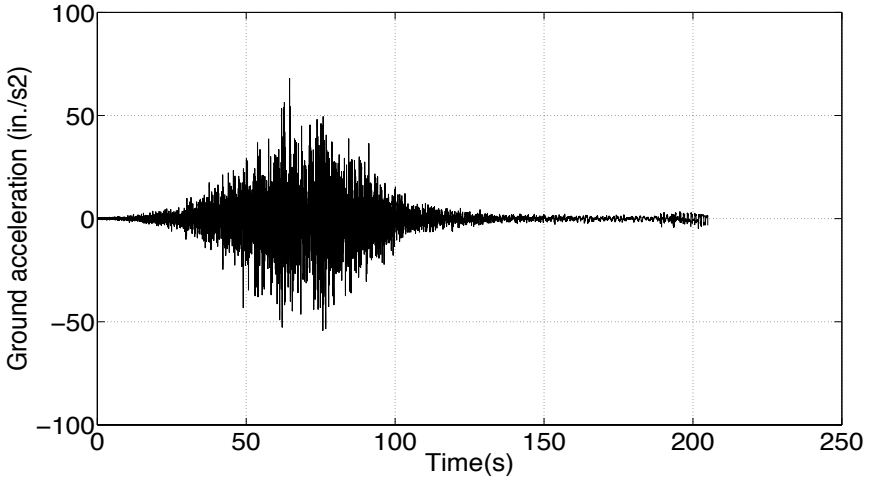

Figure 4.6 Corrected ground motion Santiago Centro – UD direction (1 in.=25.4 mm).

Figure 4.7 to Figure 4.9 show the pseudo acceleration, pseudo velocity, and the displacement response spectrum (2% damping ratio).

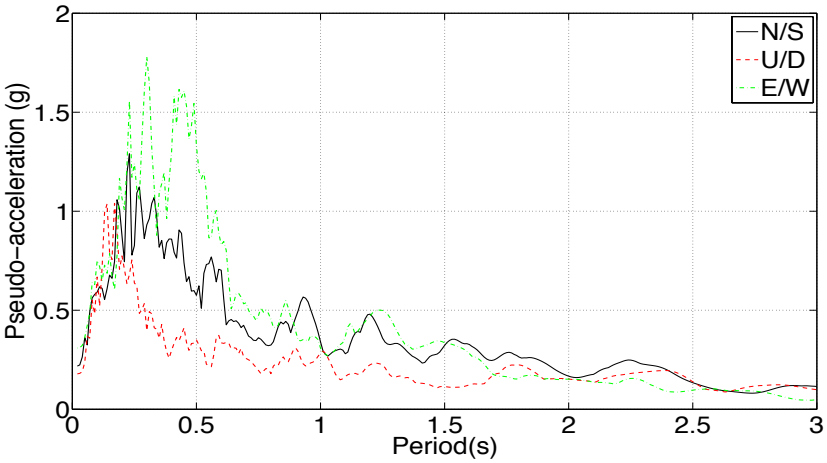

Figure 4.7 Pseudo acceleration spectrum Santiago Centro.

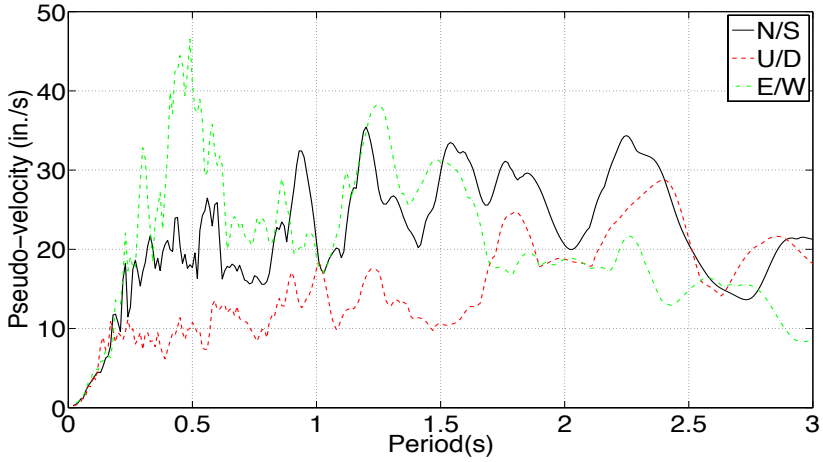

Figure 4.8 Pseudo velocity spectrum Santiago Centro (1 in.=25.4 mm).

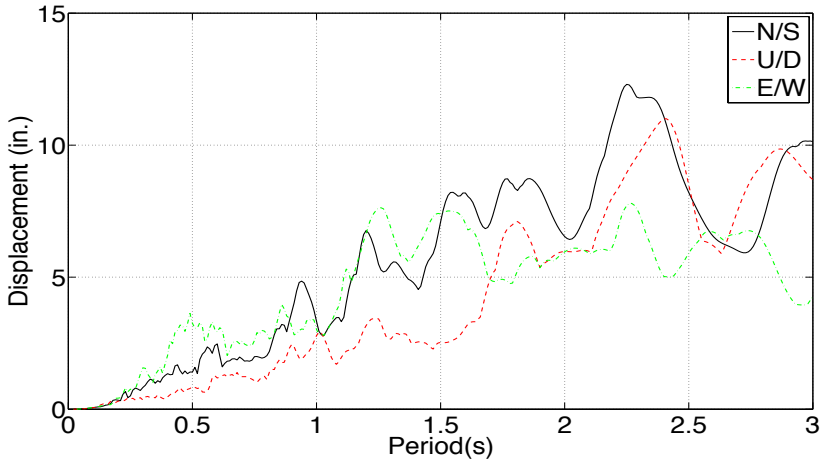

Figure 4.9 Displacement spectrum Santiago Centro (1 in.=25.4 mm).

From a linear analysis model developed in ETABS (section 4.7), the first-mode period in the EW direction is $T = 1.56\ s$. This period is based in several assumptions regarding material properties and loads. According to Figure 4.9, in the EW direction the peak spectral displacement is close to 7.5 in. (190 mm) for the reasonable building period range. Therefore, the maximum average drift ratio is:

$$DR_{max} = 1.5\frac{D}{\Delta h} = 1.5\frac{7.5}{1885} = 0.60\% \tag{4.4}$$

Figure 4.10 shows a comparison between the computed PSA spectrum (2% damping ratio) and the NCh 433 Of. 1996 elastic spectrum (R^*=1).

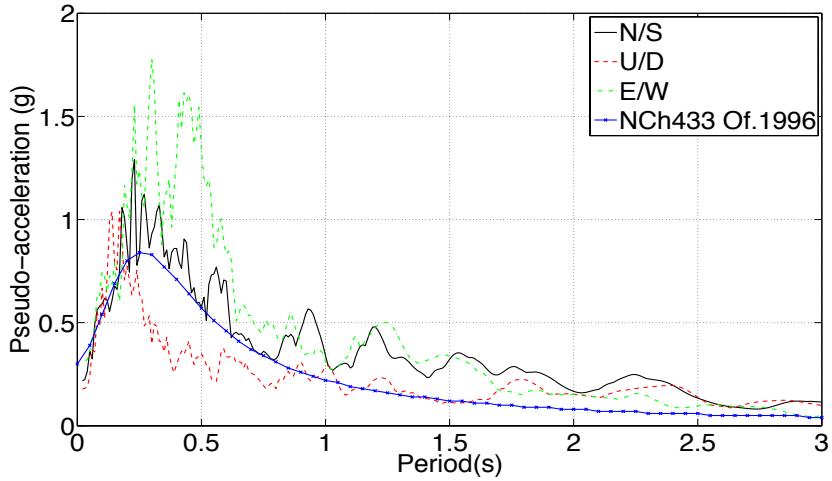

Figure 4.10 Pseudo acceleration spectrum comparison.

Figure 4.11 shows a tripartite plot for E-W, N-S and U-D motion.

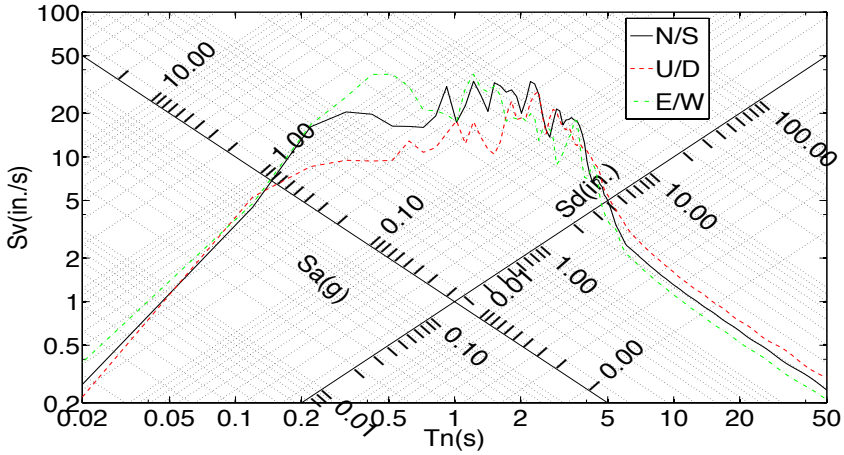

Figure 4.11 Tripartite plot for E-W, N-S and U-D motion (1 in.=25.4 mm).

From Figure 4.11 it is clear that for the 1.56s first mode period (EW direction) the structure is in the displacement preserved zone ($R = \mu\ and\ \gamma = 1$), therefore:

$$DR_{max}^{non\ linear} = DR_{max}^{elastic} \tag{4.5}$$

4.5 MATERIAL PROPERTIES

According to the building design documents, material nominal properties are:

- Concrete H25 NC 90%: maximum compressive strength in cubic test specimen 3,600 psi (25 MPa)
- Reinforcement steel A63-42H: tensile strength f_u= 91 ksi (630 MPa), yield strength f_y= 60 ksi (420 MPa)

From Table 3.1, f'_c= 2,900 psi (20 MPa).

For analyses, real material properties (DICTUC report, 2012) are used instead of nominal properties. Concrete compressive strength is determined from cores testing. Values are shown next:

- Wall O, first subterranean level: f'_c= 3,800 psi (25.9 MPa).
- Wall K2, first subterranean level: f'_c= 4,100 psi (28.5 MPa).

For linear analysis, the effective flexural and axial rigidity (including cracking) is used, according to ASCE 41 (2006), section 6.3.1.2.

Kent and Park (1971) unconfined concrete model is used for nonlinear analysis. Measured reinforcement properties from coupons from the building are tensile strength f_u= 110 ksi (759 MPa) and yield strength f_y= 73.3 ksi (506 MPa).

4.6 MAIN DAMAGE DESCRIPTION

The main post-earthquake damage of the building (DICTUC report # 878055, 2010) is described in this section. Figure 4.12 shows exterior views of the building.

(a) (b)

Figure 4.12 Exterior views from Av. Irarrázabal: (a) west face; (b) north face.

The main damage is concentrated in the first subterranean level, in six walls in the east/west direction, as pictured in Figure 4.13.

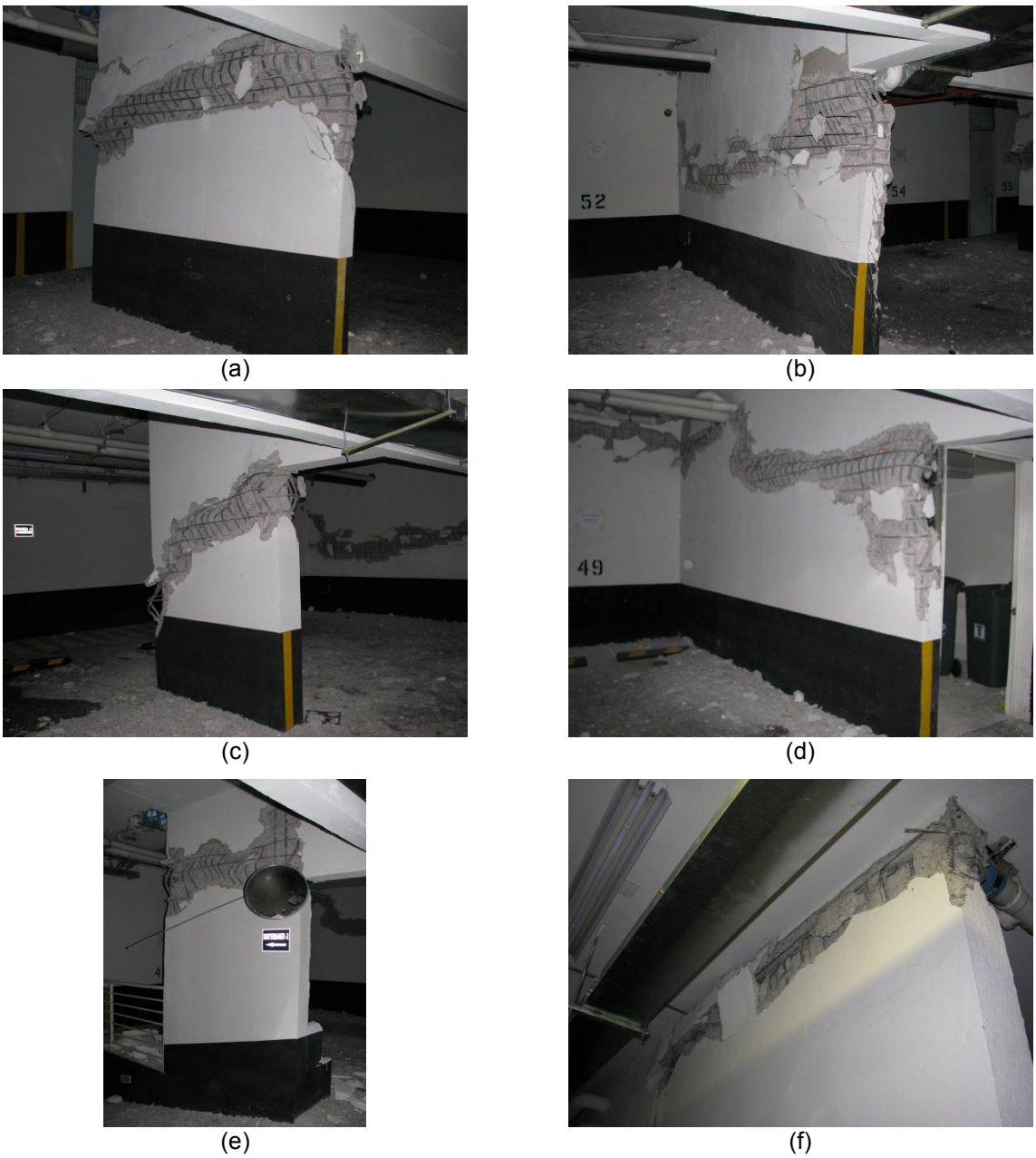

(a) (b) (c) (d) (e) (f)

Figure 4.13 Damaged walls in first subterranean level: (a) axis K2; (b) axis O; (c) axis Q3; (d) axis S; (e) axis T2; (f) axis 7.

Second to fourth subterranean levels do not show damage. In the first story only minor damage is observed. In the second story, there is one damaged wall, as shown in Figure 4.14.

(a) (b)

Figure 4.14 Damaged walls in second story, axis J: (a) view 1; (b) view 2.

4.7 BUILDING LINEAR MODEL

Figure 4.15 shows the linear ETABS model.

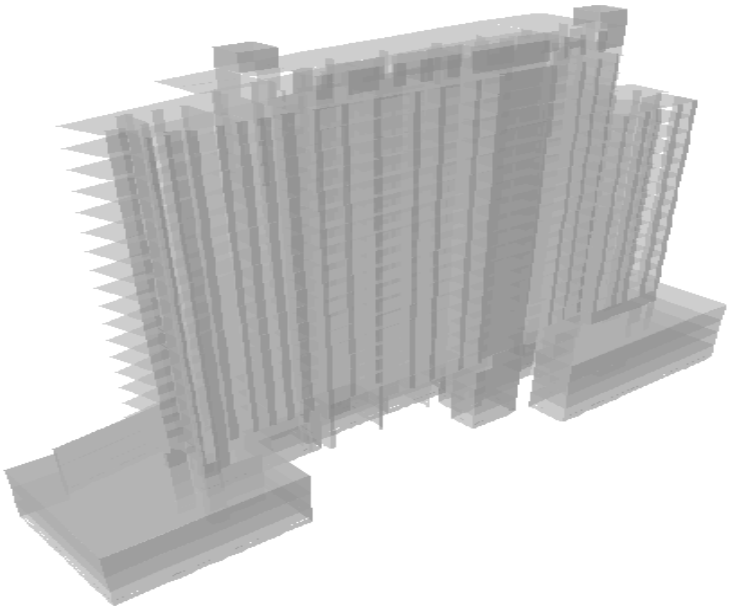

Figure 4.15 ETABS model for Emerald building.

4.7.1 Loads

Table 4.1 shows the calculated gravity loads. For the purpose of defining seismic mass 50% of live load is considered.

Table 4.1 Gravity loads per floor.

Floor	Slab thickness, in. (mm)	Dead Load, psf (kPa)	Live Load, psf (kPa)
-4 to -1	7.09 (180)	102.00 (4.88)	10.03 (0.48)
1 to 20	5.51 (140)	82.00 (3.93)	10.03 (0.48)

4.7.2 Seismic Analysis

Table 4.2 shows the building modes periods and modal participating mass ratios.

Table 4.2 Modal analysis output for Emerald building.

Mode	Period (s)	Modal mass ratio X direction	Modal mass ratio Y direction
1	1.56	0.01	52.76
2	1.25	1.06	1.70
3	0.75	51.94	0.10
4	0.31	0.04	19.08
5	0.28	0.25	0.02
6	0.21	12.27	0.09
7	0.16	0.33	8.76
8	0.13	0.12	3.24
9	0.11	10.58	0.04
10	0.09	0.45	5.85
11	0.06	18.22	0.74
12	0.05	0.17	5.93

Therefore, the 3rd mode has the greatest effective modal mass in long building direction ($T = 0.75\ s$), and the 1st mode has the greatest effective modal mass in short building direction ($T = 1.56\ s$). Figure 4.16 shows the maximum floor displacements for the east-west direction ($T = 1.56\ s$).

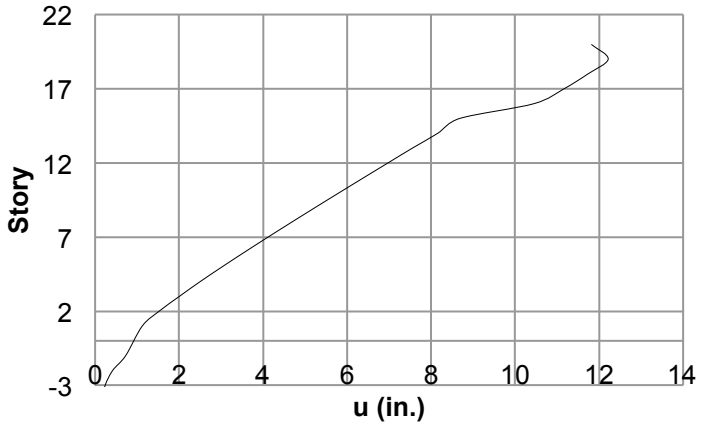

Figure 4.16 Maximum floor displacements, east-west direction (1 in. = 25.4 mm).

Therefore, the average drift is 12/1885=0.64%, close to the simplified value obtained in Equation (4.4).

4.8 WALL O ANALYSIS

4.8.1 Simplified Plastic Hinge Approach

For this case, only the simplified plastic hinge model is used, according to Equation (2.20). Figure 4.17 shows an elevation view of wall O.

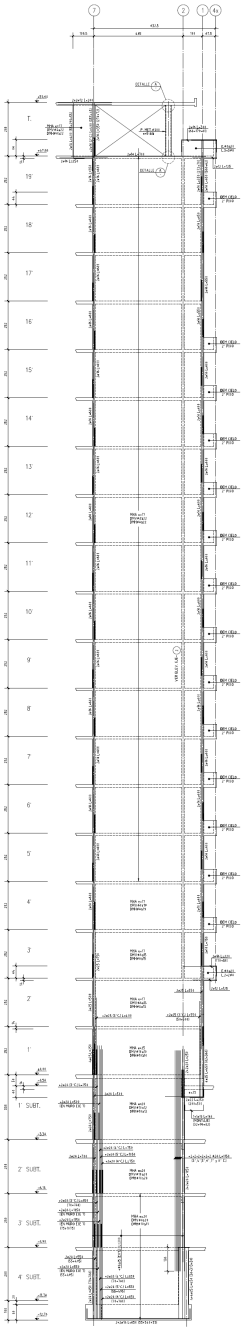

Figure 4.17 Elevation view of wall O.

In this case the plastic hinge is located at the first subterranean level. Figure 4.18 shows the section properties for XTRACT model.

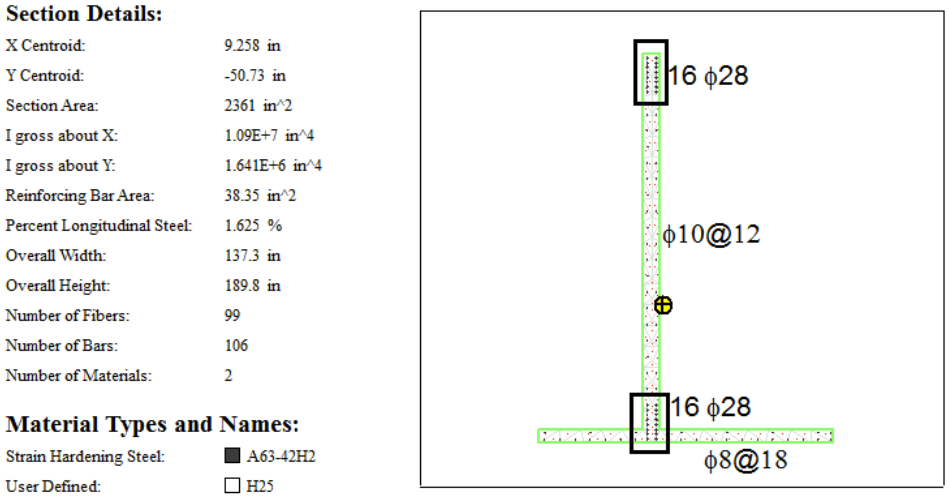

Figure 4.18 XTRACT model section properties for wall O (1 in. = 25.4 mm, bars diameter in mm).

Figure 4.19 shows the moment-curvature relations.

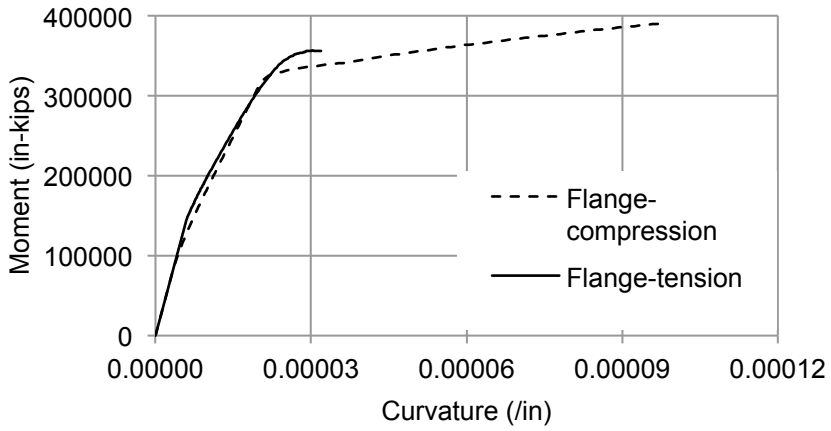

Figure 4.19 Moment-curvature relations axial load *N*= 2048 kips (1 in. = 25.4 mm; 1 in-kips = 0.11 kN-m).

Considering the elastic drift ratio $DR = 0.6\%$ and the plastic hinge in the first subterranean level, $\emptyset_u = \frac{0.6\%}{0.5 \cdot 189.8} = 6.32 \cdot 10^{-5}$ in.$^{-1}$. This simplified model considers the wall as a cantilever column with base at the bottom of the first subterranean level. Therefore, a small lateral displacement is allowed at the grade level.

Figure 4.20 shows the calculated strain profiles.

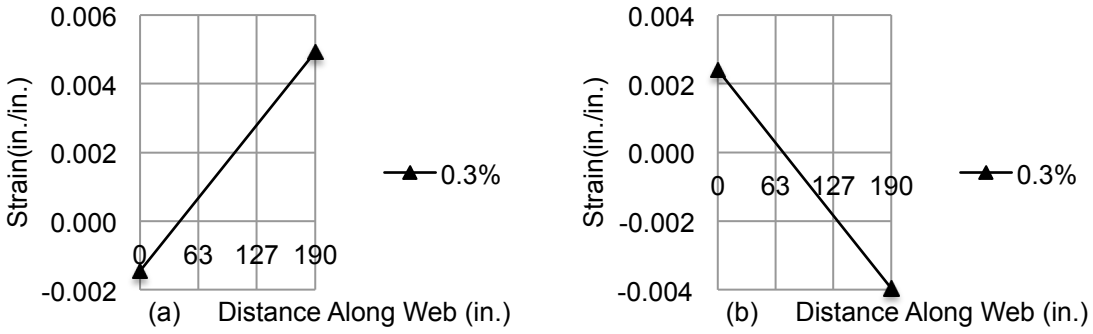

Figure 4.20 Strain profiles for wall O from simplified plastic hinge approach: (a) flange in compression; (b) flange in tension.

As shown in Figure 4.20, for the case of flange in tension, the ultimate state is triggered by compressive failure at the wall stem, when the maximum compressive strain reaches $\epsilon_c = 0.004$ at $DR = 0.3\%$. Then the wall does not reach $DR = 0.6\%$ without crushing failure. At $DR = 0.3\%$, when the flange is in compression, the maximum tensile strain in the boundary bars is $\in_{sm} = 0.005$.

4.8.2 Buckling Analysis

The wall web crushes at $DR = 0.3\%$. At this stage, it is possible to use the buckling model to investigate the stability of the section with the cover spalled off.

For this case, b_{cr}=4.0 in. (101 mm), k=0.5, h_u= 133 in. (3.38 m), and $\kappa = 1$. The reinforcement ratio for the 16ϕ28mm boundary bars is $\rho = 16\pi\frac{2.8^2}{4}/(40 \cdot 10) = 24.63\%$. Therefore, from Equation (2.21), $\in_{sm} = 0.006$.

In this case, the tensile strain limit ($\in_{sm} = 0.006$) is slightly higher than the calculated strain from the simplified plastic hinge approach ($\in_{sm} = 0.005$). Therefore, the lateral instability presented in section 2.2 for the section with the cover spalled off cannot be ruled out as an explanation of the observed post-earthquake damage.

4.9 WALL K2 ANALYSIS

4.9.1 Simplified Plastic Hinge Approach

The same approach used in wall O is applied here. Figure 4.21 shows an elevation view of wall K2.

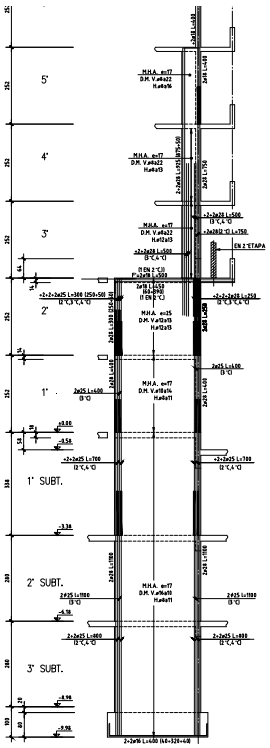

Figure 4.21 Elevation view of wall K2.

In this case the plastic hinge is located at the first subterranean level (as in wall O).

Figure 4.22 shows the section properties for XTRACT model.

Section Details:

X Centroid:	-.4460E-16 in
Y Centroid:	86.27E-3 in
Section Area:	747.3 in^2
I gross about X:	818.8E+3 in^4
I gross about Y:	2386 in^4
Reinforcing Bar Area:	27.29 in^2
Percent Longitudinal Steel:	3.651 %
Overall Width:	6.693 in
Overall Height:	111.7 in
Number of Fibers:	120
Number of Bars:	62
Number of Materials:	2

Material Types and Names:

Strain Hardening Steel:	A63-42H2
User Defined:	H25

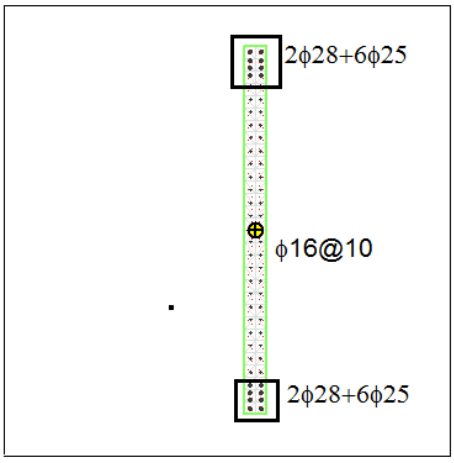

Figure 4.22 XTRACT model section properties for wall K2 (1 in. = 25.4 mm, bars diameter in mm).

Figure 4.23 shows the XTRACT moment-curvature relation.

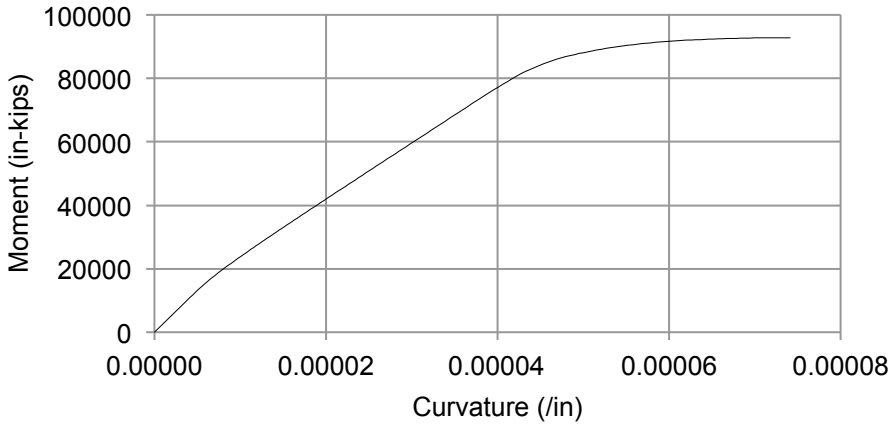

Figure 4.23 Moment-curvature relation axial load *N*= 562 kips (1 in. = 25.4 mm; 1 in-kips = 0.11 kN-m).

Considering $DR = 0.6\%$ and the plastic hinge in the first subterranean level, $\emptyset_u = \frac{0.6\%}{0.5 \cdot 111.7} = 1.07 \cdot 10^{-4}$ in.$^{-1}$. As in wall O, the simplified model considers the wall as a cantilever column with base at the bottom of the first subterranean level.

The ultimate state is triggered by compressive failure at the wall boundary, at a curvature $\emptyset_u = 8.19 \cdot 10^{-5}$ in.$^{-1}$. Therefore, the drift ratio is $\text{DR} = \emptyset_u \, l_p = 8.19 \cdot 10^{-5} \cdot 0.5 \cdot 112 = 0.5\%$. Figure 4.24 shows the calculated section strain profiles.

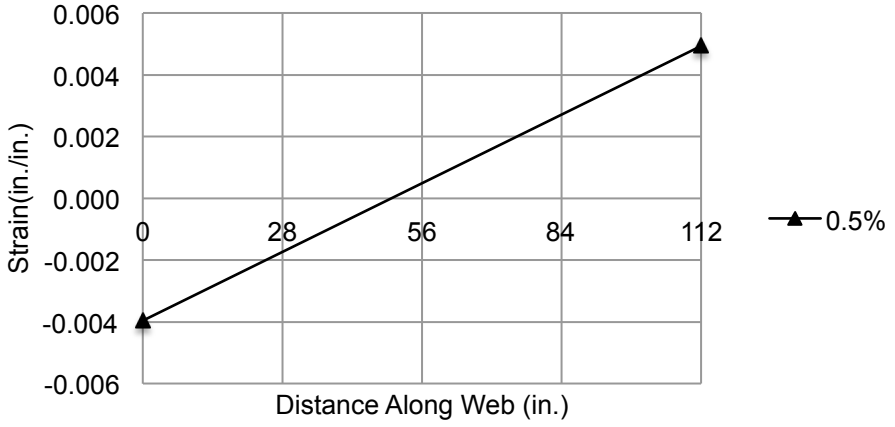

Figure 4.24 Strain profile for wall K2 from simplified plastic hinge approach.

From Figure 4.24, the maximum tensile strain when the wall boundary crushes is $\epsilon_{sm} = 0.005$.

4.9.2 Buckling Analysis

After the wall crushes, it is possible to use the buckling model to investigate the stability of the section with the cover spalled off. For this case, b_{cr}=3.2 in. (80 mm), k=0.5, h_u= 133 in. (3.38 m), and $\kappa = 1$. The reinforcement ratio for 2ϕ28mm+6ϕ25mm bars is $\rho = \left(2\pi\frac{2.8^2}{4} + 6\pi\frac{2.5^2}{4}\right)/(20 \cdot 8) = 26.10\%$. Therefore $\in_{sm} = 0.0053$.

As in wall O, the tensile strain limit ($\in_{sm} = 0.0053$) is slightly higher than the calculated strain from the simplified plastic hinge approach ($\in_{sm} = 0.005$). As in wall O, the presented buckling theory, considering only the confined core width, could explain the observe failure mode.

4.10 ANALYSIS SUMMARY

Two walls of Emerald building were analyzed: O and K2. Both are oriented in the east-west direction, which is the building short direction, with a main period of 1.56s. Both walls buckled in the first subterranean level, as shown in section 4.6.

The estimated building average drift ratio is $DR \sim 0.6\%$. This value was calculated from a linear elastic analysis using the software ETABS. None of the walls is able to reach $DR \sim 0.6\%$ without failure.

The analysis results suggest that lateral instability after the cover spalled off cannot be ruled out in both walls, which can explain the observed post-earthquake damage.

5 Summary

- Wall boundaries can sustain overall buckling when subjected to earthquake loading. Tendency to buckle depends primarily on the aspect ratio h_u/b.
- Two failure modes are hypothesized. One hypothesis is that tensile yielding for loading in one direction weakens the boundary for subsequent loading in the opposite direction. A theory for this first hypothesis is presented. The second hypothesis is that the wall crushes first, leaving an even smaller, eccentric section cross section. This "plastic" section essentially flows laterally, leading to a secondary buckling failure. Either type of buckling can lead to critical loss of axial force capacity in the flexural compression zone of the wall.
- Five laboratory test specimens are analyzed. TW2 (Thomsen and Wallace, 2004) and R2 (Oesterle et al., 1976) specimens showed lateral instability in the compression zone. The analyses suggest that in both cases the failure appears to be caused by concrete crushing first, followed by lateral buckling of the reduced section, according to the second hypothesis.
- Several walls of two Chilean buildings (Alto Huerto and Emerald) are also analyzed. Both buildings were severely damaged after the 2010 earthquake.
- In Alto Huerto building, walls Ñ, K and Q are analyzed. Wall Ñ has a tee-shaped cross section, with buckling apparent in the stem. From the analysis results, although it is not possible to rule out buckling as the trigger for wall failure, it seems much more likely to have crushing first, with buckling of the crushed section following. Adjacent Wall K had rectangular cross section, with minor spalling of cover concrete. Analyses suggest that the drift demand was not high enough to trigger the wall failure.
- In Emerald building, buckled walls O and K2 are analyzed. Similar conclusions are obtained. Failure modes appear to be caused by concrete crushing first, followed by lateral buckling of the reduced section.

6 Recommendations

- Building codes should have a slenderness ratio limit for the intended hinge zone of special structural walls. The UBC (1997) limit of $h_u/b \leq 16$ is recommended for walls that maintain their concrete cover. The same limit could be applied to walls for which cover concrete has spalled. However, the limited evidence suggests that the h_u/b limit should apply with b referring to the width of the confined core, which in ACI 318 is defined as b_c.
- Based on consideration of out-of-plane buckling, special structural walls should have two curtains of reinforcement within the intended hinge zone, regardless the shear or the wall thickness.

REFERENCES

Acevedo CE, Creagh A, Moehle JP, Hassan W, Tanyeri AC (2010). Seismic Vulnerability of Non-special Boundary Element of Shear Wall under Axial Force Reversals, *Network for Earthquake Engineering Simulation*, 16 pp.

American Society of Civil Engineers (2006). Seismic rehabilitation of existing buildings ASCE 41-06.

American Concrete Institute (2011). Building code requirements for structural concrete and commentary ACI 318-11.

Chai YH, and Elayer DT (1999). Lateral Stability of Reinforced Concrete Columns under Axial Reversed Cyclic Tension and Compression. *ACI Structural Journal*, American Concrete Institute, V. 96, No. 5, pp. 780-789.

Creagh A, Acevedo C, Moehle JP, Hassan W, Tanyeri AC (2010). Seismic Performance of Concrete Special Boundary Element, *Network for Earthquake Engineering Simulation*, 18 pp.

DICTUC (2010). Inspección visual y levantamiento de daño Edificio Alto Huerto Concepción, *Report # 906575/10-056-EE-01-R0*, Santiago, Chile.

DICTUC (2010). Verificación de correcta ejecución de las obras conforme de diseño Edificio Alto Huerto San Pedro de la Paz, *Report # 906575/10-056-EN-01-R0*, Santiago, Chile.

DICTUC (2010). Contrastación de la existencia en terreno de elementos de confinamiento de borde y del plano de algunos muros versus especificaciones de planos estructurales tras sismo del 27 de febrero de 2010. *Report # 878055*, Santiago, Chile.

DICTUC (2012). Resistencia del hormigón y de las barras de refuerzo edificio Emerald, Santiago, Chile.

EMPRO (2007). Informe de mecánica de suelos Edificio Alto Huerto, *Report # 71071-07*, Concepción, Chile.

INN (1986). Cargas permanentes y sobrecargas de uso, *Chilean standard # NCh 1537 Of. 1986*, Santiago, Chile.

INN (1996). Diseño sísmico de edificios, *Chilean standard # NCh 433 Of. 1996*, Santiago, Chile.

INN (2001). Hormigón – Testigos de hormigón endurecido – Parte 1: Extracción y ensayo, *Chilean standard # NCh 1171/1 Of.2001*, Santiago, Chile.

INN (2001). Hormigón – Testigos de hormigón endurecido – Parte 2: Evaluación de resultados de Resistencia mecánica, *Chilean standard # NCh 1171/2 Of.2001*, Santiago, Chile.

INN (2008). Hormigón armado. Requisitos de diseño y cálculo, *Chilean standard # NCh 430 Of. 2008*, Santiago, Chile.

Kent DC, and Park R (1971). Flexural members with confined concrete, *J. Struct. Div. ST7*, 97: 1969-1990.

Moehle JP (2011), *Reading material for CEE 244: Reinforced Concrete Structures*, University of California Berkeley, CA.

Moehle JP, Ghodsi T, Hooper JD, Fields DC, and Gedhada R (2011). Seismic Design of Cast-in-Place Concrete Special Structural Walls and Coupling Beams. *NEHRP Seismic Design Technical Brief No. 6*, NIST, 37 pp.

Oesterle RG, Fiorato AE, Johala LS, Carpenter JE, Russell HG, and Corley WG (1976), *Earthquake Resistant of Structural Walls – Test of Isolated Walls*, Research and Development - Constructions Technology Laboratories, Portland Cement Association, Skokie, Illinois.

Paulay T, and Priestley MJN (1993). Stability of Ductile Structural Walls. *ACI Structural Journal*, V. 90, No. 4, pp. 385-392.

Saatcioglu M, and Razvi SR (1992). Strength and ductility of confined concrete. *J. Struct. Eng.*, 118(6), 1590–1607.

Sepúlveda C (2007). Alto Huerto building project drawings, *Drawings # 28769-01 to 28769-44*, Concepción, Chile.

Taylor CP, Cote PA, and Wallace JW (1998). Design of slender reinforced concrete walls with openings. *Struct. J.*, 95(4), 420–433.

Thomsen JH, and Wallace JW (2004). Displacement-Based Design of Slender Reinforced Concrete Structural Walls-Experimental Verification, *J. Struct. Eng.*, 130(4), 618-630.

VMB (2006). Emerald building project drawings, *Drawings # 3641-A00 to 3641-A53*, Santiago, Chile.